

AD-769 893

CALCULATIONS OF NEAR FIELD, EARTHQUAKE
GROUND MOTION

J. Theodore Cherry

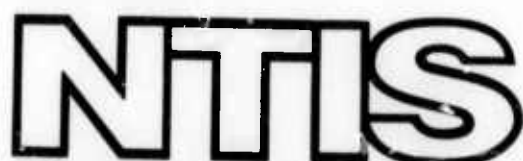
Systems, Science and Software

Prepared for:

Air Force Office of Scientific Research

29 June 1973

DISTRIBUTED BY:



National Technical Information Service
U. S. DEPARTMENT OF COMMERCE
5285 Port Royal Road, Springfield Va. 22151

UNCLASSIFIED

AD-769 893

Security Classification

DOCUMENT CONTROL DATA - R & D

(Security classification of title, body of abstract and indexing annotation must be entered when the overall report is classified)

1. ORIGINATING ACTIVITY (Corporate author)
 Systems, Science and Software
 PO Box 1620
 La Jolla, CA 92037

2a. REPORT SECURITY CLASSIFICATION
 UNCLASSIFIED

2b. GROUP

3. REPORT TITLE
 Calculations of Near Field, Earthquake Ground Motion

4. DESCRIPTIVE NOTES (Type of report and inclusive dates)
 Scientific....Interim, Annual Technical Report 1 May 1972 - 31 May 1973

5. AUTHOR(S) (First name, middle initial, last name)
 J. T Cherry

6. REPORT DATE
 29 June 1973

7a. TOTAL NO. OF PAGES
 847b. NO. OF REFS
 20

8a. CONTRACT OR GRANT NO
 F44620-72-C-0051

9a. ORIGINATOR'S REPORT NUMBER(S)

b. PROJECT NO.
 AO 2134

c.
 62701E

d.
 AFOSR-TR-73-1127

10. DISTRIBUTION STATEMENT

Approved for public release; distribution unlimited

11. SUPPLEMENTARY NOTES
 TECH, OTHER

12. SPONSORING MILITARY ACTIVITY
 Air Force Office of Scientific Research/AFOSR
 1400 Wilson Boulevard
 Arlington, VA 22209

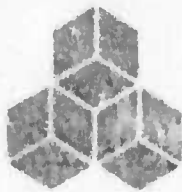
13. ABSTRACT

A stick-slip rupture model has been incorporated into a two-dimensional (plane strain) Lagrangian code with the added feature that rupture initiation is plastic work dependent. Realistic laboratory test data have been used as input to the model. Theoretical seismograms have been generated in both the frequency and time domain along with a decomposition of the ground motion into P and S components. The calculations suggest how estimates of fault length, rupture velocity and dynamic stress drop may be obtained from near field data. These estimates provide an initial specification of the parameters required by the rupture model in order to match a given set of near field data.

Reproduced by
 NATIONAL TECHNICAL
 INFORMATION SERVICE
 U.S. Department of Commerce
 Springfield VA 22151

91

DSR - TR - 78 - 1127



SYSTEMS, SCIENCE AND SOFTWARE

AD 769893

SSS-R-75-1759

CALCULATIONS OF NEAR FIELD, EARTHQUAKE GROUND MOTION

Annual Technical Report
For Period Ending 31 May 1973

Project Manager: J. Theodore Cherry (714) 453-0060

Sponsored by
Advanced Research Projects Agency
ARPA Order No. 2134

Monitored by
Air Force Office of Scientific Research
Arlington, Virginia 22209

D D C

NOV 14 1973

REF ID: A651150
B

Contract No. F44620-72-C-0051
Program Code 2F10
Effective Date of Contract: 1 June 1972
Contract Expiration Date: 28 Feb. 1974
Amount of Contract: \$112,709

S³ Project 195

DISTRIBUTION STATEMENT A

Approved for public release
Distribution Unlimited

June 29, 1973

Approved for public release
Distribution Unlimited



SYSTEMS, SCIENCE AND SOFTWARE

SSS-R-73-1759

CALCULATIONS OF NEAR FIELD, EARTHQUAKE GROUND MOTION

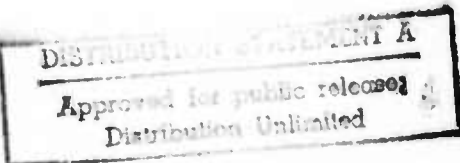
Annual Technical Report
For Period Ending 31 May 1973

Project Manager: J. Theodore Cherry (714) 453-0060

Sponsored by
Advanced Research Projects Agency
ARPA Order No. 2134

Monitored by
Air Force Office of Scientific Research
Arlington, Virginia 22209

Contract No. F44620-72-C-0051
Program Code 2F10
Effective Date of Contract: 1 June 1972
Contract Expiration Date: 28 Feb. 1974
Amount of Contract: \$112,709



S³ Project 195

June 29, 1973

P.O. BOX 1620, LA JOLLA, CALIFORNIA 92037. TELEPHONE (714) 453-0060

FOREWORD

This annual technical report entitled "Calculations of Near Field, Earthquake Ground Motion," is submitted by Systems, Science and Software (S³) to the Advanced Research Projects Agency (ARPA) and to the Air Force Office of Scientific Research (AFOSR).

The report presents the results obtained over the first twelve months of an eighteen-month effort designed to uncover the relation between earthquake ground motion and the nature of the earthquake source.

This research was supported by the Advanced Research Projects Agency of the Department of Defense and was monitored by the Air Force Office of Scientific Research under Contract No. F44620-72-C-0051. Mr. Donald C. Clements was the ARPA Program Manager and Col. Donald W. Klick the AFOSR Project Scientist.

Dr. J. T. Cherry was the S³ Project Manager for the study. Mr. E. J. Halda was responsible for the scientific programming associated with the ground motion calculations. Mr. K. G. Hamilton developed the computer codes required to process and display the results.

ABSTRACT

A stick-slip rupture model has been incorporated into a two-dimensional (plane strain) Lagrangian code with the added feature that rupture initiation is plastic work dependent.

Realistic laboratory test data have been used as input to the model. Theoretical seismograms have been generated in both the frequency and time domain along with a decomposition of the ground motion into P and S components.

The calculations suggest how estimates of fault length, rupture velocity and dynamic stress drop may be obtained from near field data. These estimates provide an initial specification of the parameters required by the rupture model in order to match a given set of near field data.

TABLE OF CONTENTS

	Page
FOREWORD	i
ABSTRACT	ii
I. INTRODUCTION	1
II. THE PHYSICS OF THE EARTHQUAKE SOURCE	4
III. CALCULATED GROUND MOTION RESULTING FROM THE STICK-SLIP RUPTURE MODEL	13
3.1 SUMMARY OF INPUT PARAMETERS	13
3.2 RADIATION PATTERNS	17
3.3 PEAK PARTICLE VELOCITY	36
3.4 DISPLACEMENT SPECTRA AND CORNER FREQUENCY	58
IV. SUMMARY	65
V. REFERENCES	68
APPENDIX I	70
APPENDIX II	77
APPENDIX III	83

I. INTRODUCTION

The elastic rebound theory, developed by H. F. Reid^[1] after the 1906 San Francisco earthquake identifies the immediate source of an earthquake as the release of accumulated strain energy in the rock mass surrounding a fault. This statement implies that the rupture process at the fault surface is responsible for the relative displacement across the fault and hence the seismic waves radiated during the earthquake. Almost sixty years passed before Benioff^[2] showed that the displacement at the fault inferred from the elastic rebound theory was consistent with seismological observations which suggested that the earthquake source function, for the radiated seismic energy, should be a double couple.

Following Benioff's work it became clear that an understanding of the nature of the earthquake source depended on an adequate simulation of fracture propagation over the fault plane. Analytic techniques were applied to the problem.

Analytic models have assumed either a moving dislocation^[3,4] or a prescribed stress relaxation^[5,6,7] in order to simulate the propagating rupture. Differences between these techniques should occur only because the assumed stress relaxation does not produce the same time history of relative displacement at the fault surface as that used during a specific exercise of the dislocation technique.

Obviously these analytic models assume the behavior of the equivalent elastic source at the fault surface. This assumption is stated either in a dislocation or stress relaxation format. If analytic techniques are to be used with confidence then arbitrary assumptions, regarding the behavior of the equivalent elastic source at the fault surface, must be removed.

When analytic models are used to match the free field ground motion from a specific earthquake in the region where the material response is linear-elastic, only then will the equivalent elastic source for the earthquake become available. The match implies that the analytic technique has used the correct description of the equivalent source at the fault surface.*

Free-field ground motion measurements from actual earthquakes do not exist. A few free surface, near field measurements have been made (for the Parkfield, June 28, 1966, and San Fernando, February 9, 1971, earthquakes) and more data of this type are certain to become available. It is important, therefore, that techniques be developed which are capable of:

1. Simulating the rupture process in such a manner that laboratory data from appropriate rock tests may be used to specify the parameters in the rupture model.
2. Calculating the theoretical, free-field seismograms caused by the rupture in order to obtain the equivalent elastic source.
3. Including the effect of the free surface and local site geology in order to compare calculated ground motion with free-surface, close-in measurements.

Lagrangian computer codes have been developed [8,9,10] which are capable of simulating the response of geologic materials to a propagating stress wave of arbitrary amplitude.

*Of course the actual behavior of the fault surface will be quite different from that specified by the equivalent source if nonlinear material behavior occurs during the rupture process. An analogous situation is encountered for spherical explosions in which the actual material response in the nonlinear region is different from that obtained using the equivalent elastic source (the reduced displacement potential).

These codes are capable of carrying the calculations into the small displacement, elastic region and yet flexible enough to permit very general material response formulations in the nonlinear region.^[11,12] They have been used extensively to both predict the effects of explosive sources on the surrounding rock environment^[13,14,15] and to obtain the equivalent elastic source as a function of rock type, depth of burial, and explosive yield.^[16,17]

In an attempt to at least partially satisfy the above three objectives, a stick-slip rupture model has been incorporated into a two-dimensional (plane strain) Lagrangian stress wave code. This earthquake model now furnishes the near source (free-field and free surface) ground motion caused by the stick-slip rupture process. The only limitation in the model is the plane strain assumption. This assumption implies an infinite fault dimension normal to the plane. If the calculations were carried to their far-field limit, they would correspond to a line source rather than a point source.*

In spite of this assumption, this two-dimensional fault model has provided a great deal of insight into the near field variation of peak particle velocity, corner frequency and displacement spectra with fault length, rupture velocity and stress drop. The physics of the source seems to be easy to simulate (certainly easier than nuclear explosions). The last remaining obstacle to be overcome, before teleseismic amplitude dependence can be related to the nature of the earthquake source, is the inclusion of the third space dimension in the model.

*Theoretical seismograms from this model would be appropriate for an actual earthquake having an out-of-plane fault dimension comparable to the distance between the fault and the seismometer.

II. THE PHYSICS OF THE EARTHQUAKE SOURCE

A formulation of the rupture process must provide quantitative answers to the following three questions:

1. Why does rupture occur?
2. What is the stress adjustment during rupture?
3. When does the rupture heal?

A stick-slip model of rupture has been formulated which answers the above questions as follows:

1. Rupture initiation is plastic work dependent.
2. During rupture the tangential stress at the slipping interface is relaxed to its kinetic friction value. This relaxation allows adjacent points on the interface to move apart (slip).
3. The rupture heals (adjacent points on the interface stick) if the relative velocity of two adjacent points changes sign and if the tangential stresses at the interface is sufficient to maintain continuity of tangential velocity.

A Lagrangian code is ideally suited to simulate a slipping interface. It is simply necessary to first decouple the grid line, over which slip is to occur, in order to isolate the normal and tangential components of stress at the interface (Equations 22 through 25, Appendix I) and second, to apply contact discontinuity boundary conditions, involving continuity of normal stress and normal velocity components, in order to solve for the normal stress component (Eq. 18, Appendix II). If the boundary point is "welded" (not slipping) then the tangential velocity component will also be continuous. This latter condition permits a unique solution for the

tangential stress at the welded point (Eq. 19, Appendix II). The basic mechanism for releasing the strain energy in this rupture model, is the relaxation of the tangential stress from its "welded" value to its "kinetic friction" value.

Figure 1 follows the tangential stress at two points on the fault surface (slipping interface) during a free-field calculation in which the stick-slip model was used to release the strain energy. For this particular calculation the fault length eventually grew to 10 km. The solid curve in the figure corresponds to the point on the fault where the rupture starts (the focus) while the dashed curve is for a point on the fault 2.5 km away. The initial value of tangential stress (τ_0) on the fault was one kbar. During rupture this stress component is relaxed to its kinetic friction value (τ_k). In this problem $\tau_k = 0.5$ kbar. The tangential stress is maintained at the τ_k value until adjacent points on each side of the fault reverse velocity. When the velocity reversal occurs, the points are tied (the fault sticks) if the tangential stress, required to maintain continuity of tangential velocity lies between $\pm \tau_k$. After the points are tied the tangential stress finds a static equilibrium value (τ_s).

Notice that for the point 2.5 km away from the beginning of the fault, the tangential stress builds to a maximum of 1.43 kbar due to stress differences parallel to the fault, before the plastic work criterion at this distance is violated. This occurs at 1.12 seconds; rupture begins and the tangential stress is relaxed to τ_k .

Figure 2 shows the final static level attained by the tangential stress over the 10-km fault. Results from all problems run to date indicate that at least one point on the fault will stick early and cause a mild stress concentration to occur in the static solution. In this figure the concentration occurs 3 km from the focus. Figure 2 also shows that most

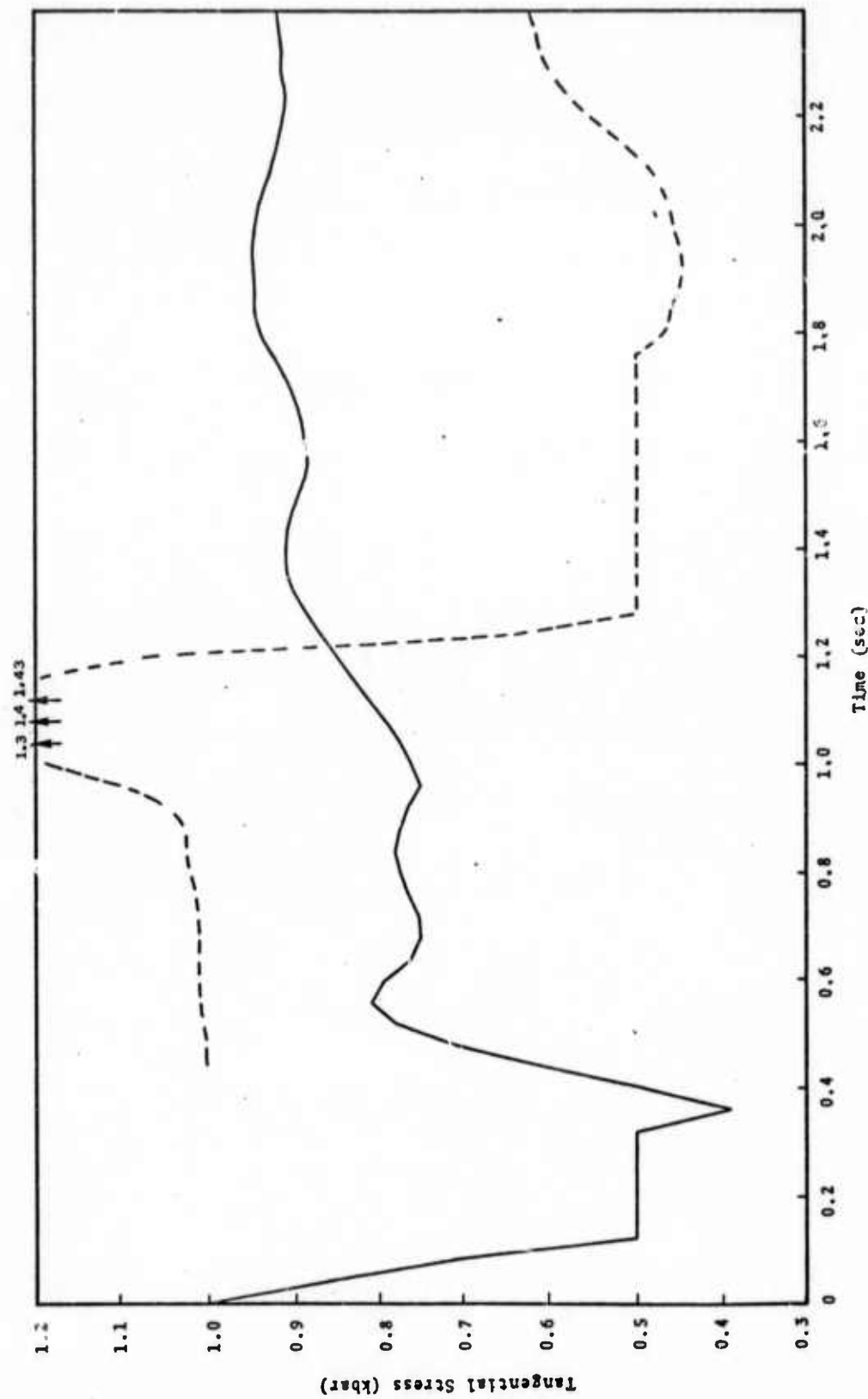


Fig. 1--Tangential stress versus time at two points 2.5 km apart on the fault.

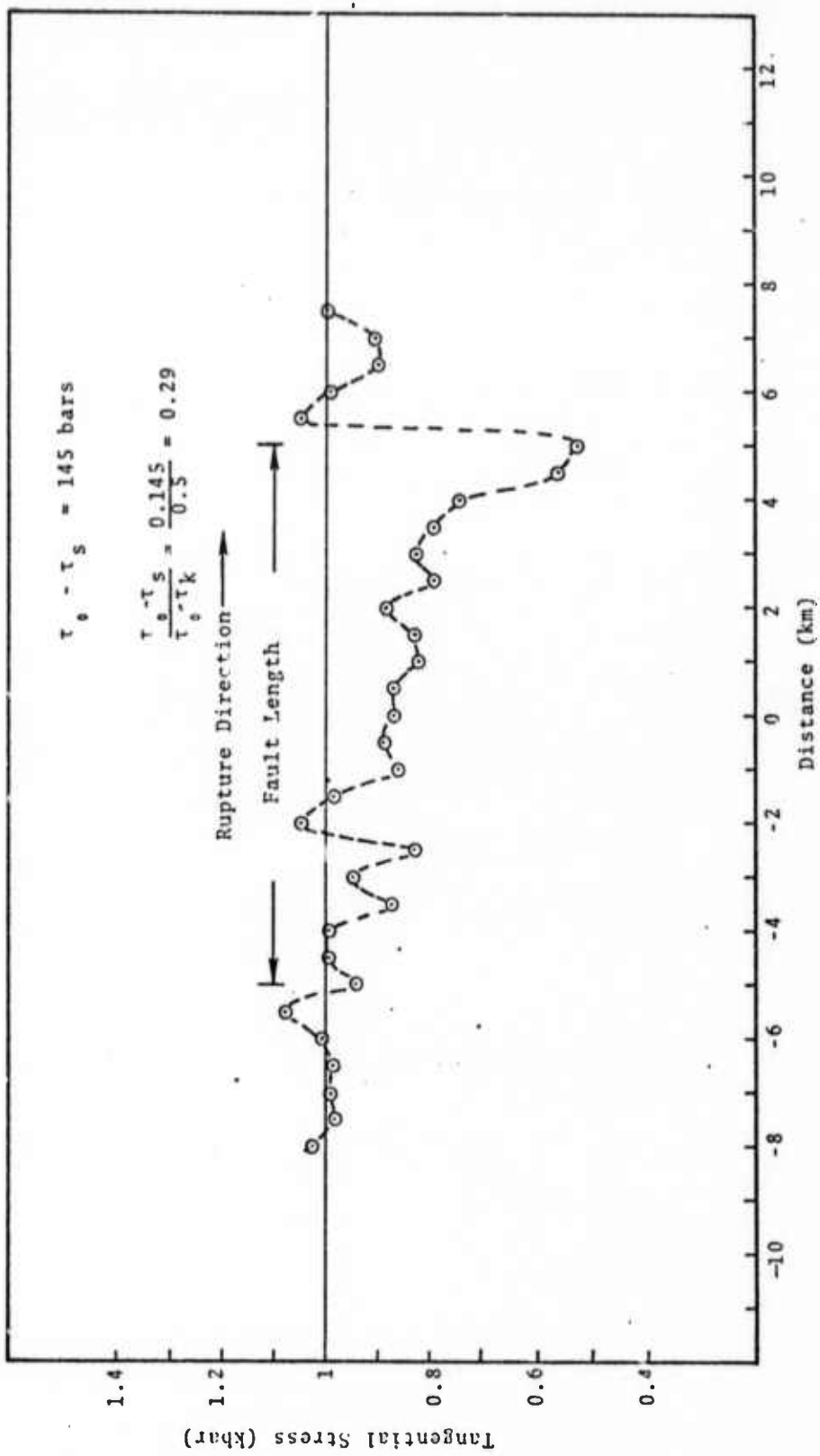


Fig. 2--Static value of tangential stress on fault.

of the static stress drop occurs at the end of the fault where the rupture stops; a result that is again common to all calculations having a finite rupture velocity.

Figure 3 shows the relative displacement over the fault at 0.4-second intervals. The point that ties early at 3 km is responsible for the stress concentration at that distance in Fig. 2.

The rupture velocity over the first 7 km of the fault was 2.15 km/sec. At this distance the plastic work criterion was increased so that the rupture would not stop abruptly. Figure 4 shows the arrival time of the rupture versus distance along the fault. Over the last 3 km the rupture velocity is approximately 1.6 km/sec, giving an average rupture velocity over the entire fault of 2 km/sec.

Plastic flow is due to the inability of real geologic materials to support unlimited values of shear stress. The deviatoric stress components in the yielding element are modified such that the resulting stress state is consistent with a Mises yield criterion (Eq. 1, Appendix III).

Initially, plastic flow was included in the model in order to remove the large stress concentrations that occurred at the ends of the rupture during calculations involving only linear, elastic material behavior. It was immediately found that rupture velocity could be controlled by allowing rupture initiation to be dependent on the plastic work dissipated during the yielding process (Eqs. 3 through 5, Appendix III).

There is experimental evidence^[18] that crystalline rocks undergo significant yielding prior to brittle failure at the temperatures and pressures appropriate even for shallow earthquakes (focal depths of around 10 km). We have allowed this mechanism to control the rupture velocity by specifying the plastic work for rupture to be a function of distance from

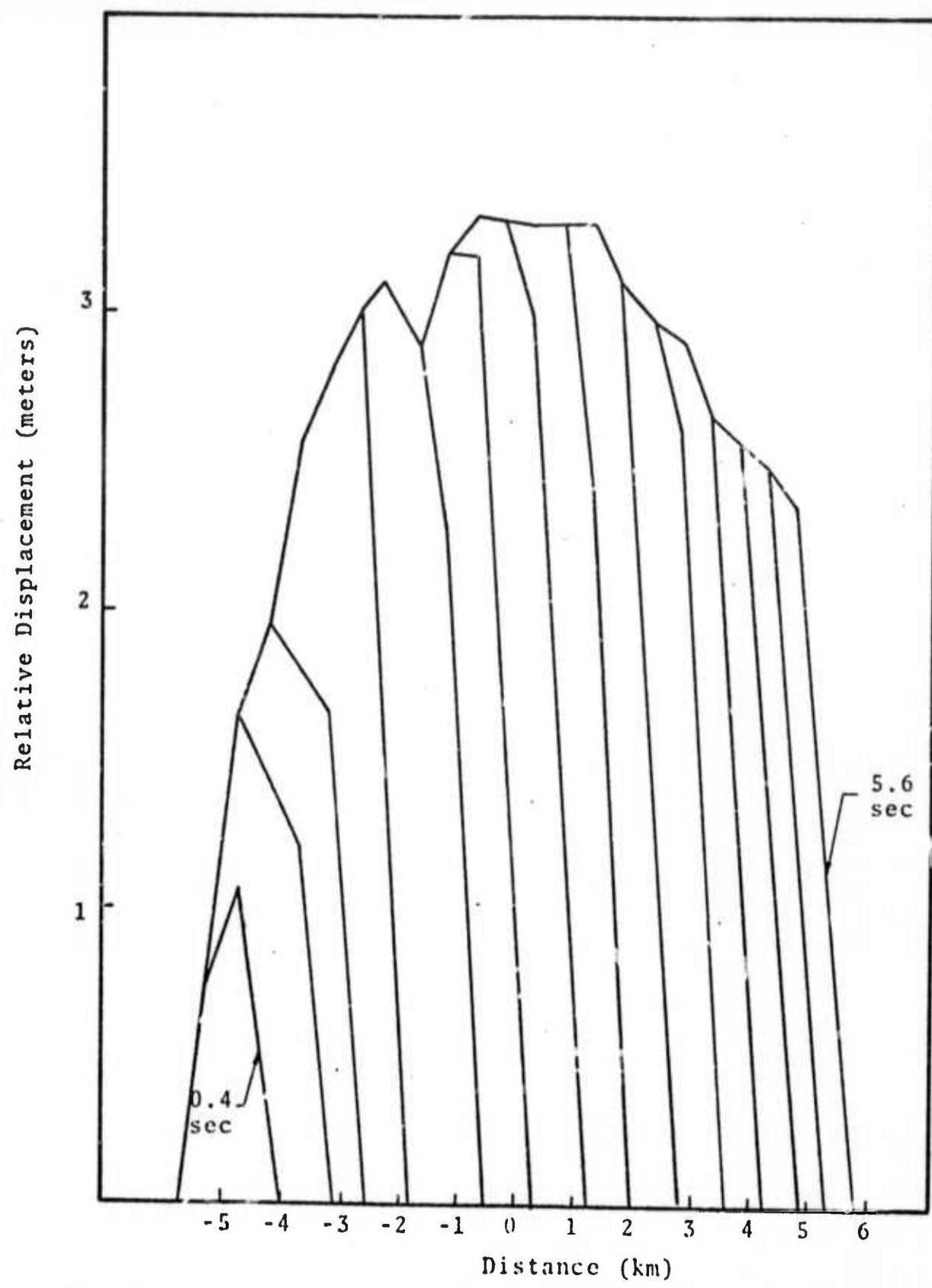


Fig. 3--Relative displacement on 10 km fault at 0.4 sec intervals.

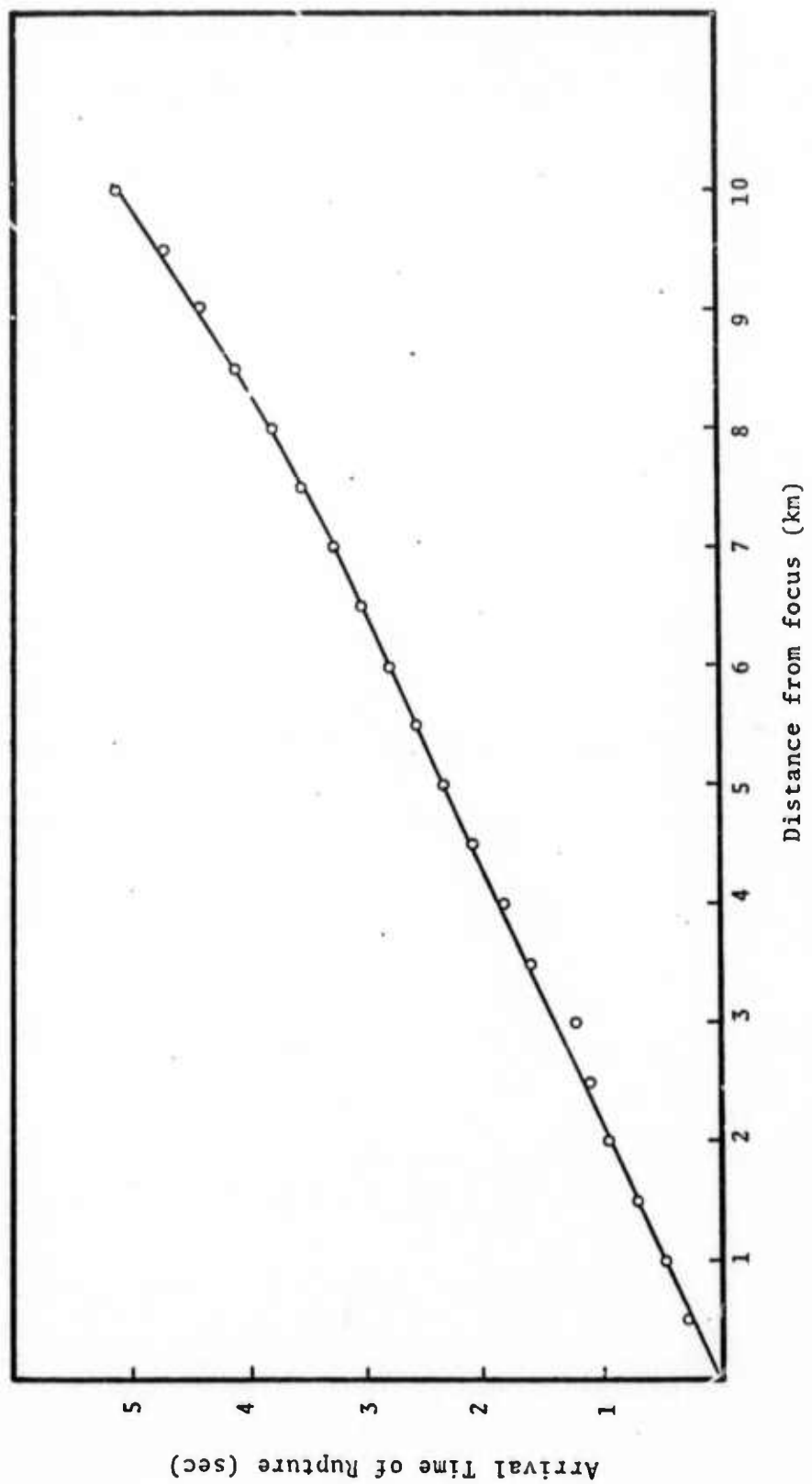


Fig. 4--Arrival time of the rupture versus distance along the fault.

the focus (Eq. 6, Appendix III). This requires not only that the dimensions of the fault zone be specified, but also the relation between the yield surface and the stress state in the fault zone.

The calculations reported in the next section were obtained assuming an elliptical fault zone with all the material in the fault zone initially lying on the yield surface, i.e., an attempt to increase the second deviatoric invariant above its initial value in the fault zone causes plastic flow and therefore plastic work.

The code, of course, is not limited to a plastic work rupture criterion. In the code, the components of stress have been isolated at the fault surface and a rupture criterion could easily be formulated in terms of these stress components.

For example, the tangential stress could initially be limited at the boundary. This would allow the fault to slide stably, i.e., creep. (In Fig. 1, a creep event would occur at 2.5 km if the allowable tangential stress at this distance was less than 1.43 kbar). The drop in tangential stress to its kinetic friction value (rupture) could then be made a function of the size of the creep event. Stable sliding has been observed, prior to rupture, in laboratory stick-slip events in plates of Westerly granite.^[19] Creep may prepare the fault surface for rupture by polishing the surface. Rupture velocity could be controlled by varying the magnitude of the creep event required to cause the tangential stress to drop to its kinetic friction value.

Frictional sliding on ground surfaces of granite has been investigated by Byerlee.^[20] For normal stresses (σ_n) varying between 2 - 12 kbar over the surface, he found that the tangential stress drop from static friction (τ_s) to kinetic friction (τ_k) is given by

$$\tau_0 - \tau_k = 0.25 + 0.13 \sigma_n \quad (\text{all units in kbars}) \quad (2.1)$$

While this relation was established for specimens at room temperature and for specially prepared surfaces, it probably furnishes an upper limit to the allowable dynamic stress drop for shallow earthquakes. Laboratory experiments should be performed in order to (1) determine the effect of temperature on dynamic stress drop and (2) to determine the amount of inelastic work required to cause stick-slip. Results of these experiments would provide the input required by the stick-slip rupture model.

III. CALCULATED GROUND MOTION RESULTING FROM THE STICK-SLIP RUPTURE MODEL

3.1 SUMMARY OF INPUT PARAMETERS

In order to exercise the rupture model in its current form, a number of parameters must be specified. These are:

- The Fault Zone. An elliptical fault zone, defined as

$$\frac{x^2}{a^2} + \frac{y^2}{b^2} = 1 \quad (3.1)$$

was assumed with all the material in the fault zone initially lying on the yield surface. The origin of the x-y coordinate system is located at the center of the fault, as shown in Fig. 5. Elastic behavior was assumed for the material outside the fault zone. The minor axis, b , was 2 km for all calculations. The major axis, a , extended 3 km beyond the end of the fault.

- The Plastic Work Required for Rupture Initiation.

A unidirectional rupture was assumed as shown in Fig. 5. For a given fault length, L , the functional form used to initiate rupture within the interval $-L/2 \leq x \leq L/2$ was assumed to be (Appendix III, Eq. 6)

$$W = 6c \left(\frac{x+L/2}{d} \right) \left[\frac{1}{2} - \frac{1}{3} \frac{x+L/2}{d} \right] \quad \left(0 \leq x + \frac{L}{2} \leq \frac{d}{2} \right) \quad (3.2a)$$

$$W = \frac{c}{2} \left[-\frac{1}{2} + 3 \frac{x+L/2}{d} \right] \quad \left(x + \frac{L}{2} \geq \frac{d}{2} \right) \quad (3.2b)$$

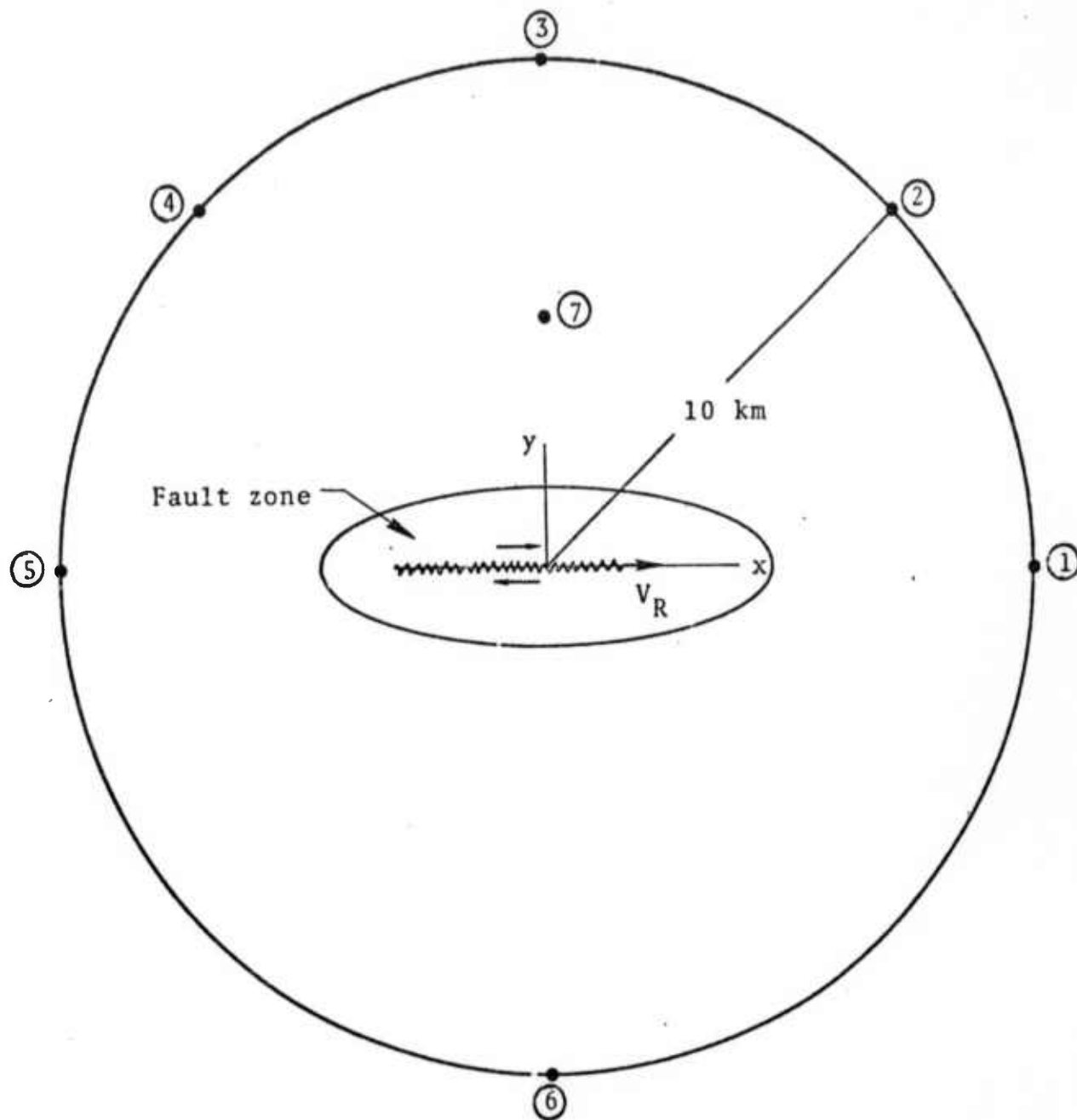


Fig. 5--Stations monitored during calculation. The origin of the x-y coordinate system is in the center of the fault.

Rupture starts at $x = -L/2$ ($W = 0$) and is assumed to terminate at $x = L/2$. In the calculations, rupturing was not permitted outside the interval $-L/2 \leq x \leq L/2$.

- The Stress Drop During Rupture ($\tau_0 - \tau_k$). It was found that the normal stress (σ_n) on the fault did not change from its initial value during the calculation. Therefore, the assumed stress drop remained constant over the fault. Equation (2.1) was used as a guide for this quantity and calculations were obtained for stress drops of 0.25 and 0.5 kbars. The initial stress (τ_0) was the same for all calculations with $\tau_0 = 1$ kbar.
- The Shear Modulus (μ), Bulk Modulus (k) and Density (ρ). These quantities were maintained constant for all calculations, with $\mu = 324$ kbar, $k = 478$ kbar and $\rho = 2.8$ g/cc. The corresponding compression (α) and shear (β) wave velocities are $\alpha = 5.7$ km/sec, $\beta = 3.4$ km/sec.

Table I summarizes the input parameters ($a, c, d, L, \tau_0 - \tau_k$) along with the rupture velocity (V_r) and static stress drop ($\tau_0 - \tau_s$) that resulted from the four calculations. Since α, β, ρ, b , and τ_0 were the same for all calculations, these parameters are not listed in the table.

TABLE I

Calculation	a(km)	c	d(km)	L(km)	$\tau_0 - \tau_k$ (kbar)	V_R (km/sec)	$\tau_0 - \tau_s$ (kbar)
10A	8	0.7	10	10	0.5	2.0	0.146
5A	5.5	0.7	10	5	0.5	2.15	0.178
5B	5.5	0.4	10	5	0.5	3.75	0.224
5C	5.5	0.4	10	5	0.25	2.15	0.110

3.2 RADIATION PATTERNS

All ground motion calculations are easily separable into P and S components. This is accomplished by monitoring the divergence ($\nabla \cdot \vec{s}$) and curl ($\nabla \times \vec{s}$) of the displacement field at selected points in the elastic regime.

The equation of motion for a linear elastic stress wave is

$$\frac{\partial^2 \vec{s}}{\partial t^2} = \alpha^2 \nabla (\nabla \cdot \vec{s}) - \beta^2 \nabla \times (\nabla \times \vec{s}) \quad (3.3)$$

where \vec{s} is particle displacement and α and β are the compression and shear velocities. If \vec{s} is separated into a scalar (ϕ) and vector (\vec{x}) potential, then

$$\vec{s} = -\nabla \phi - \nabla \times \vec{x} \quad (\nabla \cdot \vec{x} = 0) \quad (3.4)$$

Substituting Eq. (3.4) into Eq. (3.3) gives the scalar and vector wave equations

$$\frac{\partial^2 \phi}{\partial t^2} = \alpha^2 \nabla^2 \phi \quad (3.5)$$

$$\frac{\partial^2 \vec{x}}{\partial t^2} = \beta^2 \nabla^2 \vec{x} \quad (3.6)$$

Hooke's law gives

$$p = -k \nabla \cdot \vec{s} \quad (3.7)$$

where k is the bulk modulus, and p is the pressure component of the stress tensor. Also, since $\nabla \cdot (\nabla \times \vec{x}) = 0$, then from Eq. (2)

$$\nabla \cdot \vec{s} = -\nabla^2 \phi \quad (3.8)$$

Using Eqs. (3.5), (3.7) and (3.8) gives

$$\frac{\partial^2 \phi}{\partial t^2} = \frac{\alpha^2}{k} p = \left(\frac{1 + \frac{4}{3} \frac{\mu}{k}}{\rho} \right) p \quad (3.9)$$

where μ is the shear modulus and ρ the density. Therefore $\ddot{\phi}$ is easily obtained from a calculation since p is a saved variable in the code.

$$\text{Since } \nabla \times (\nabla \phi) = 0 \text{ and } \nabla \times (\nabla \times \vec{\chi}) = -\nabla^2 \vec{\chi}$$

then Eq. (3.4) gives

$$\nabla \times \vec{s} = \nabla^2 \vec{\chi} \quad (3.10)$$

Equations (3.6) and (3.10) give

$$\frac{\partial^2 \vec{\chi}}{\partial t^2} = \beta^2 (\nabla \times \vec{s}) \text{ where } \beta^2 = \frac{\mu}{\rho} \quad (3.11)$$

The quantity $\nabla \times \vec{s}$ is proportional to the rotation of a line element and is also a saved variable in the code. Therefore $\vec{\chi}$ is readily available from the calculations. The form of Eq. (3.11) used in the code is

$$\ddot{\chi}(t) = \frac{\mu}{\rho} \int_0^t \left(\frac{\partial \dot{y}}{\partial x} - \frac{\partial \dot{x}}{\partial y} \right) dt \quad (3.12)$$

where \dot{x} and \dot{y} are particle velocities in the x and y directions.

Equations (3.9) and (3.12) permit the calculated ground motion to be separated into P and S components. A positive value of $\ddot{\phi}$ corresponds to a compression ($p > 0$) while a positive value of $\ddot{\chi}$ gives a clockwise body rotation.

Figure 5 shows the stations monitored during each calculation. The origin of the x-y coordinate system is located at the center of the fault. The rupture velocity was unidirectional and propagated in the positive x direction.

Figures 6 through 13 show the $P(\ddot{\phi})$ and $S(\ddot{x})$ radiation patterns from the four calculations. These figures give the peak values of the two potentials at all stations located 10 km from the center of the fault. The finite rupture velocity produces a noticeable Doppler effect in the radiation patterns, with the S component in the fault plane (in the rupture direction) approximately 2.5 times larger than the S components in the auxiliary plane. The same factor applies to the S_{\max}/P_{\max} ratio.

While the value for S_{\max} in the auxiliary plane is real, the peaks in the other lobes in both P and S may have been missed. This is due to an inadequate azimuthal sampling along the 10-km radius (Fig. 5). While this will be remedied in future calculations, it appears that the routine for P and S separation produces acceptable radiation patterns.

Figures 14 through 21 give the full time history of $\ddot{\phi}$ and \ddot{x} at Station 2 for the four calculations and show the basic difference between an earthquake source and a center of dilatation (an explosion). The center of dilatation gives a scalar potential (ϕ) that resembles $\ddot{\phi}$ for an earthquake. Of course the vector potential vanishes for the center of dilatation. The calculations show that the earthquake source produces static, azimuthally dependent values of pressure (Eq. (3.9)) and body rotation (Eq. (3.12)). This feature should cause an increase in surface wave excitation for earthquakes relative to explosions and may be responsible for the effectiveness of the M_s/m_b discriminant.

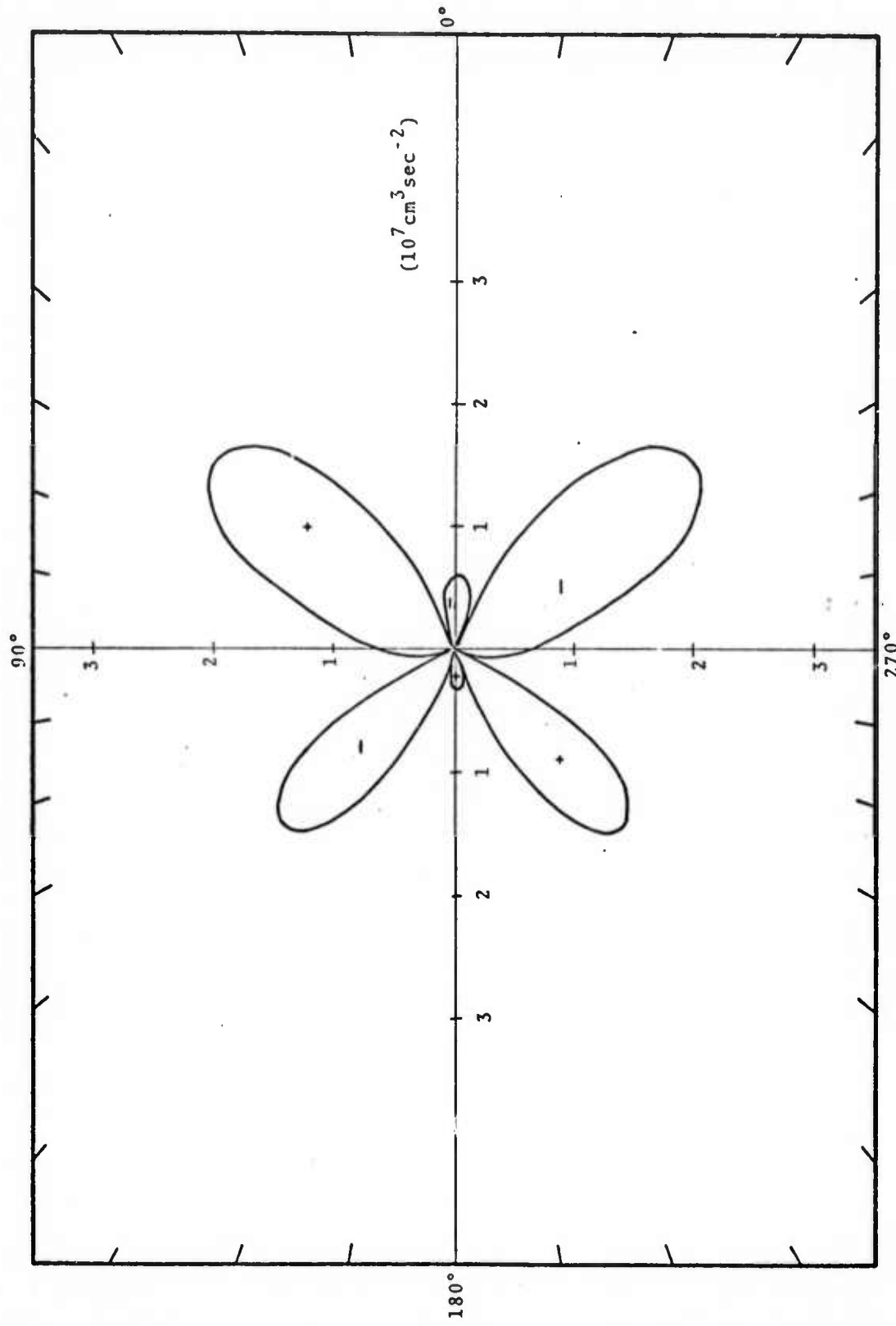


Fig. 6--P radiation from calculation 10A.

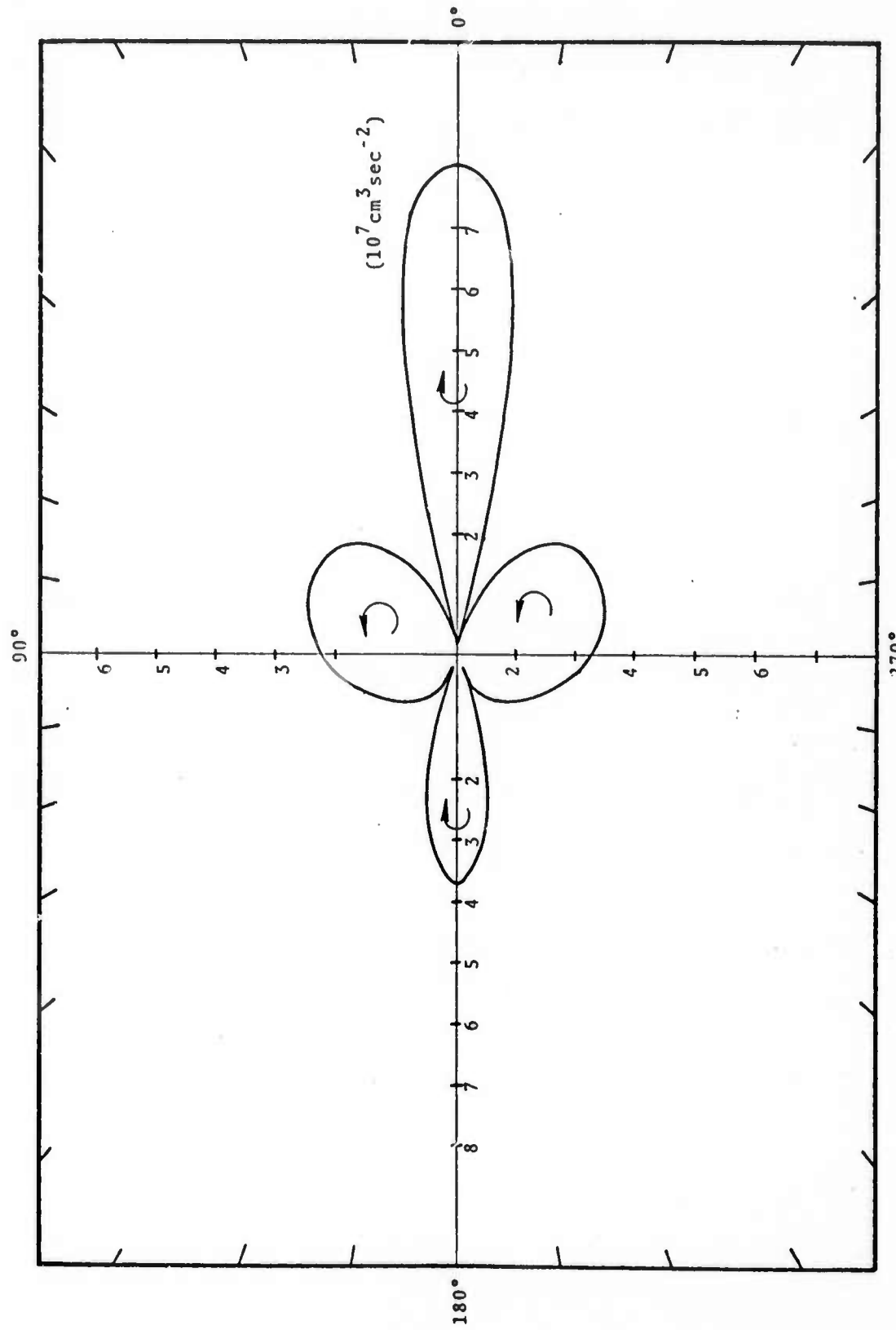


Fig. 7--S radiation from calculation 10A.

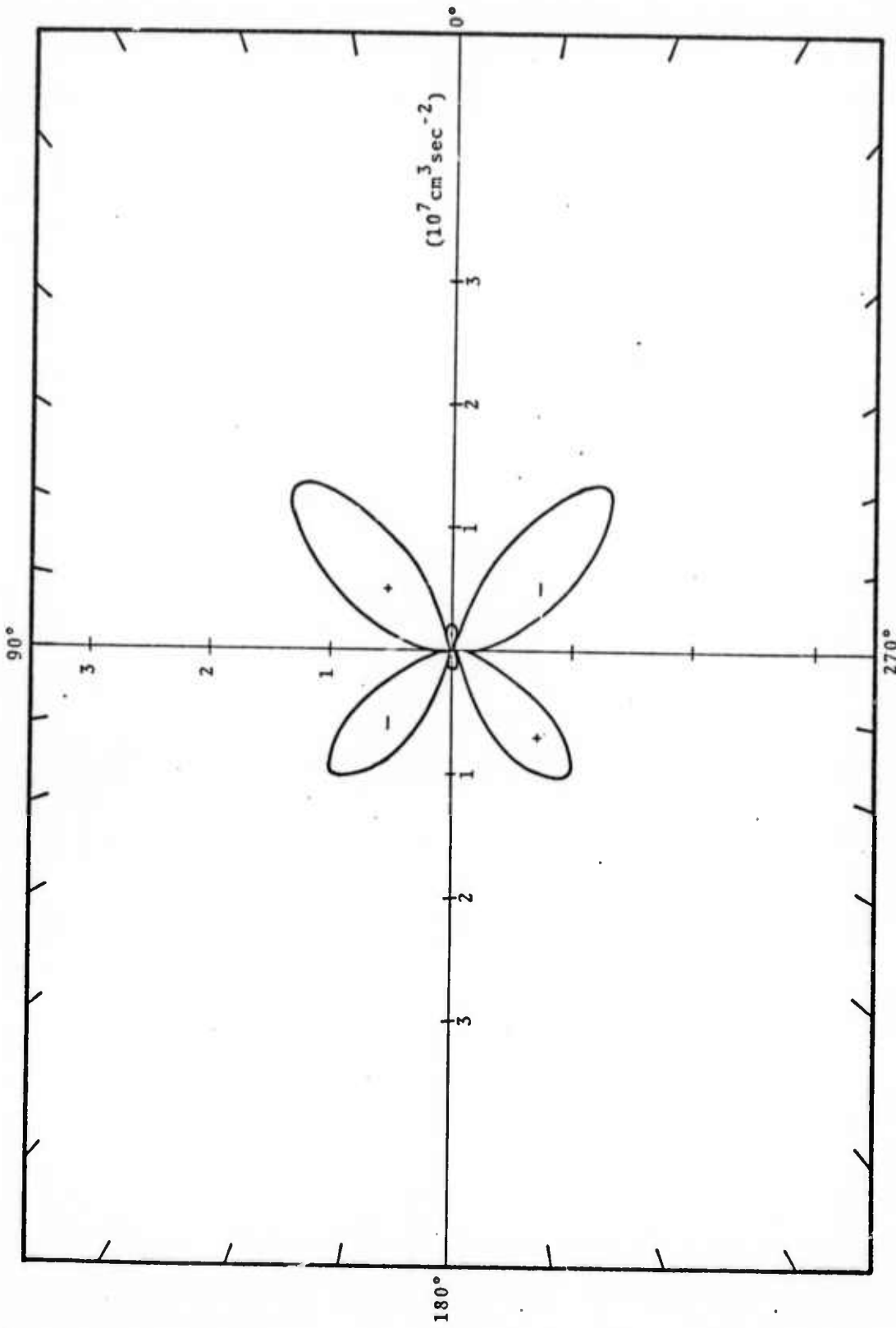


Fig. 8--P radiation from calculation 5A.

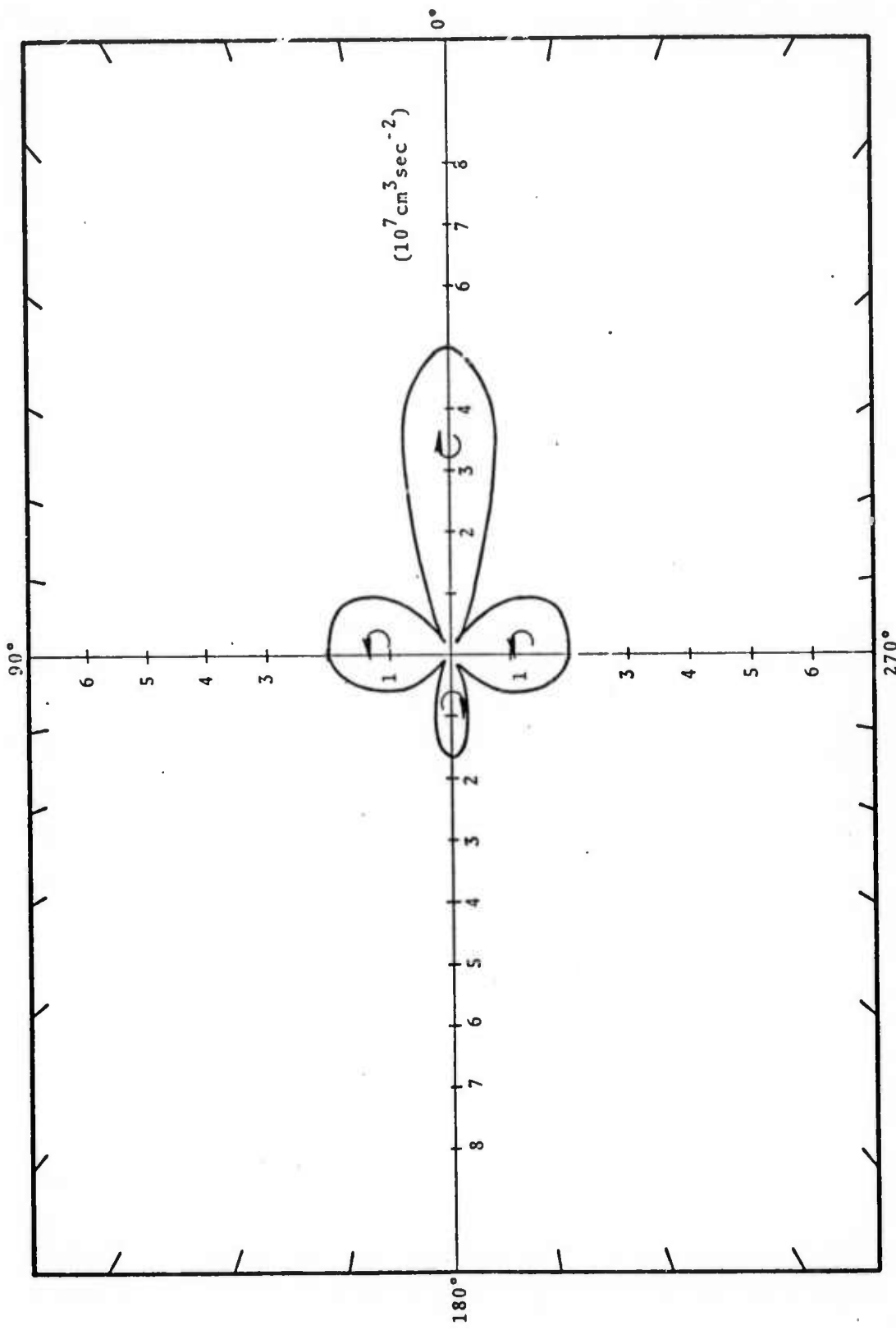


Fig. 9--S radiation from calculation 5A.

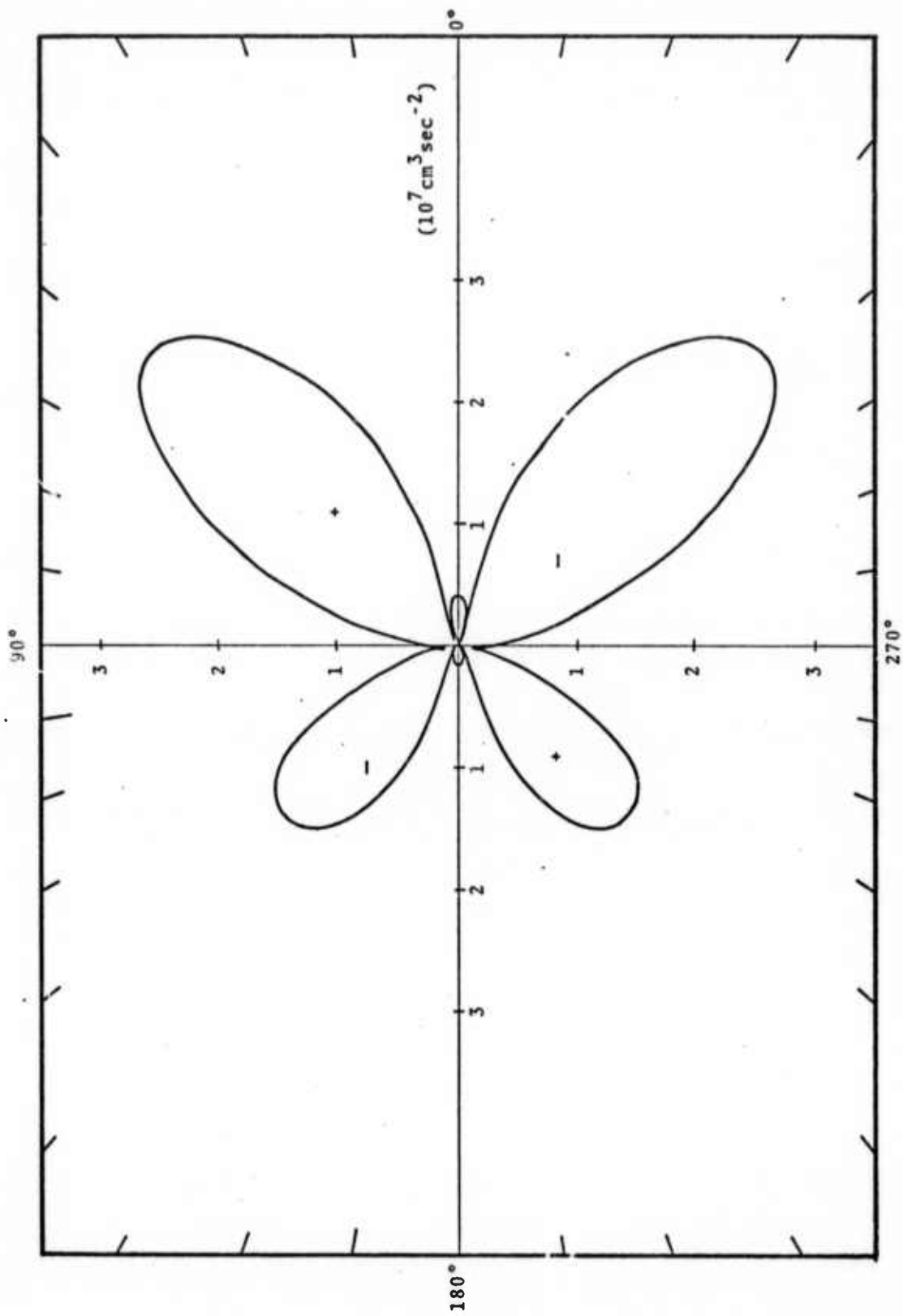


Fig. 10--P radiation from calculation 5B.

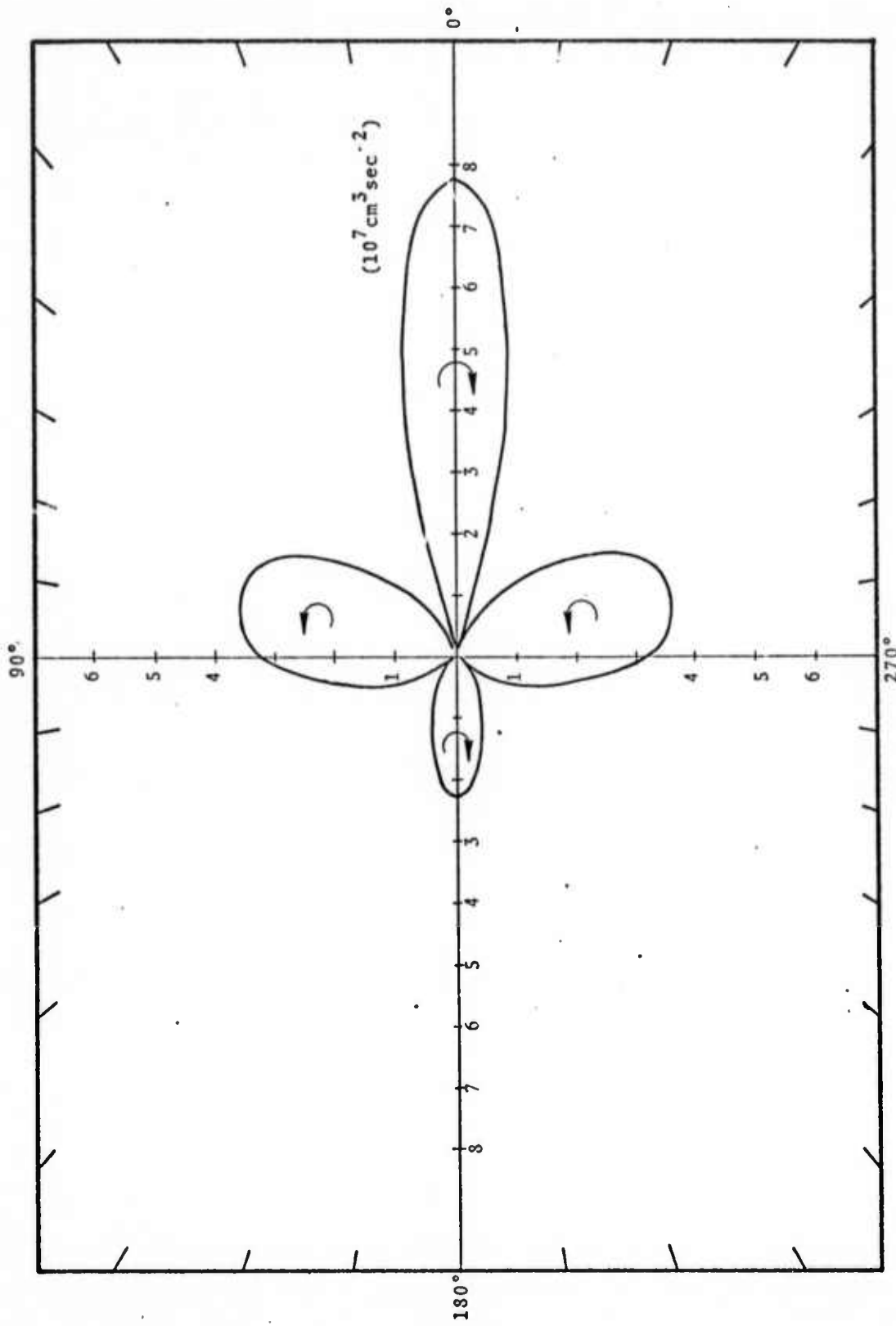


Fig. 11--S radiation from calculation 5B.

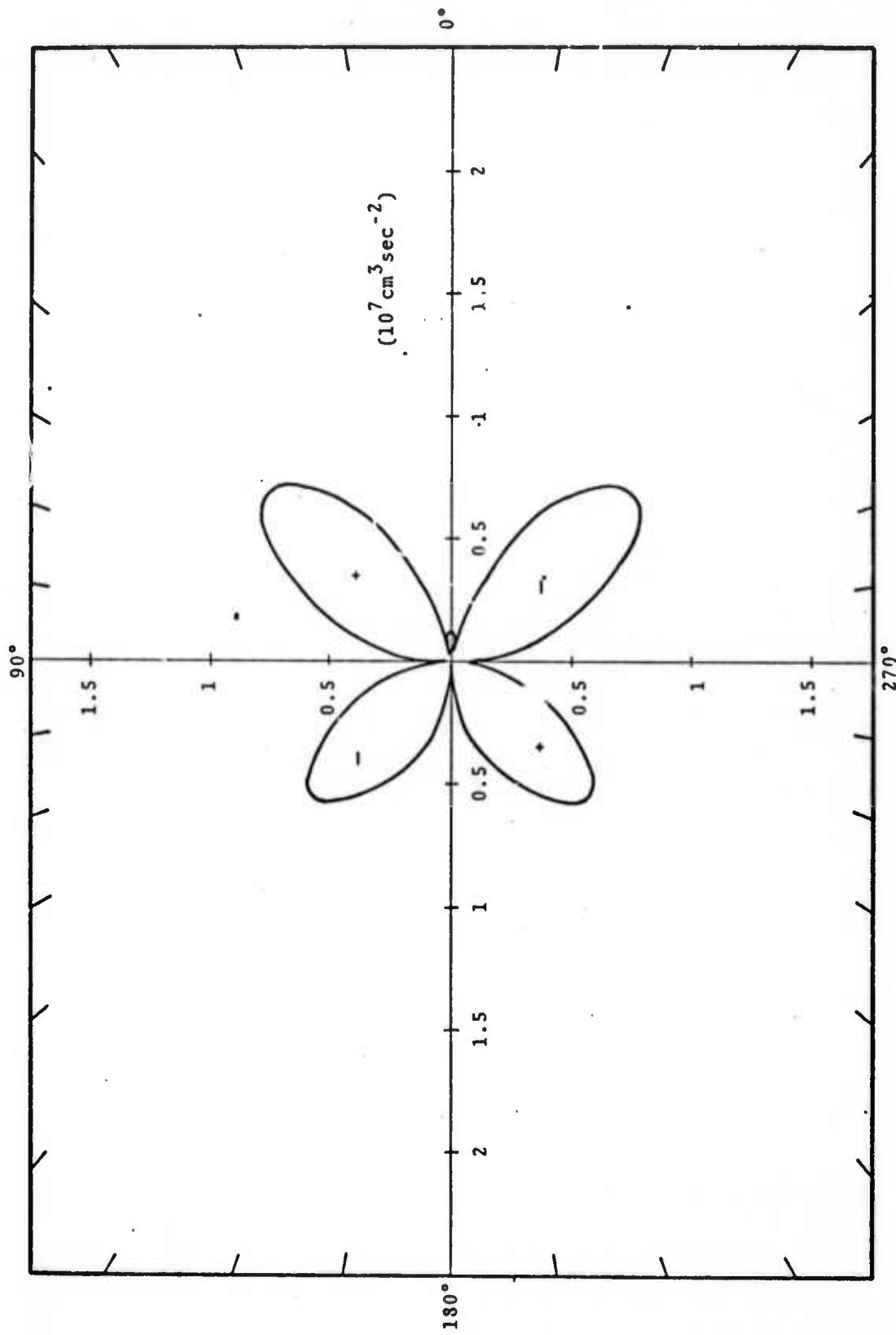


Fig. 12--P radiation from calculation 5C.

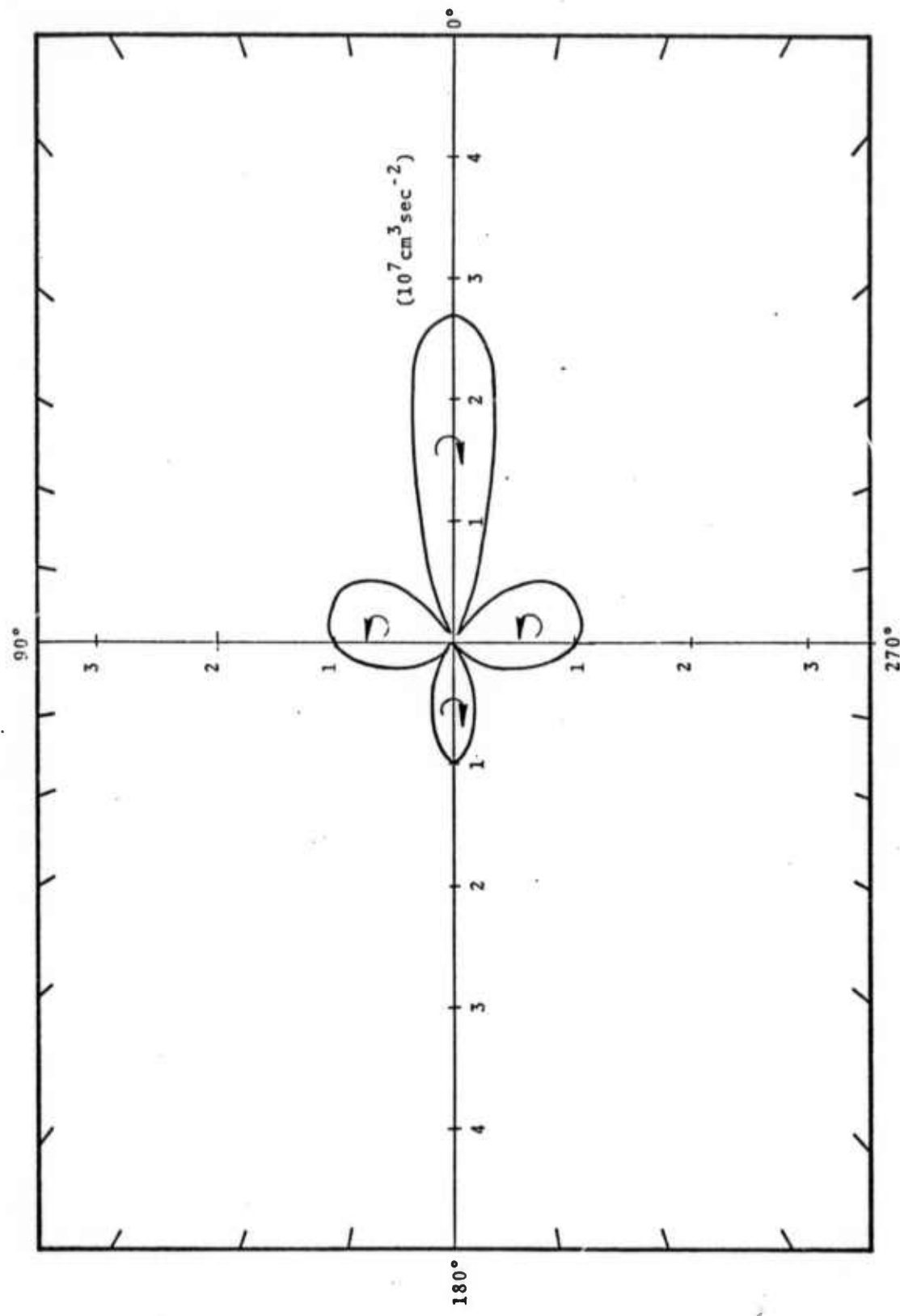


Fig. 13--S radiation from calculation 5C.

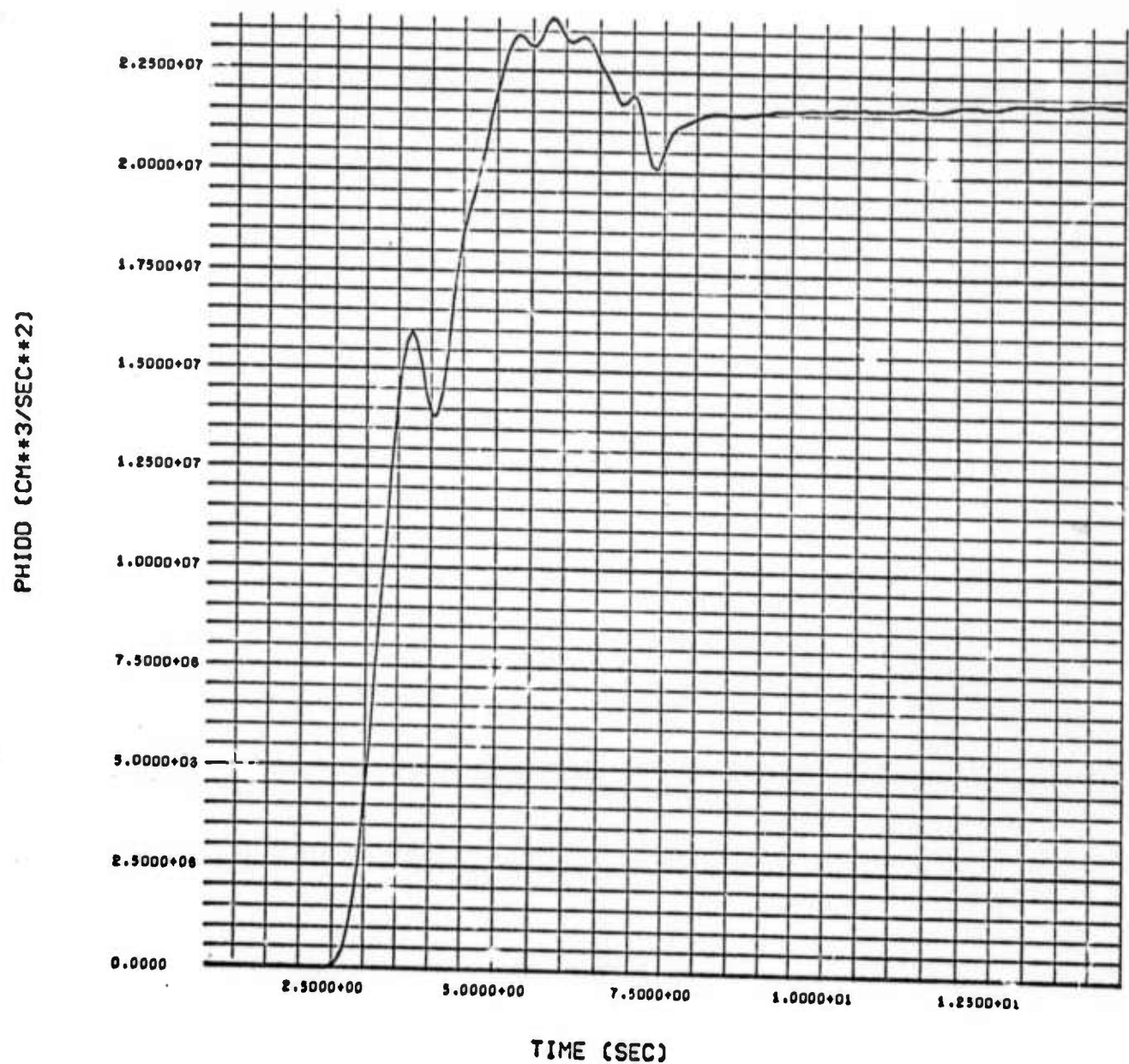


Fig. 14--Time history of scalar potential (ϕ) at Station 2, 10A.

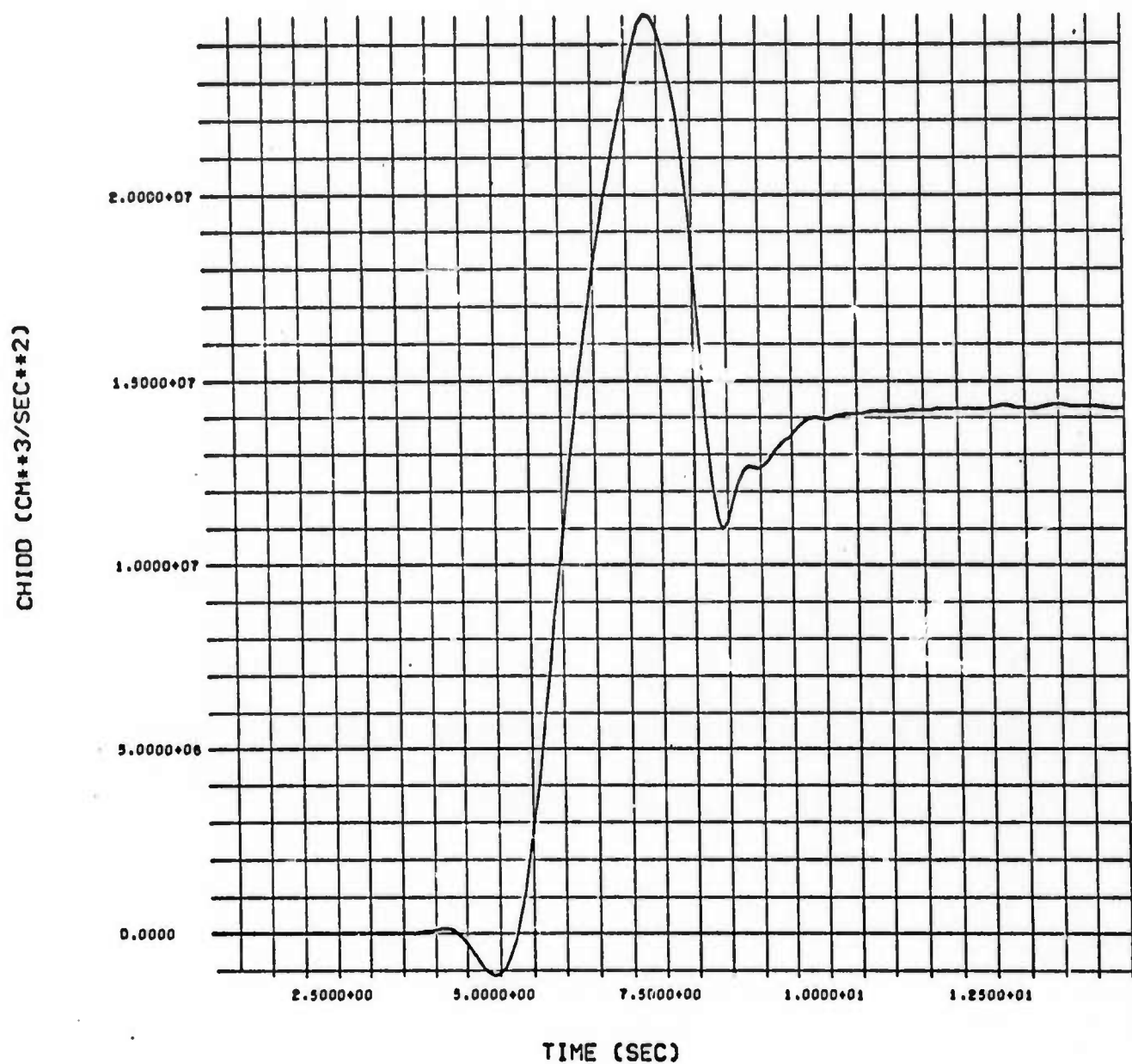


Fig. 15--Time history of vector potential (\ddot{X}) at Station 2, 10A.

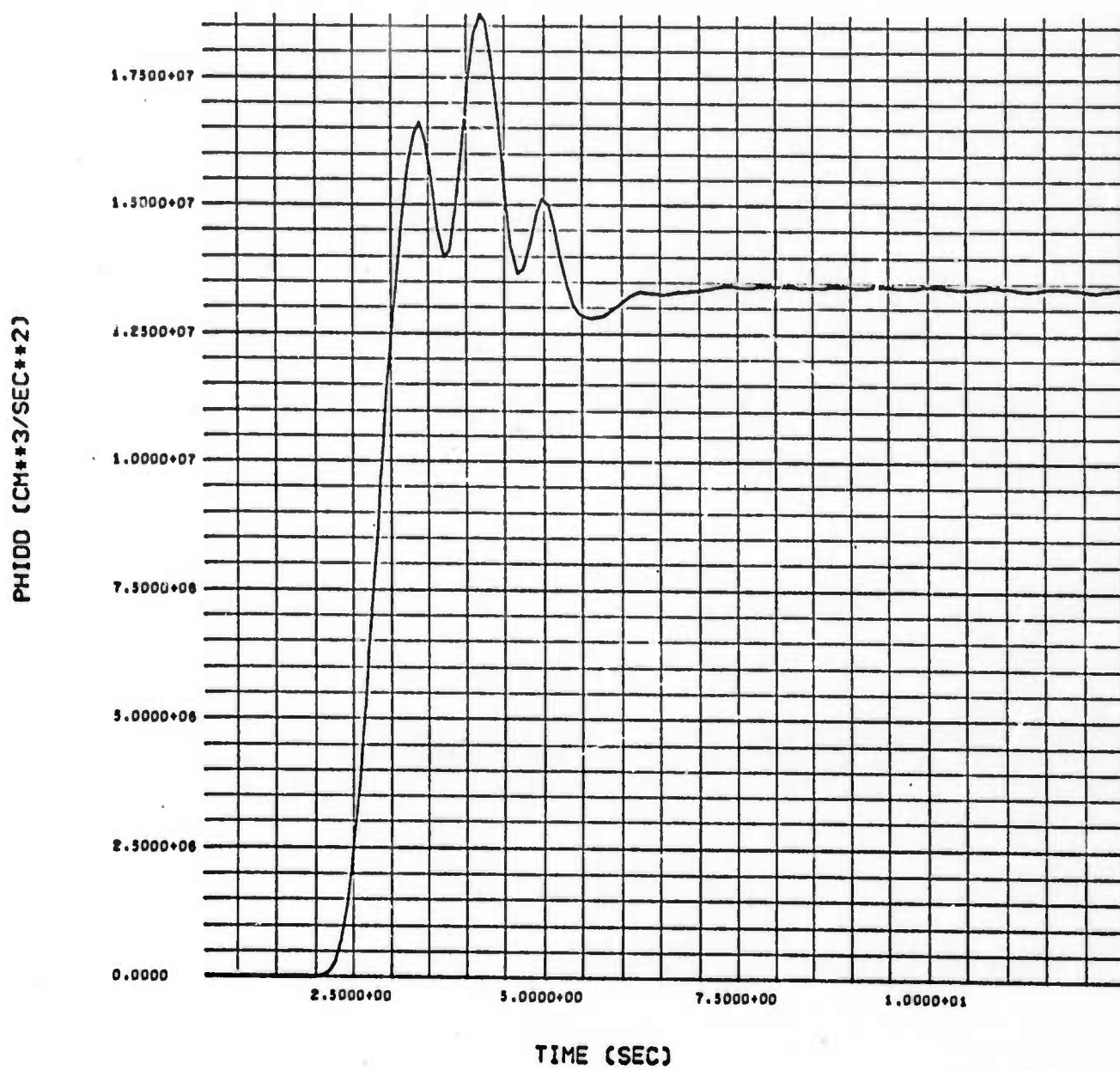


Fig. 16--Time history of scalar potential (ϕ) at Station 2, 5A.

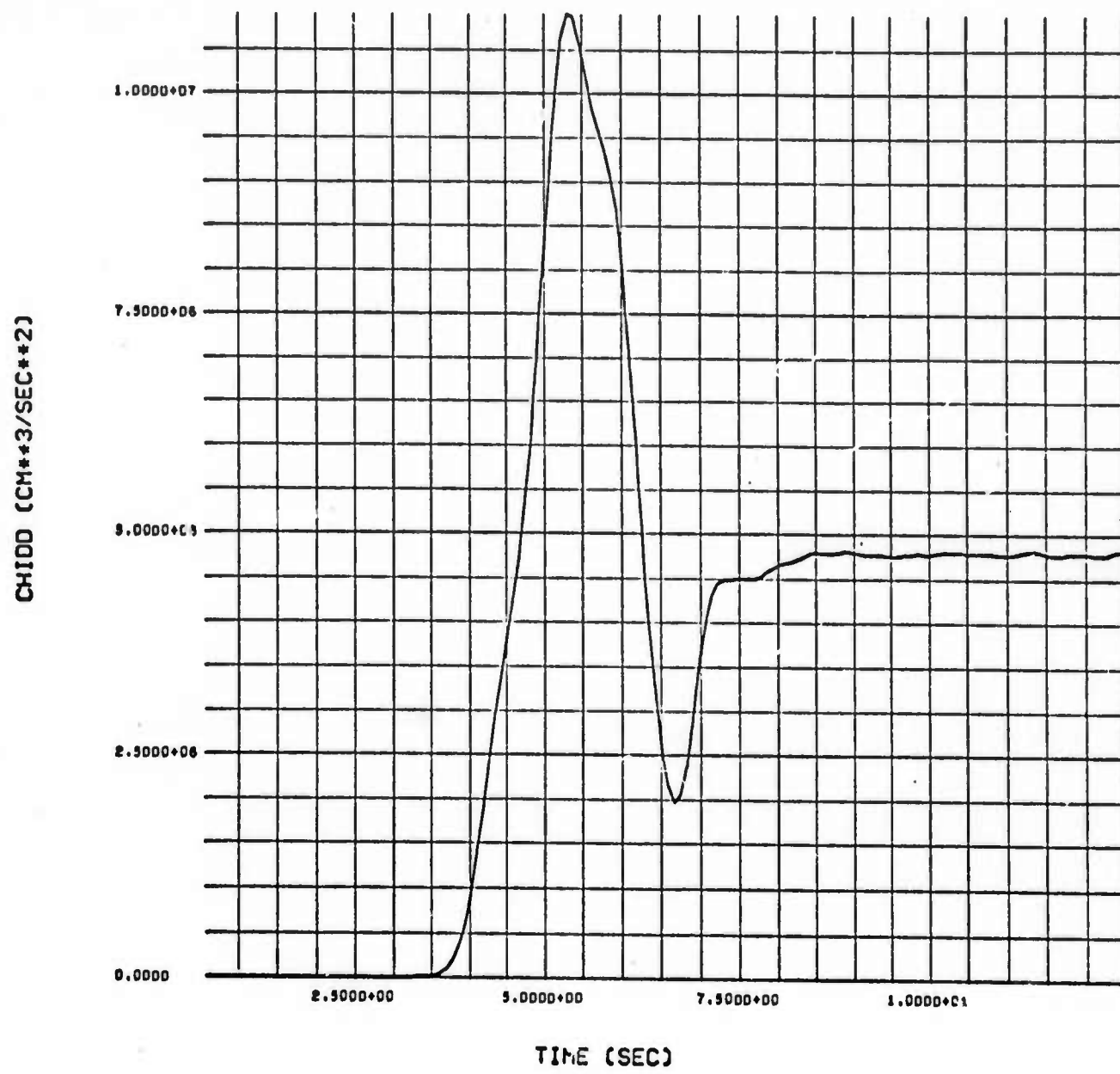


Fig. 17--Time history of vector potential (\ddot{X}) at Station 2, 5A.

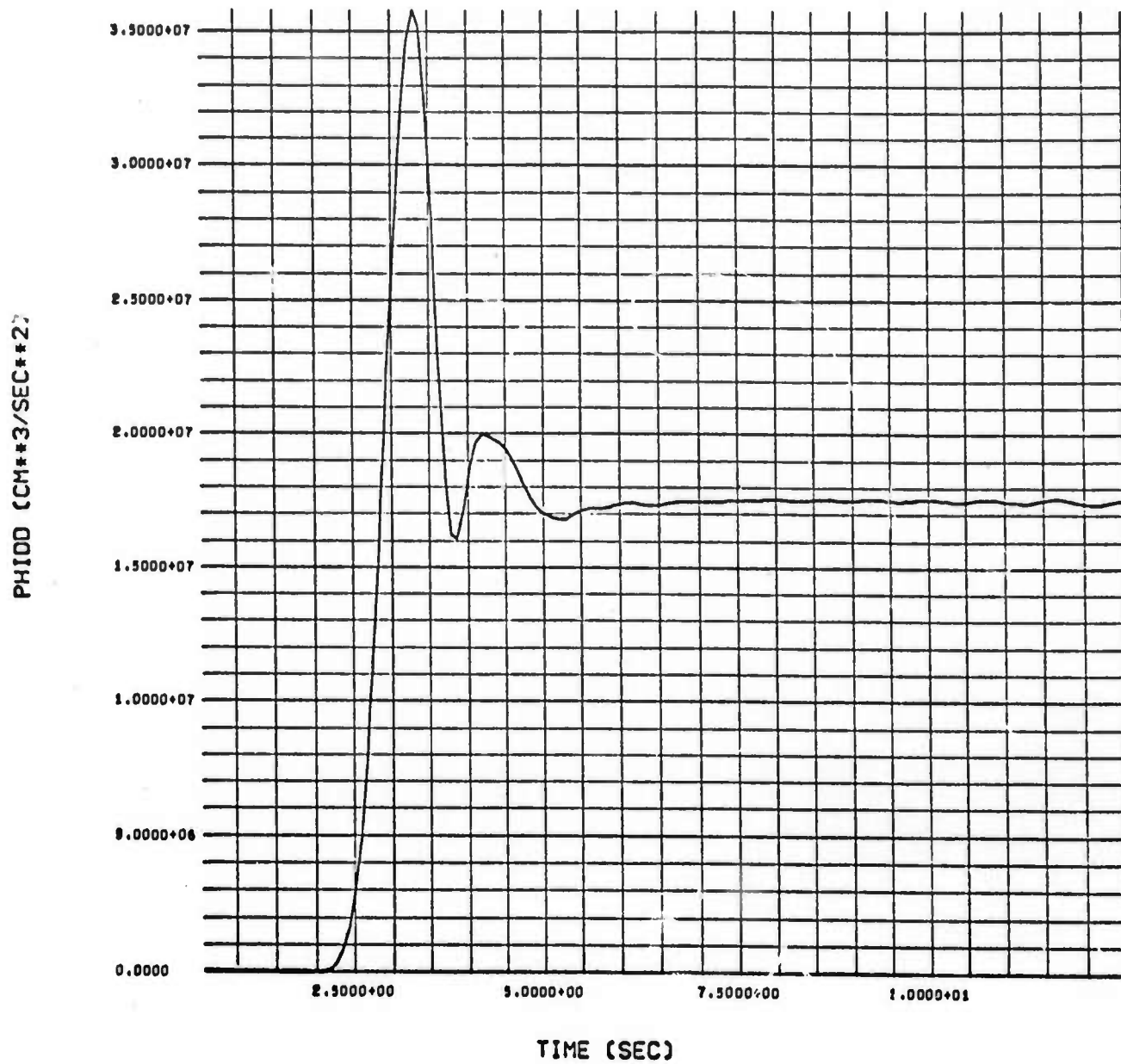


Fig. 18--Time history of scalar potential (ϕ) at Station 2, 5B.

CH100 (CH**3/SEC**2)

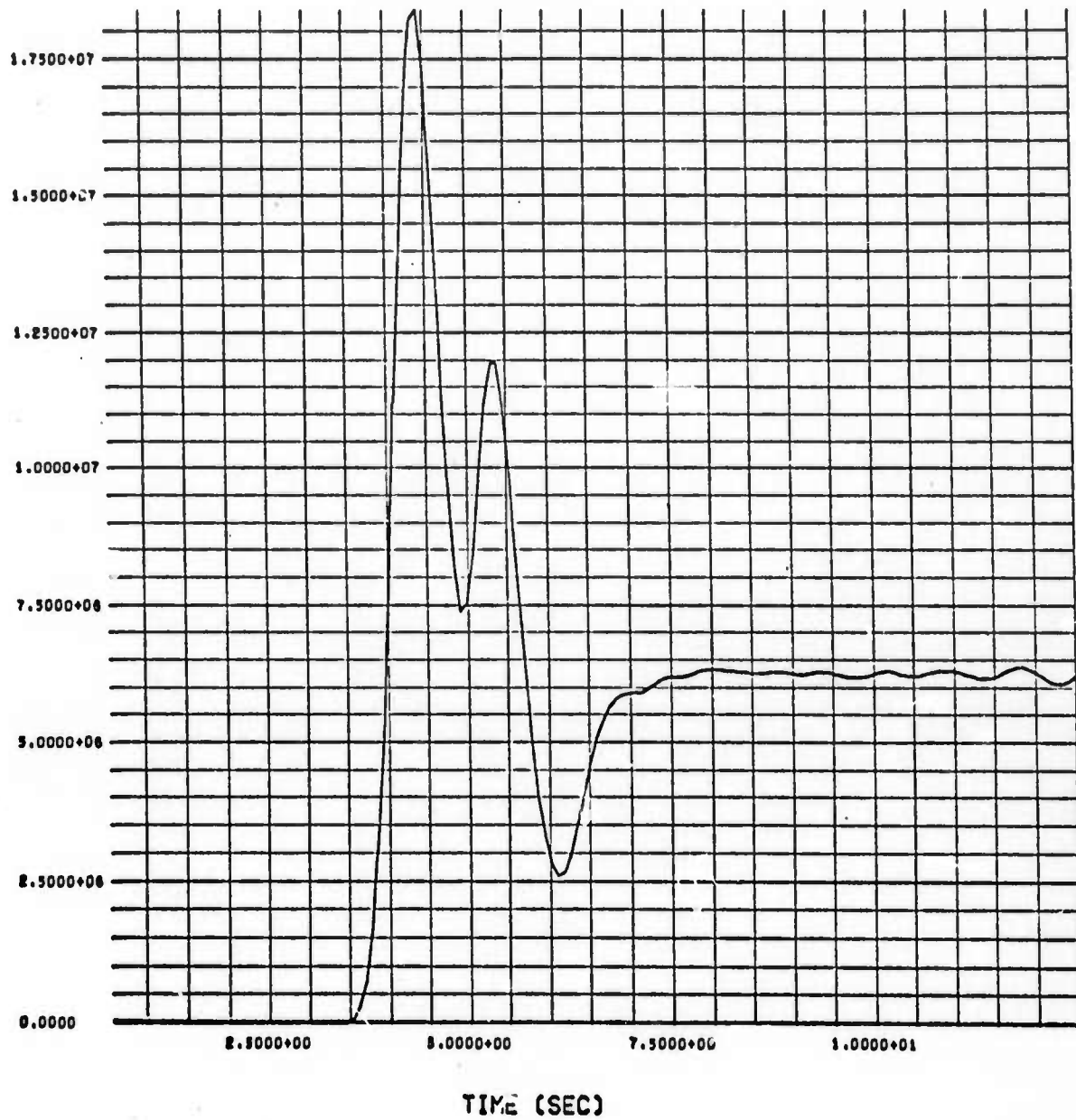


Fig. 19--Time history of vector potential ($\ddot{\chi}$) at Station 2, 5B.

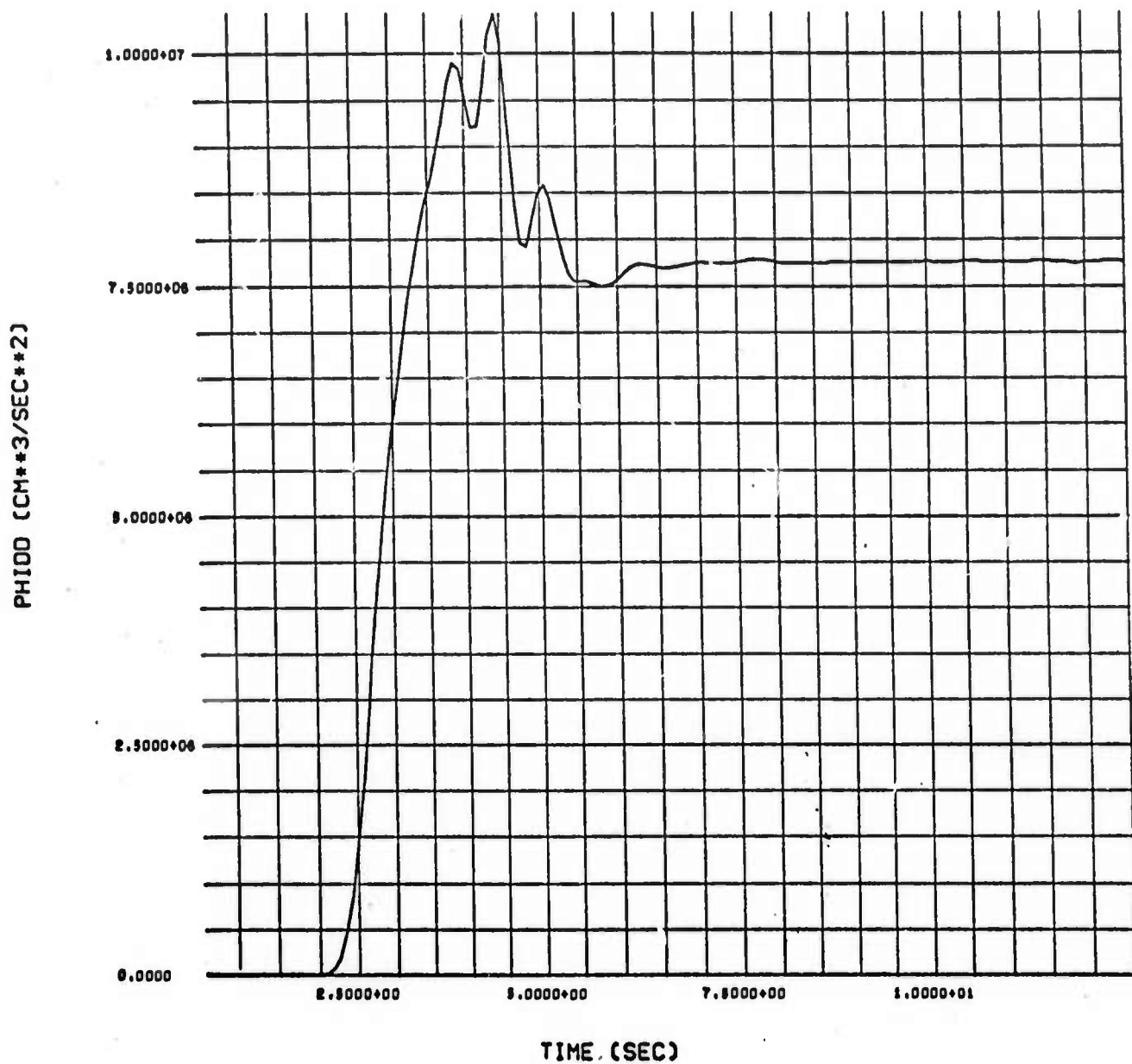


Fig. 20--Time history of scalar potential ($\ddot{\phi}$) at Station 2, SC.

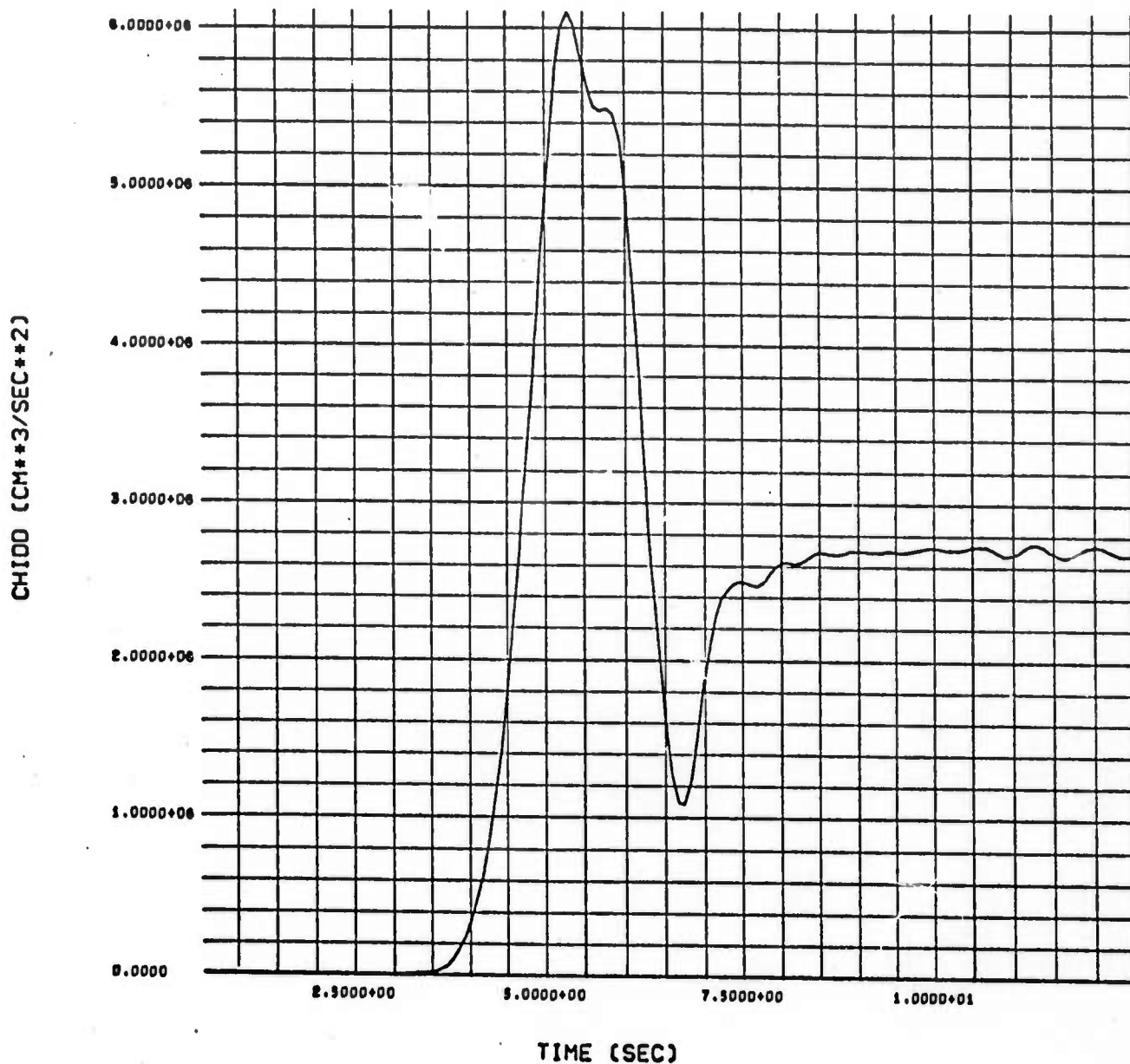


Fig. 21--Time history of vector potential ($\ddot{\chi}$) at Station 2, 5C.

3.3 PEAK PARTICLE VELOCITY

Peak particle velocity was determined at all stations 10 km from the center of the fault. Figure 22 shows peak particle velocity plotted versus the product of rupture velocity (V_R) and dynamic stress drop ($\tau_0 - \tau_k$). The functional relation seems to be linear, with the slope varying with azimuth as shown. Fault length does not seem to be important in determining peak velocity.

Figures 23 through 42 show the velocity seismograms for the four calculations at Stations 1 through 5. The complexity of the seismogram increases with increasing azimuth, apparently due to the temporal separation of the starting and stopping phases of the propagating rupture.

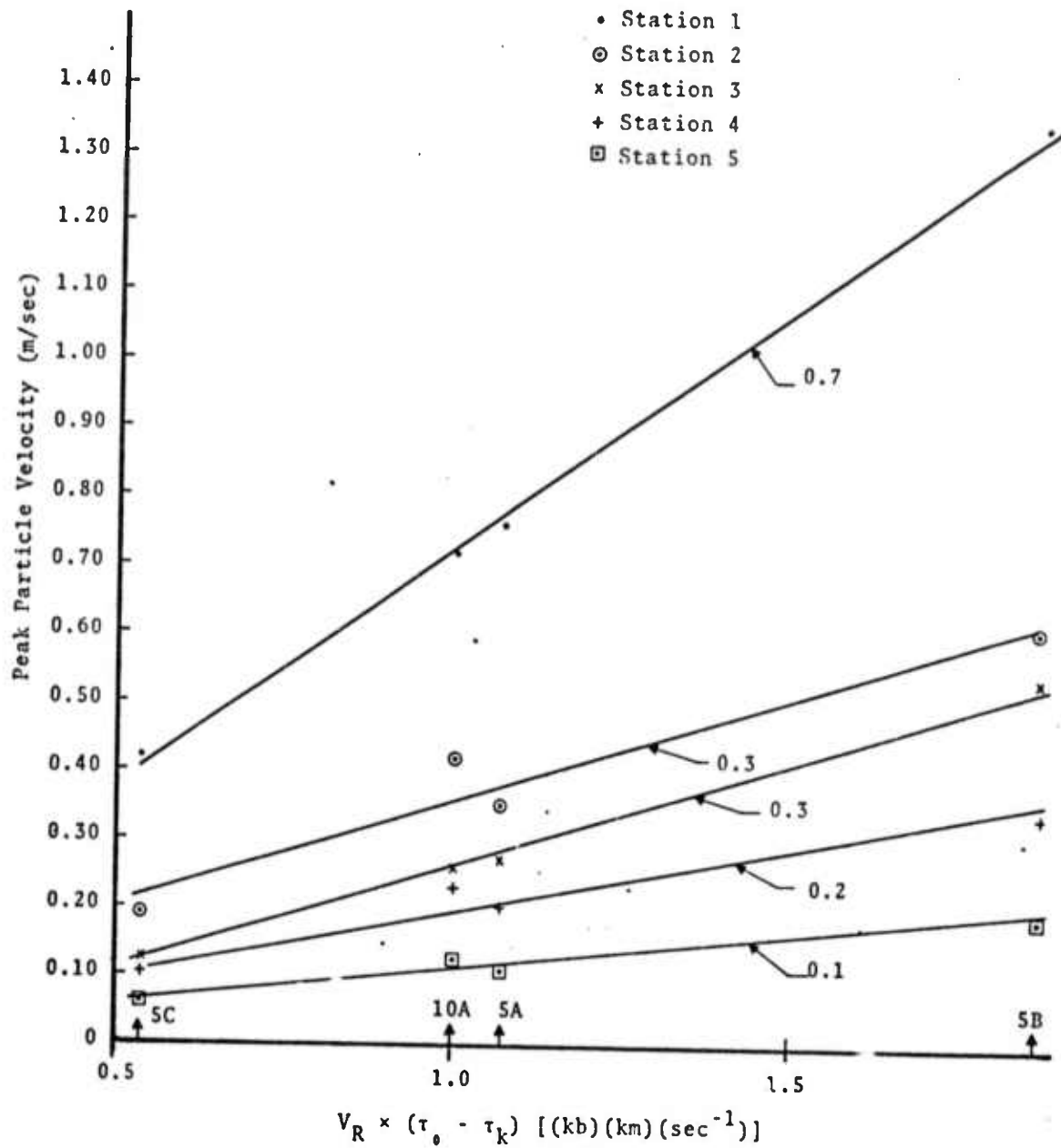


Fig. 22--Peak particle velocity at a radius 10 km from the center of the fault versus the product of rupture velocity (V_R) and dynamic stress drop ($(\tau_0 - \tau_k)$).

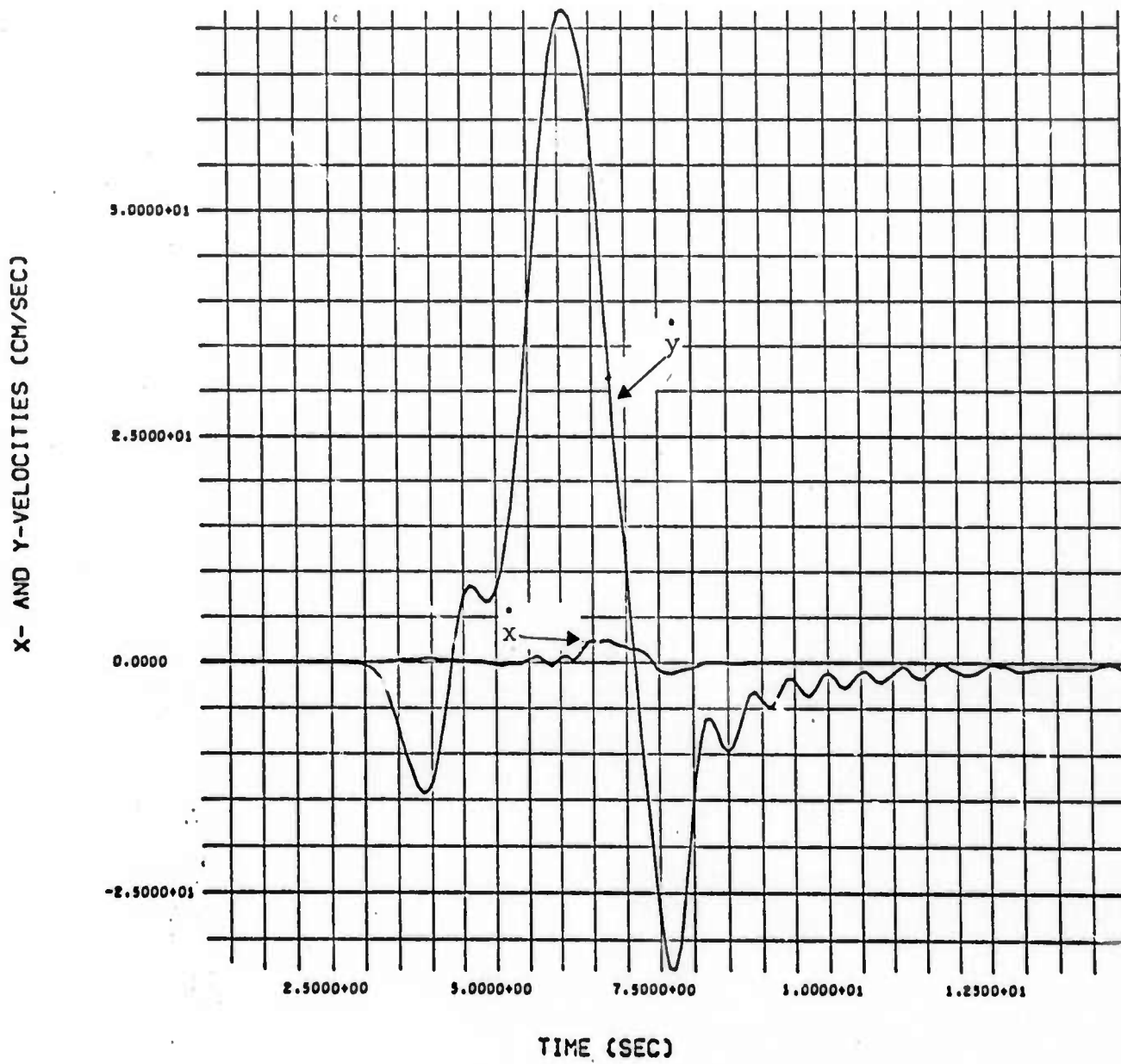


Fig. 23--Particle velocity at Station 1, 10A.

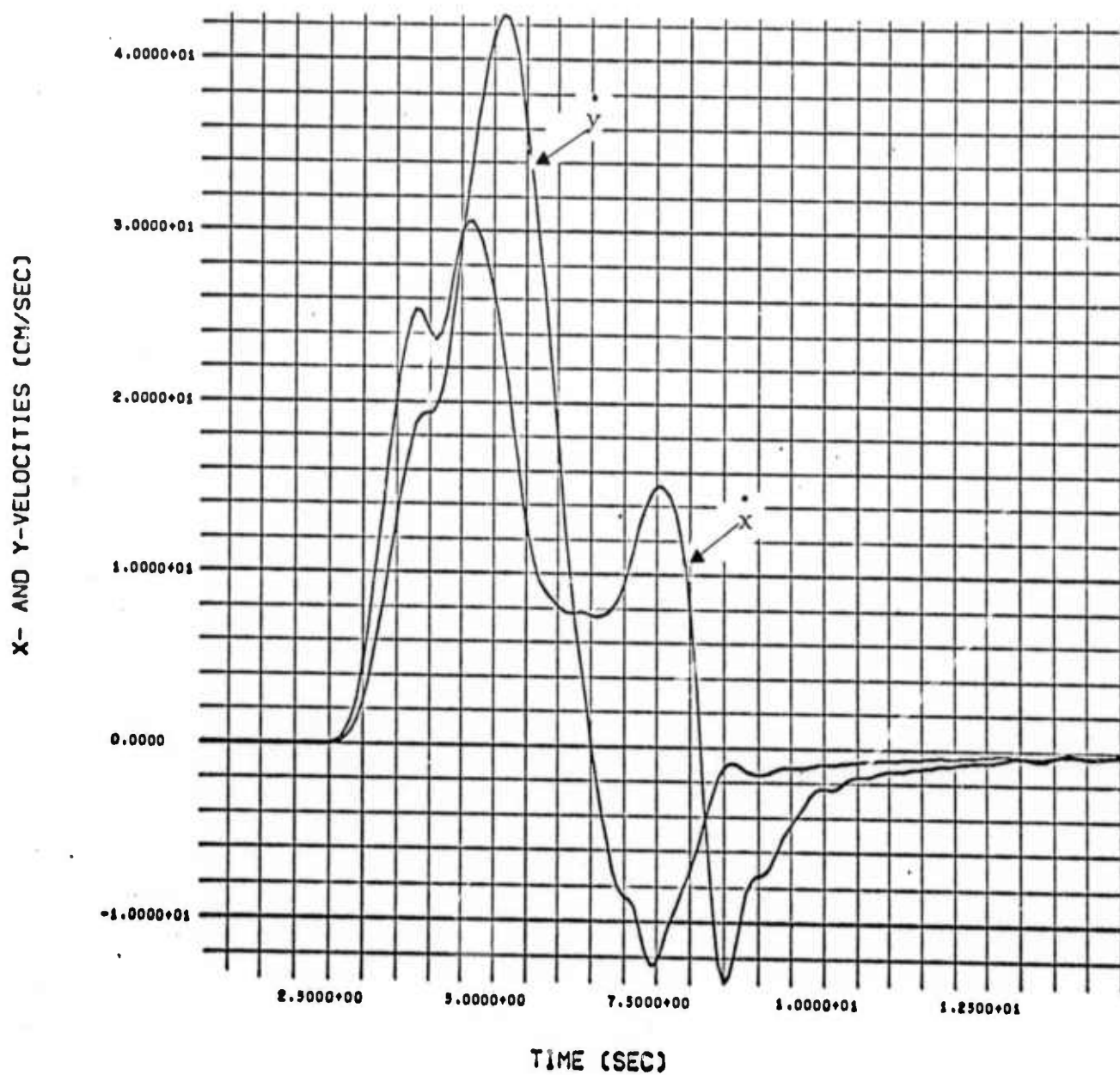


Fig. 24--Particle velocity at Station 2, 10A.

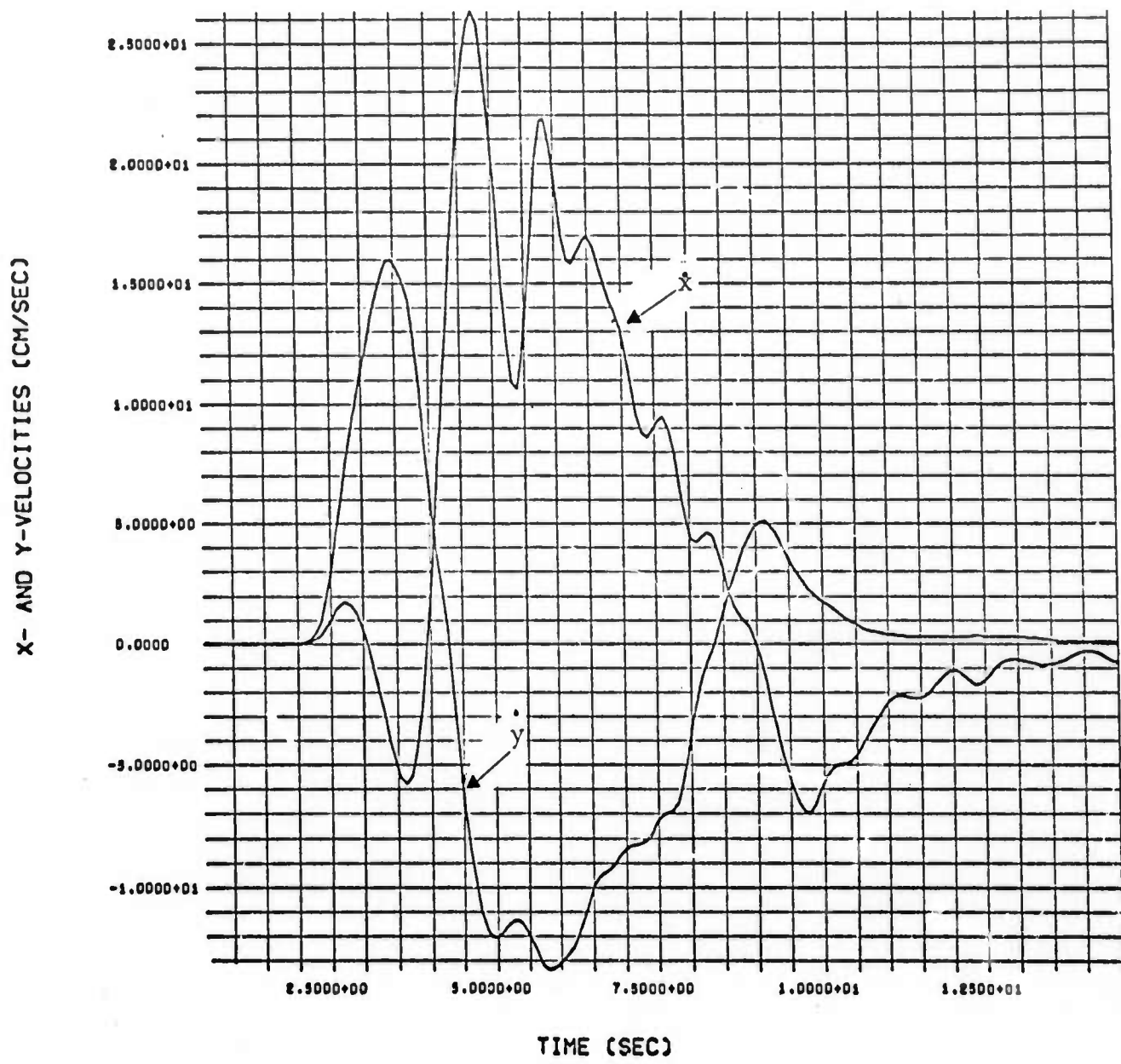


Fig. 25--Particle velocity at Station 3, 10A.

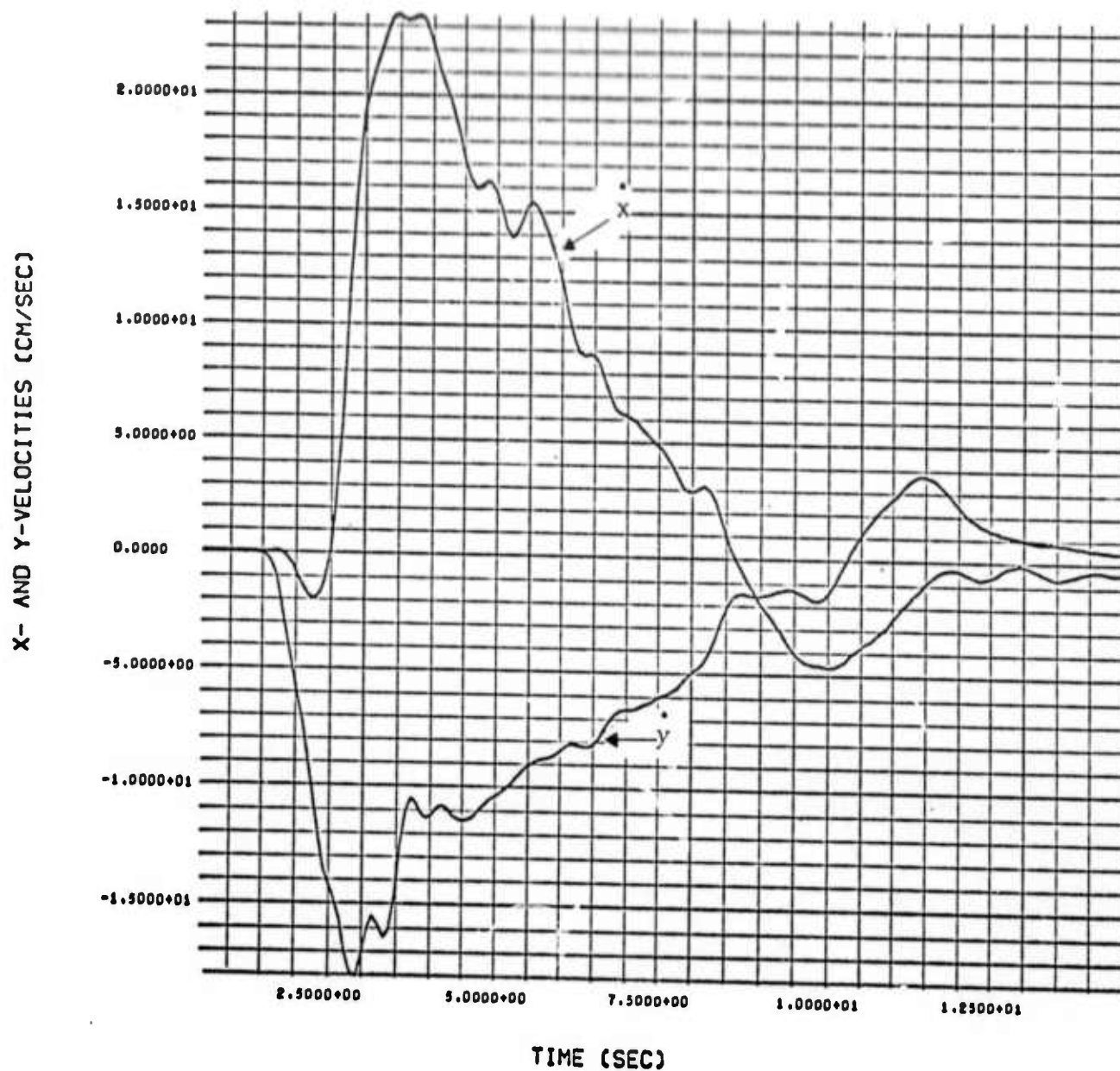


Fig. 26--Particle velocity at Station 4, 10A.

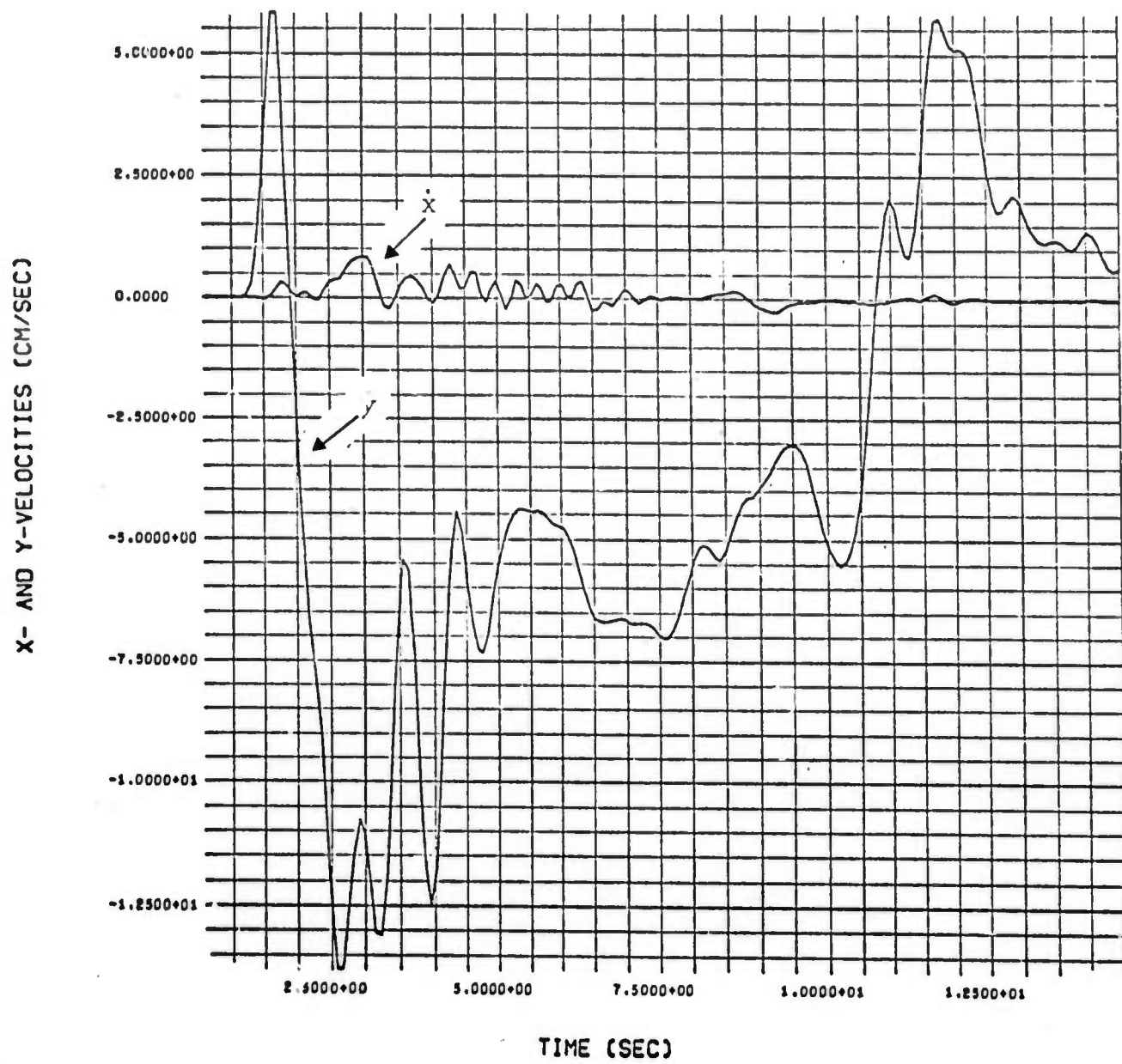


Fig. 27--Particle velocity at Station 5, 10A.

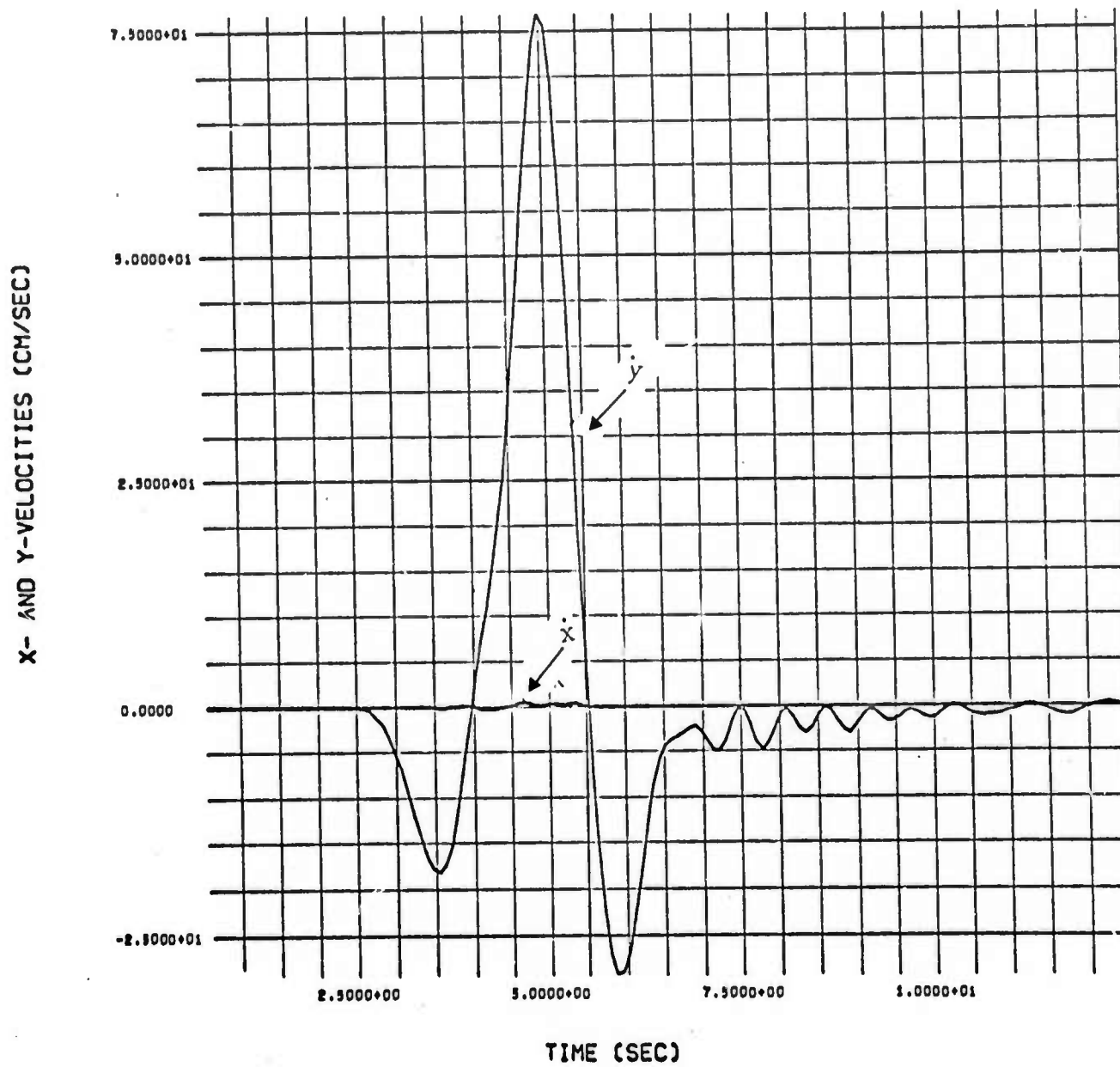


Fig. 28--Particle velocity at Station 1, 5A.

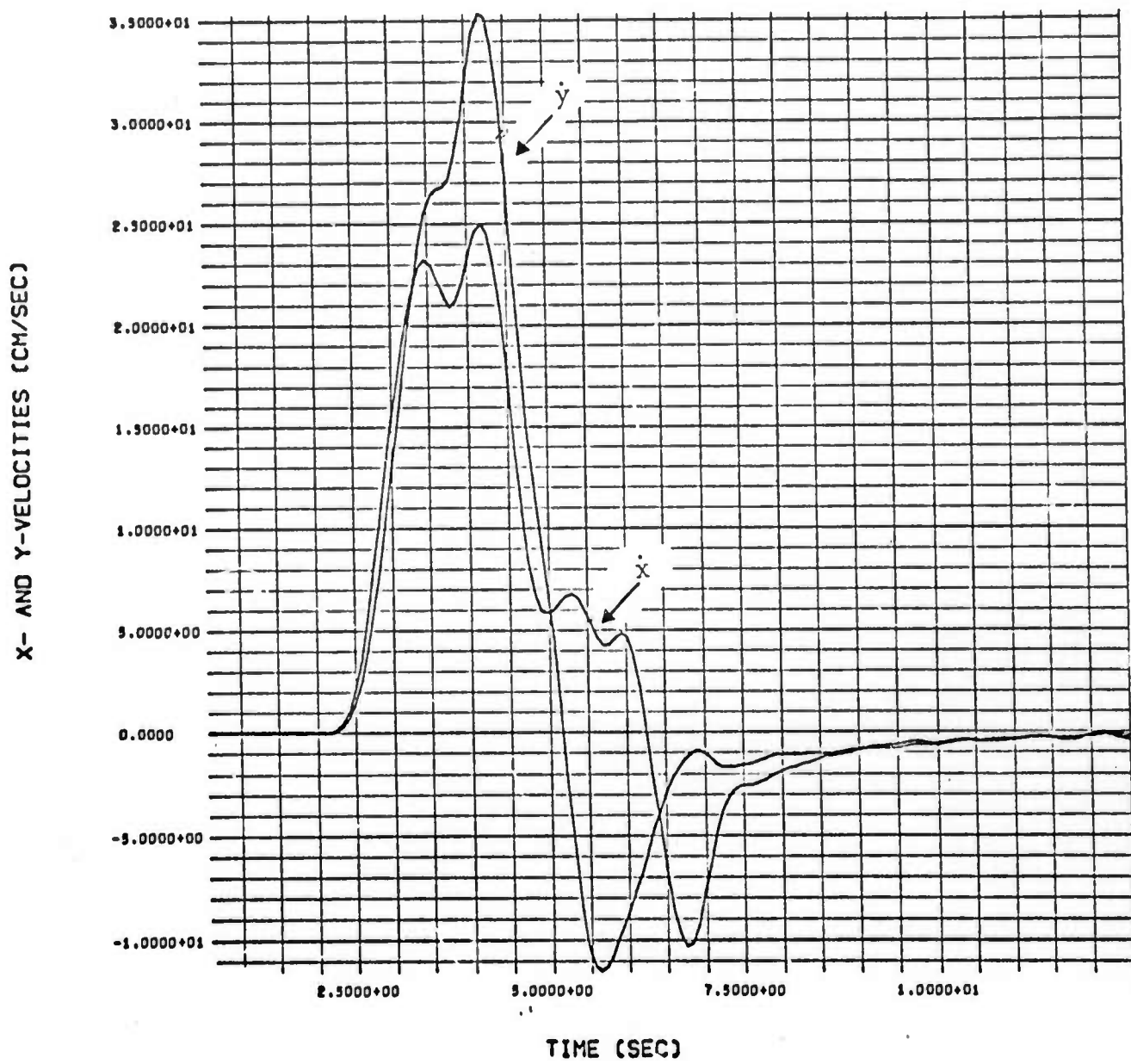


Fig. 29--Particle velocity at Station 2, 5A.

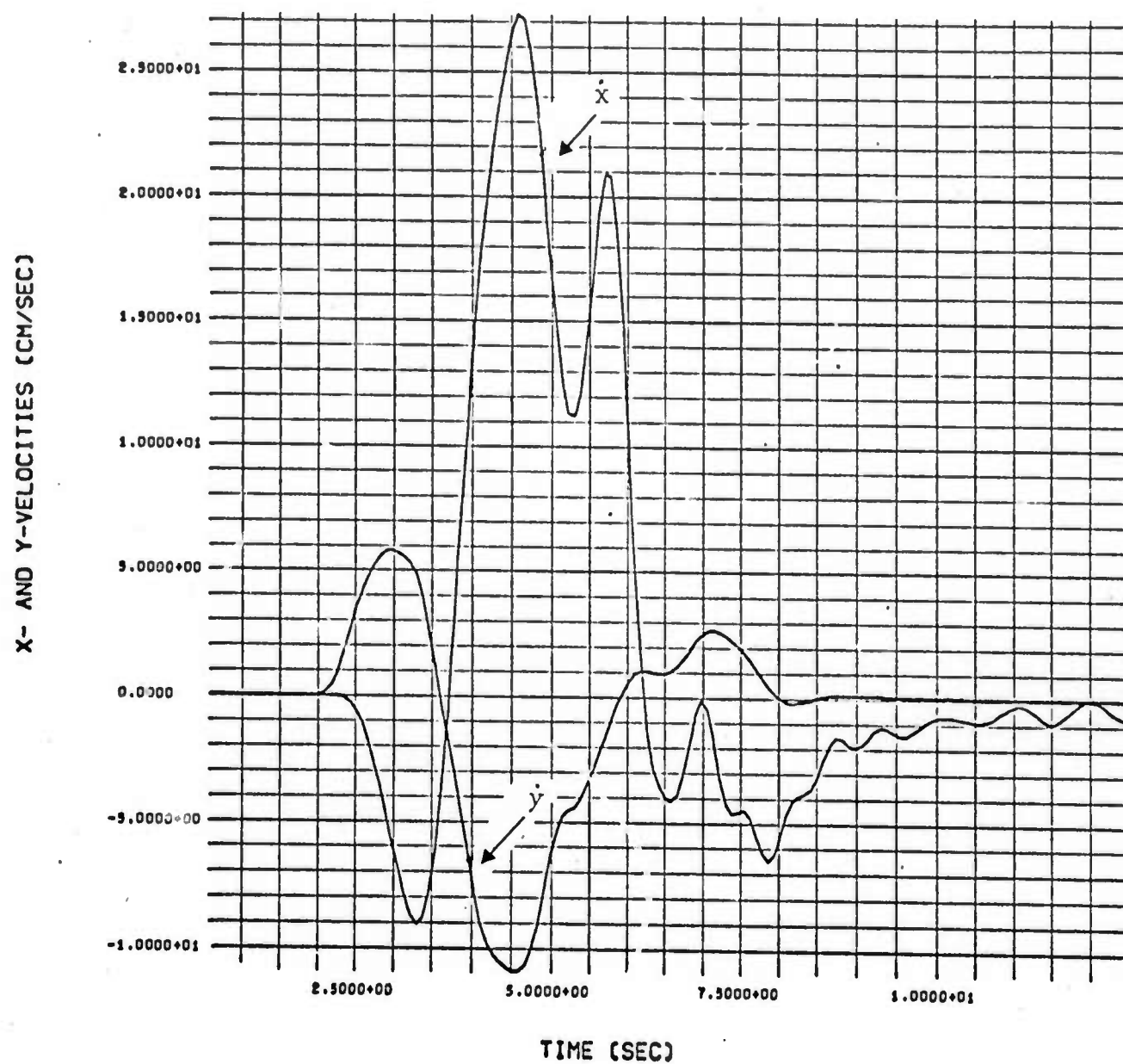


Fig. 30--Particle velocity at Station 3, 5A.

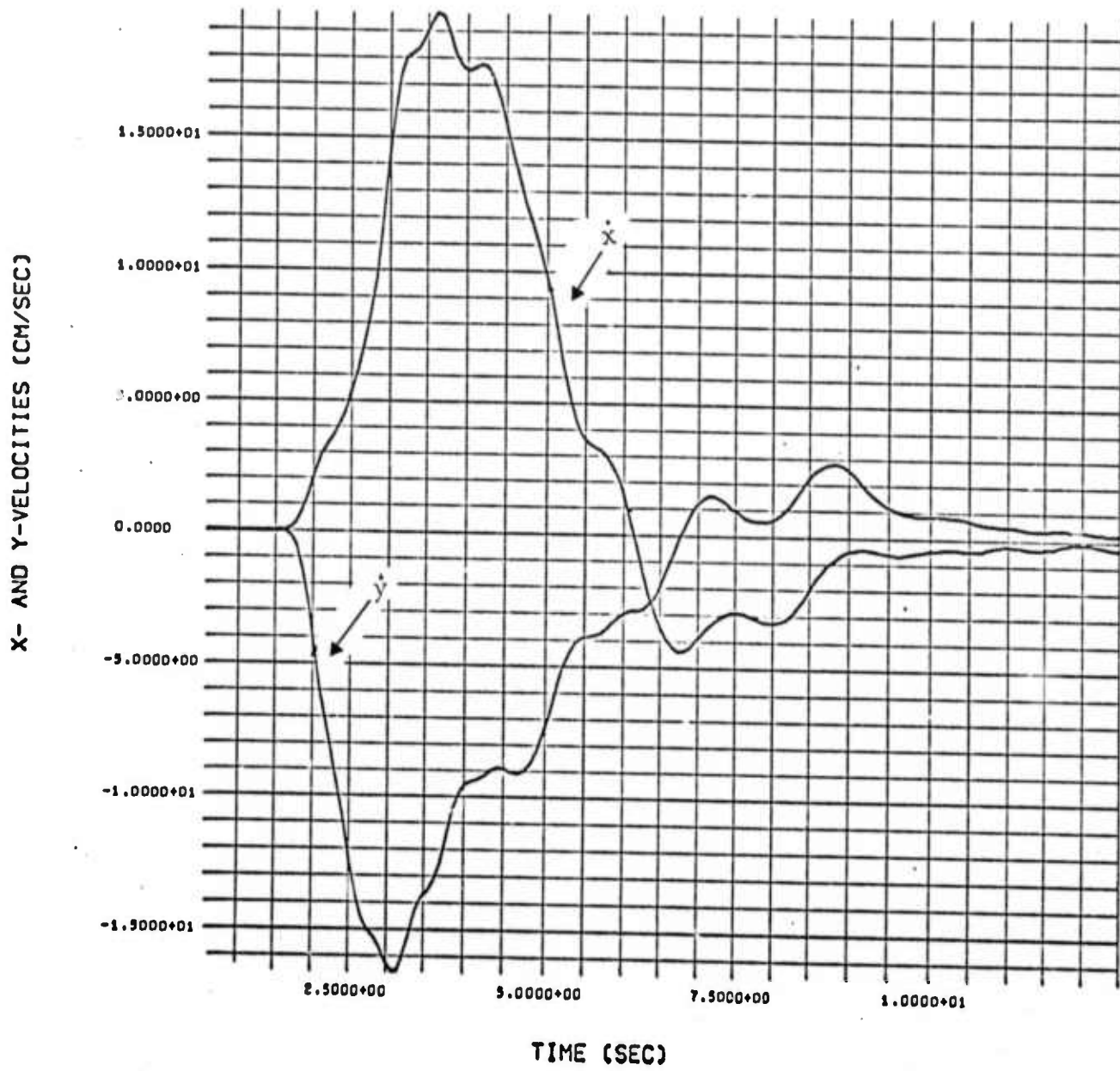


Fig. 31--Particle velocity at Station 4, 5A.

X- AND Y-VELOCITIES (CM/SEC)

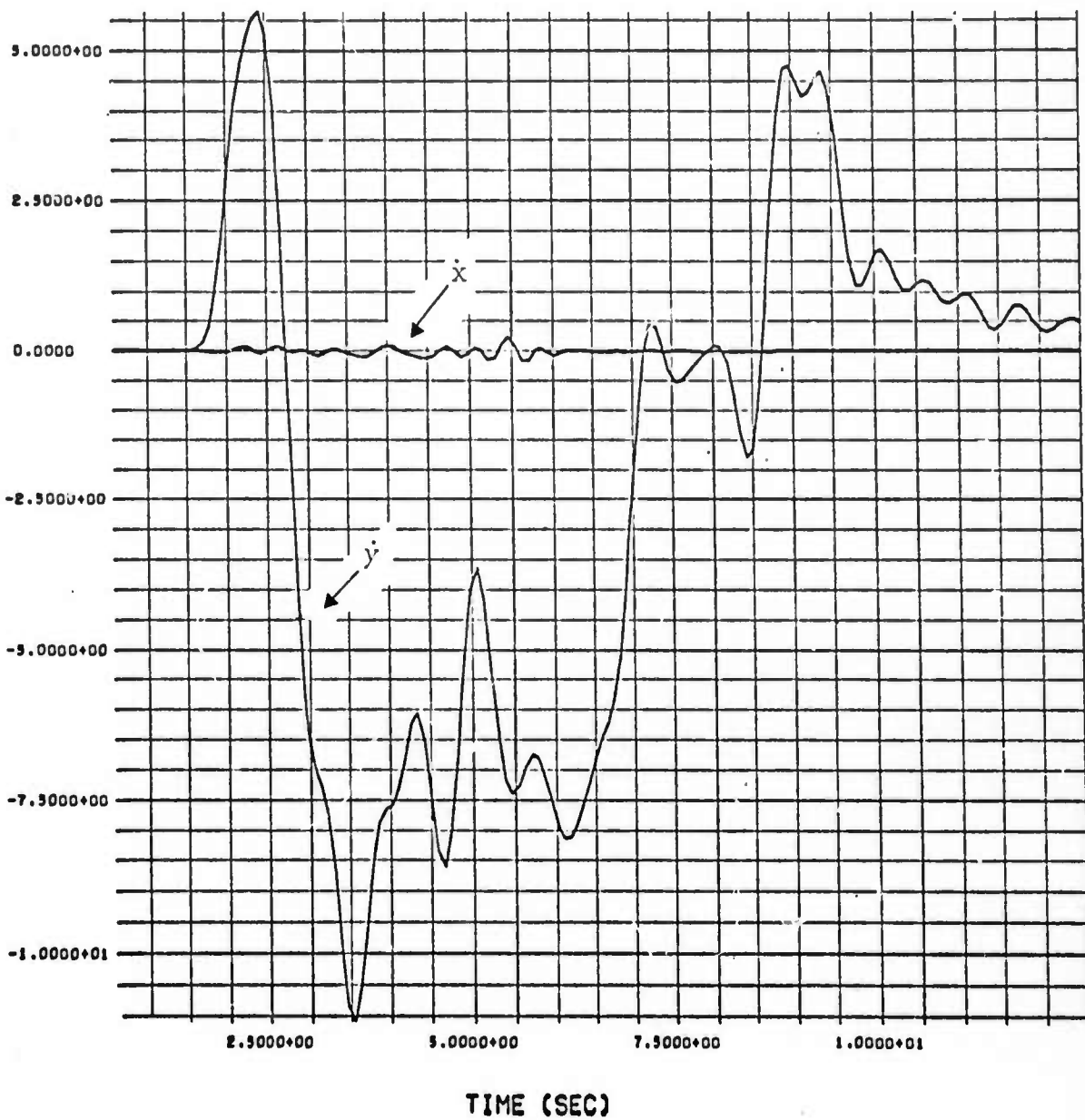


Fig. 32--Particle velocity at Station 5, 5A.

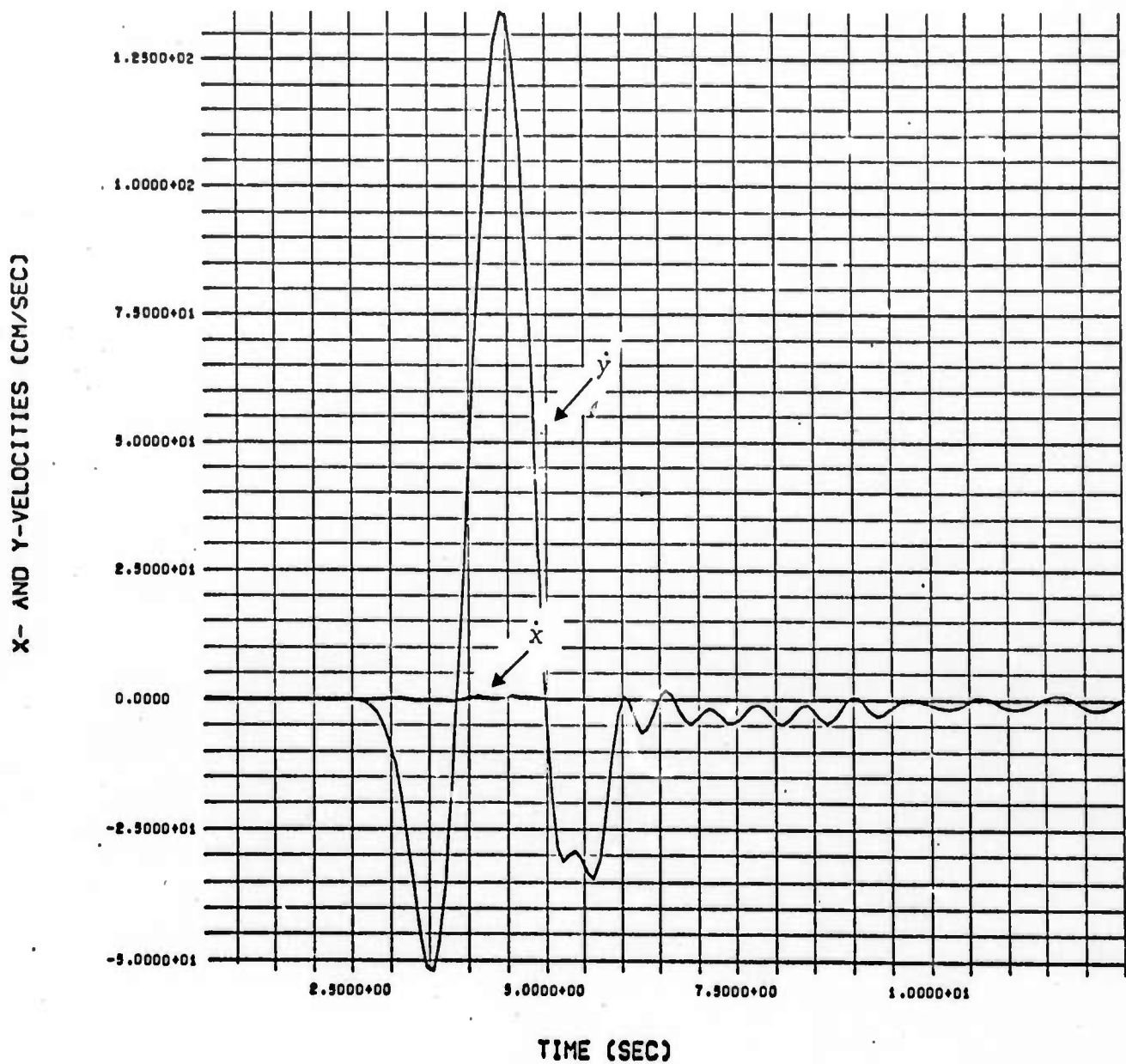


Fig. 33--Particle velocity at Station 1, 5B.

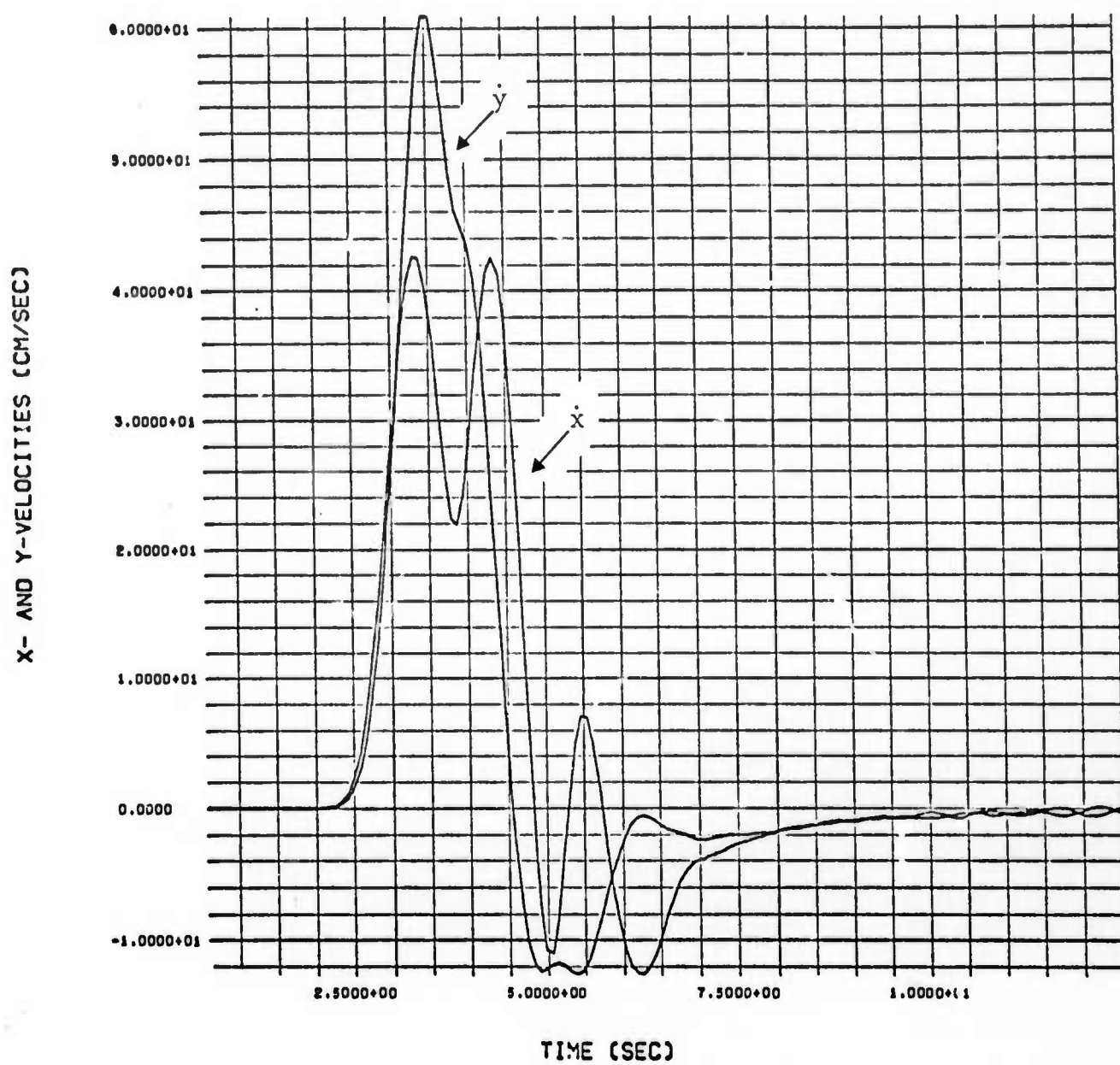


Fig. 34--Particle velocity at Station 2, 5B.

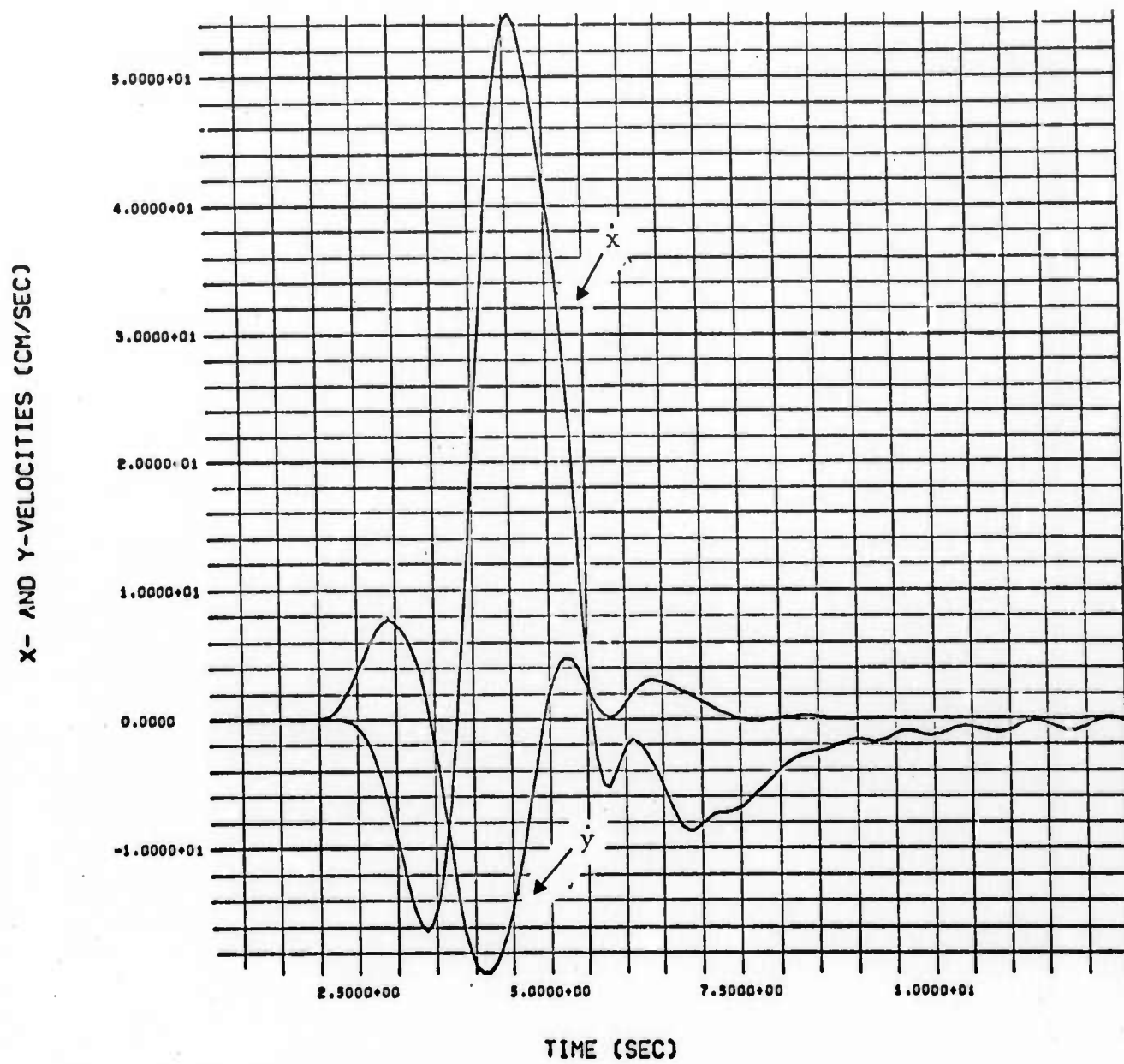


Fig. 35--Particle velocity at Station 3, 5B.

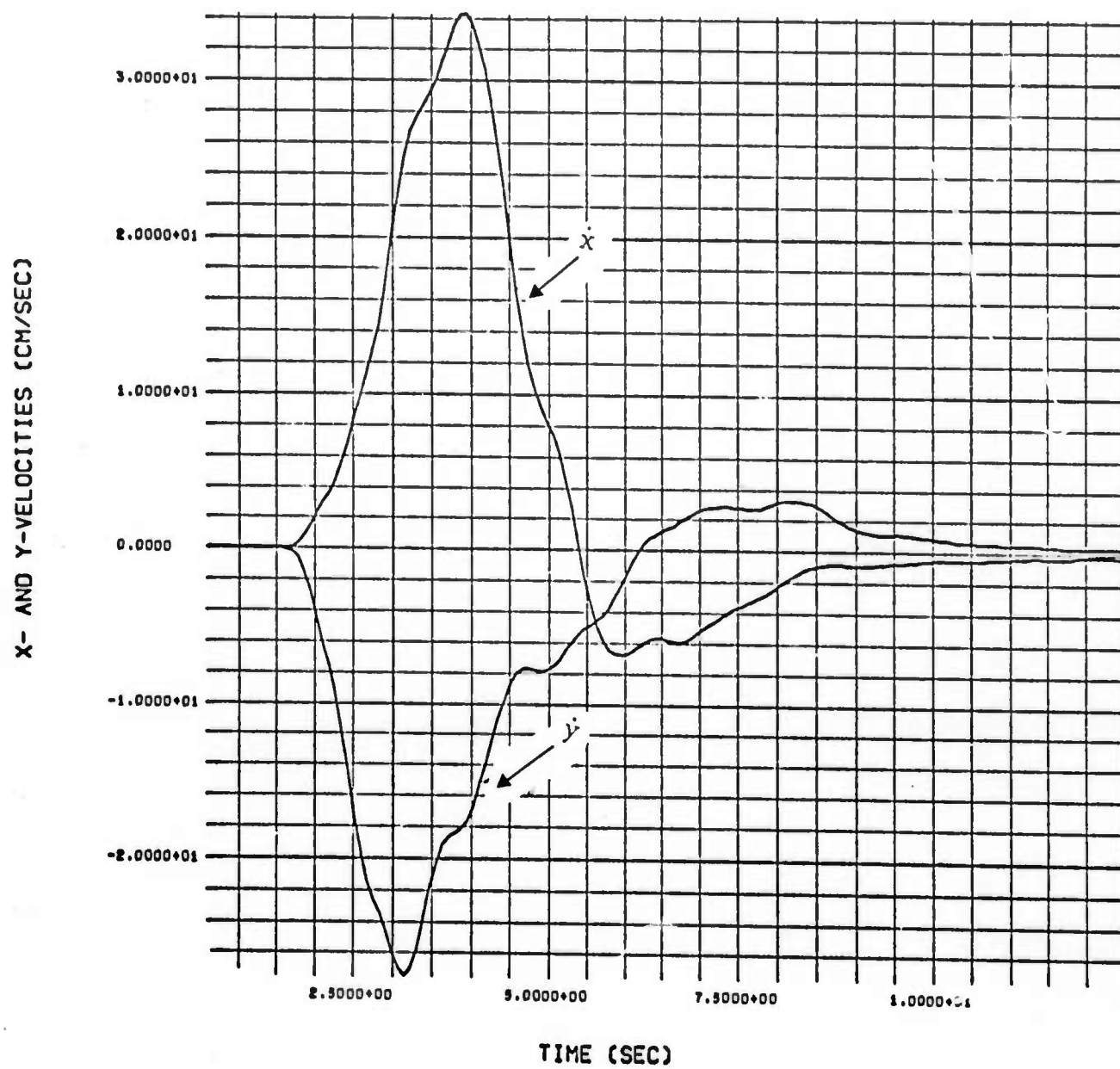


Fig. 36--Particle velocity at Station 4, 5B.

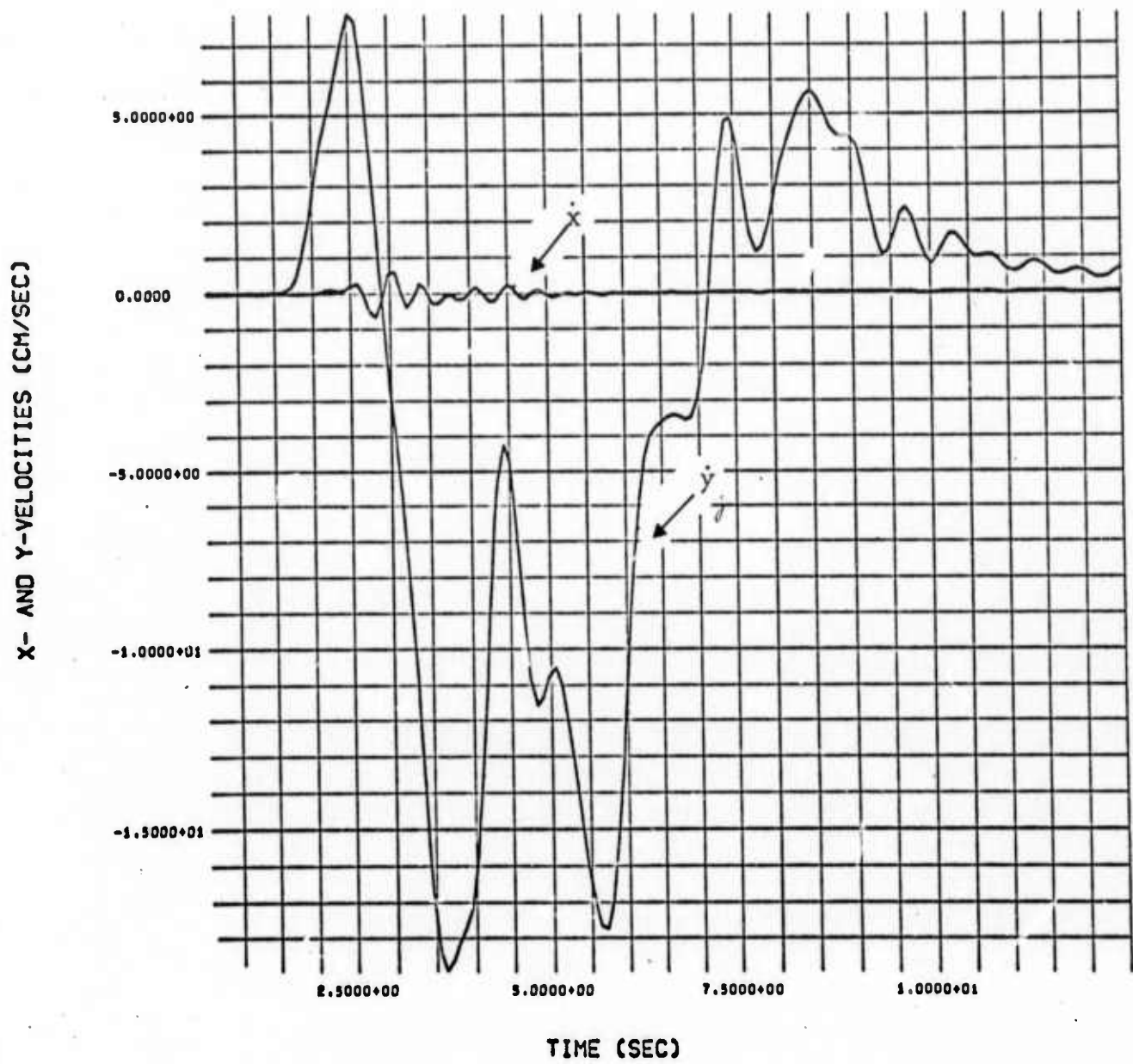


Fig. 37--Particle velocity at Station 5, 5B.

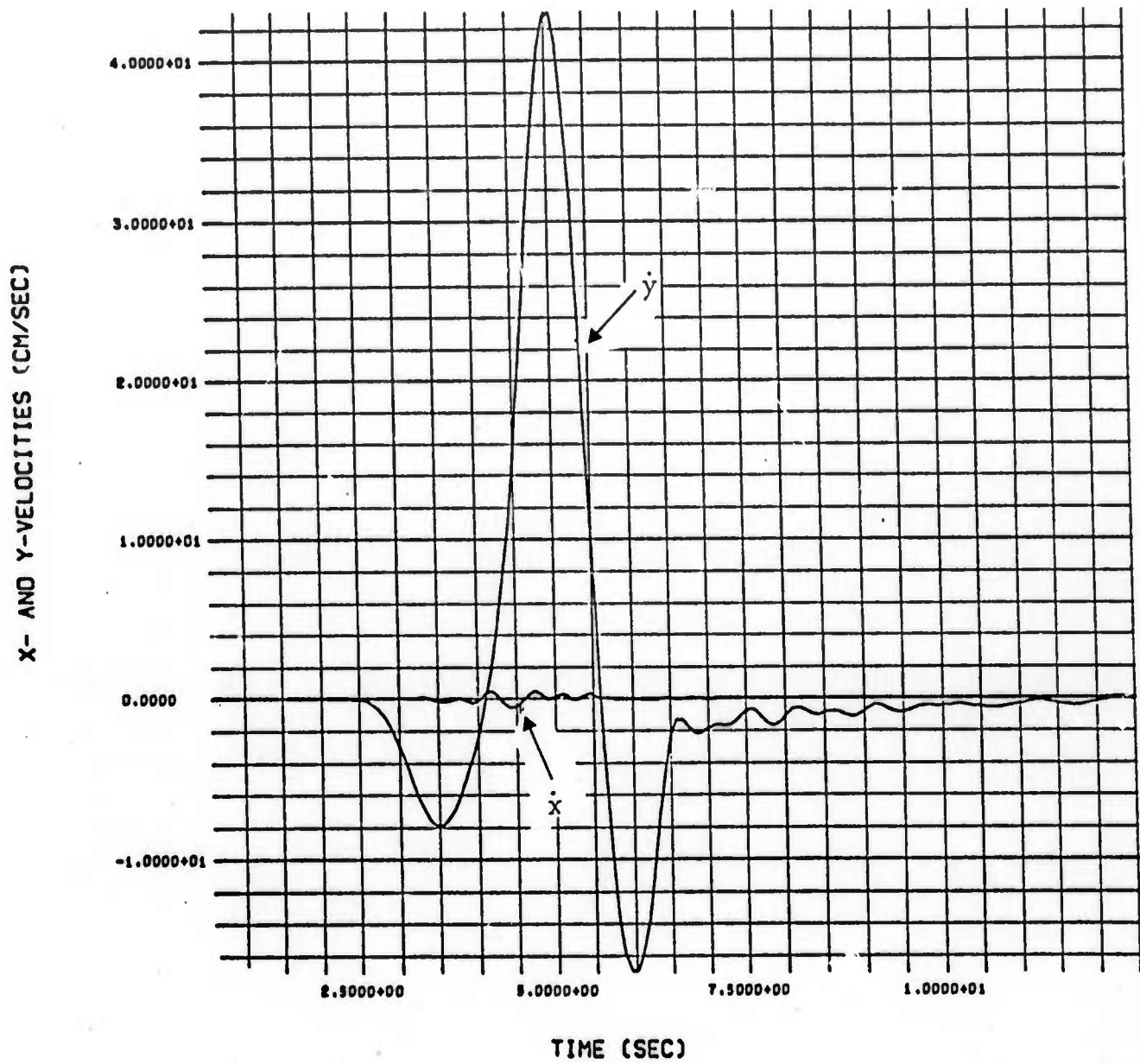


Fig. 38--Particle velocity at Station 1, 5C.

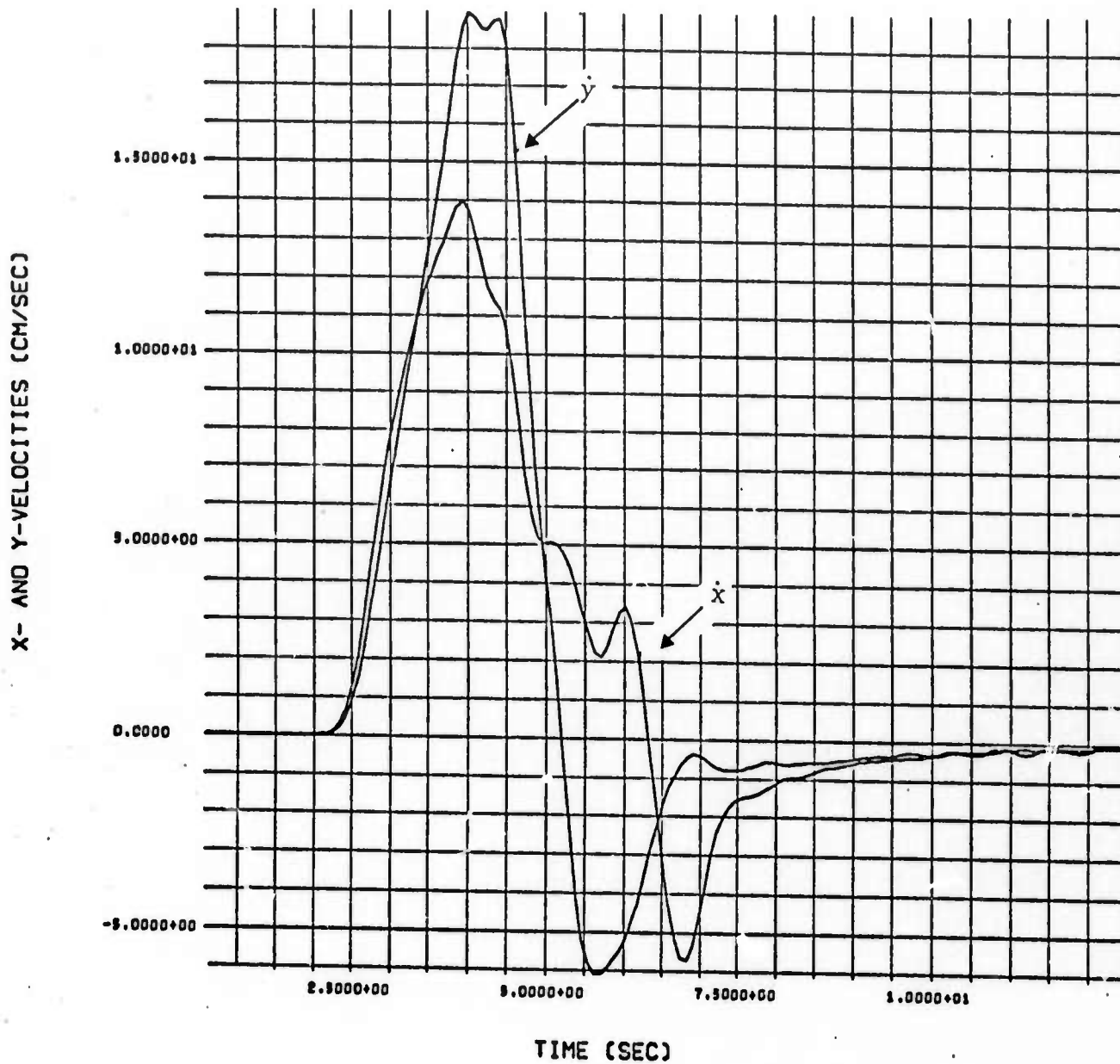


Fig. 39--Particle velocity at Station 2, SC.

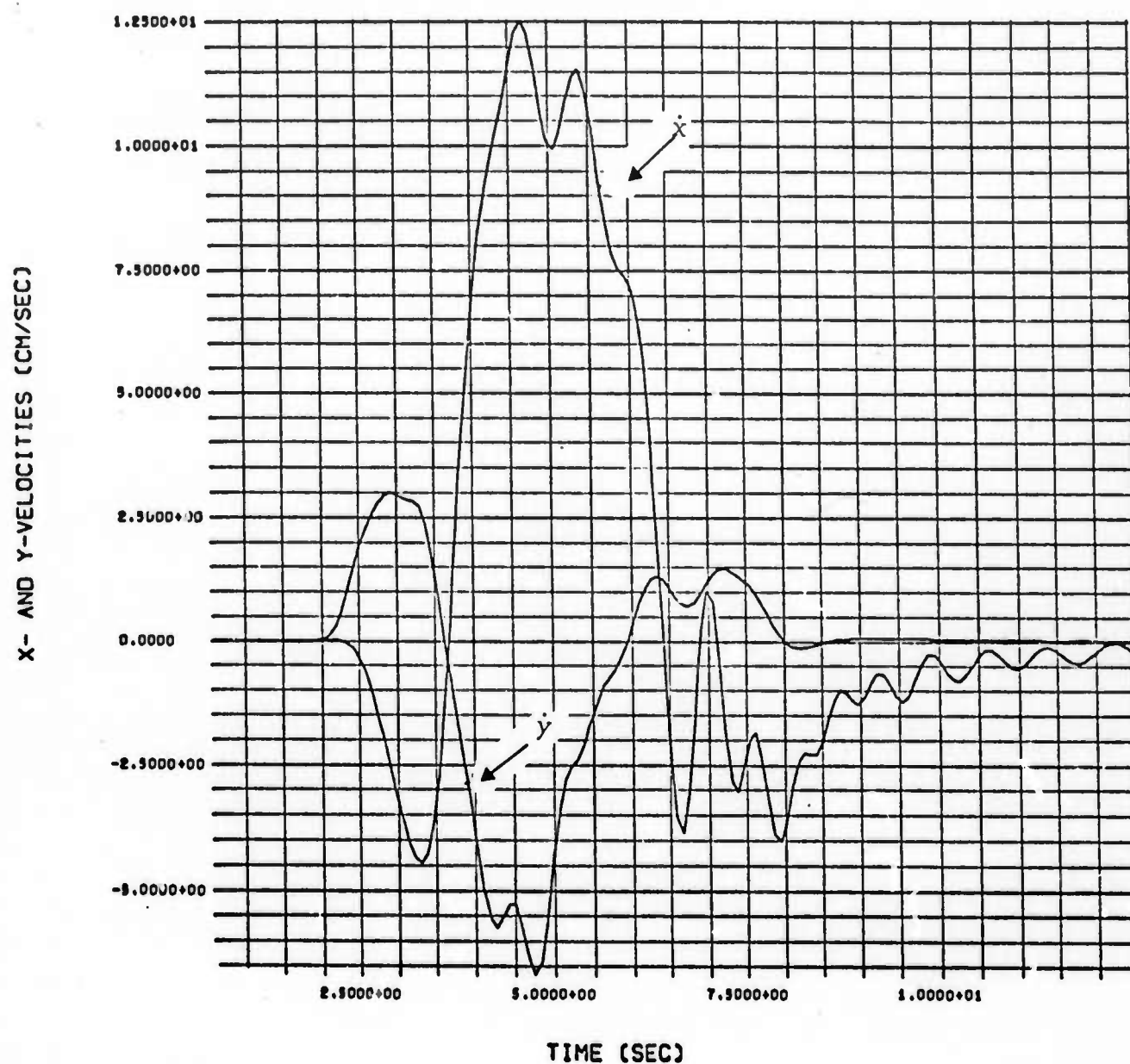


Fig. 40--Particle velocity at Station 3, 5C.

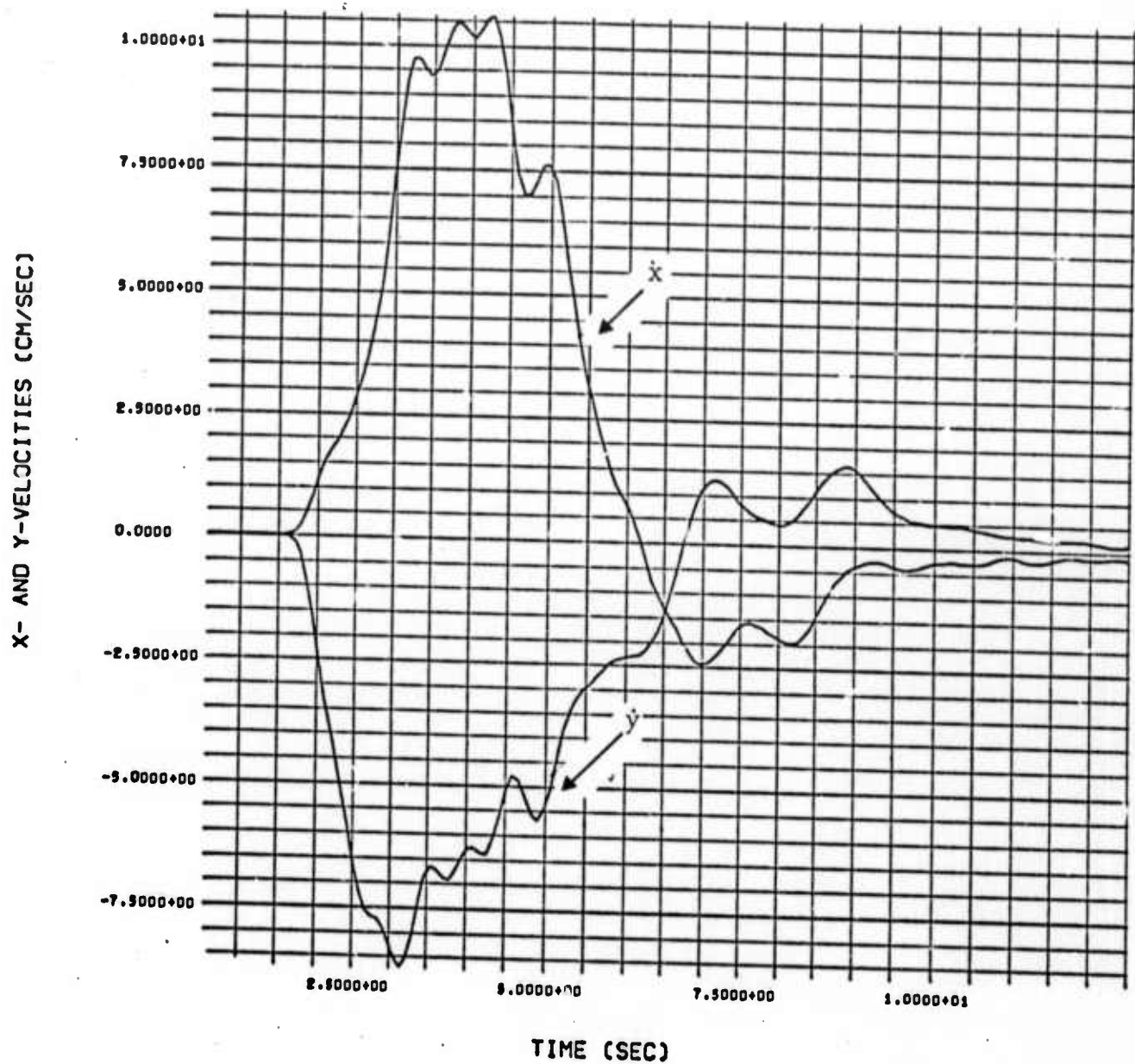


Fig. 41--Particle velocity at Station 4, 5C.

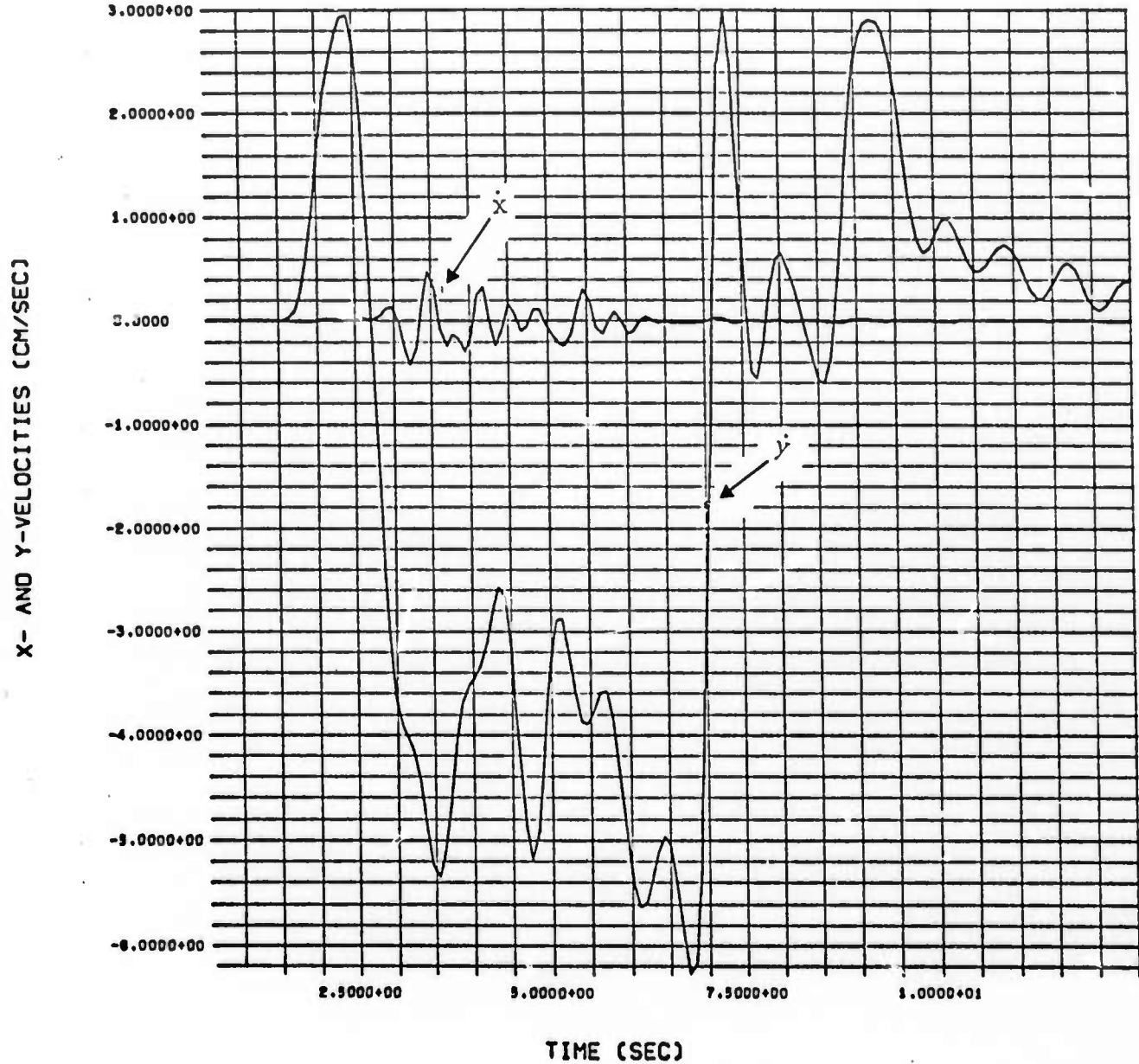


Fig. 42--Particle velocity at Station 5, SC.

3.4 DISPLACEMENT SPECTRA AND CORNER FREQUENCY

A sketch of a typical near field displacement spectrum is shown in Fig. 43. At low frequencies the spectrum shows an f^{-1} trend, caused by the static displacement. At high frequencies the spectrum decays approximately as f^{-3} , indicating that the equivalent elastic source should be continuous in both displacement and particle velocity.

As shown in Fig. 43, the corner frequency is defined to occur at the transition to the high frequency (f^{-3}) trend. Figure 44 shows corner frequency plotted versus V_R/L for the indicated stations at a radius of 10 km from the center of the fault. Corner frequency seems to be linearly related to the V_R/L ratio, with the slope varying with azimuth as shown. Apparently, corner frequency is independent of dynamic stress drop.

Figure 45 through 48 show the x and y components of displacement spectra at Station 2. The corner frequencies are marked in each figure. A less ambiguous determination of the corner frequency should be possible when the near and far field source components are separated.

Finally, there is some indication from the spectra shown in Figs. 45 through 48 that the value of the spectrum at the corner frequency is proportional to the product of the fault length (L) and the dynamic stress drop ($\tau_0 - \tau_k$).

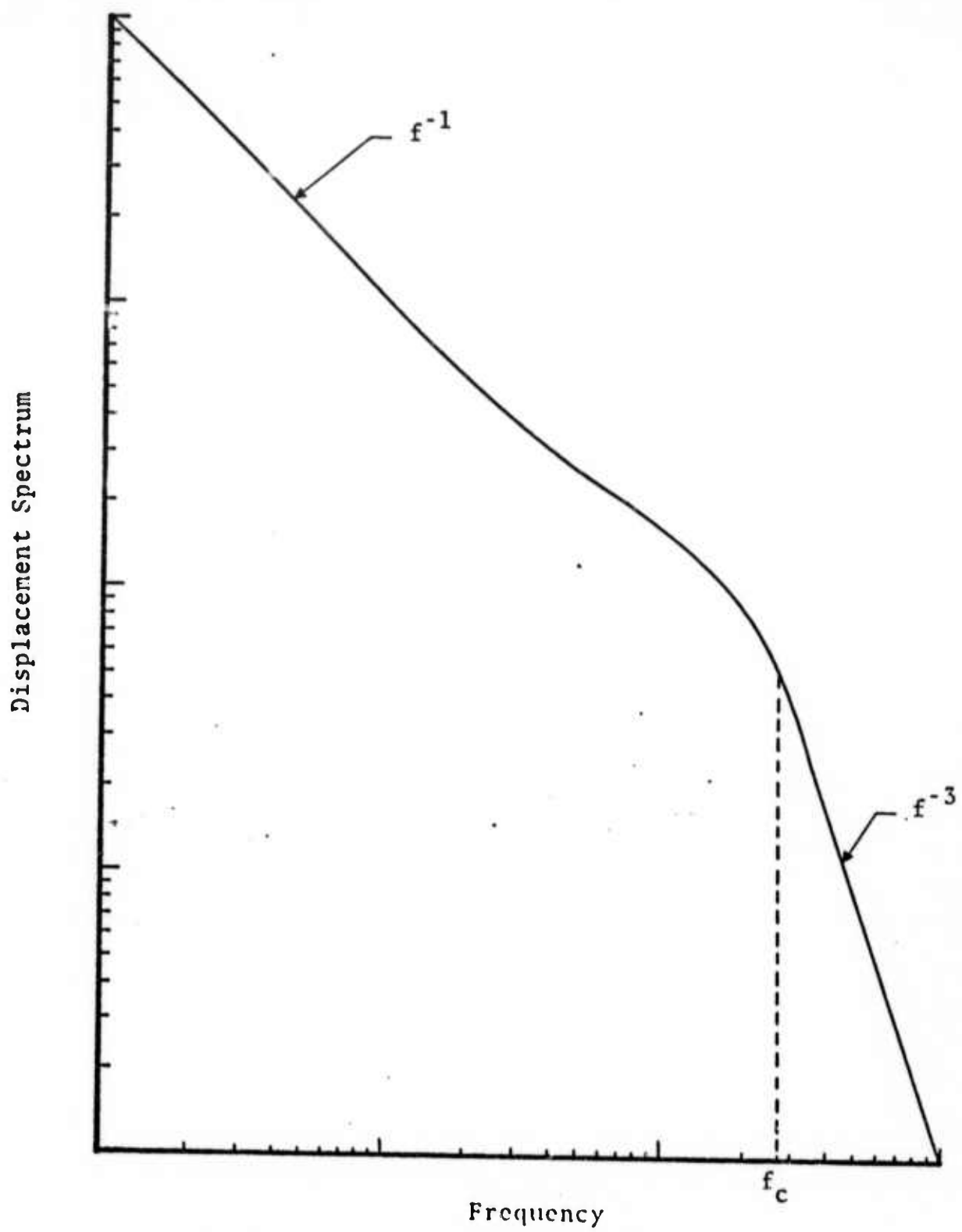


Fig. 43--Sketch of typical near field displacement spectrum showing f^{-1} trend at low frequencies, f^{-3} trend at high frequencies and definition of corner frequency (f_c).

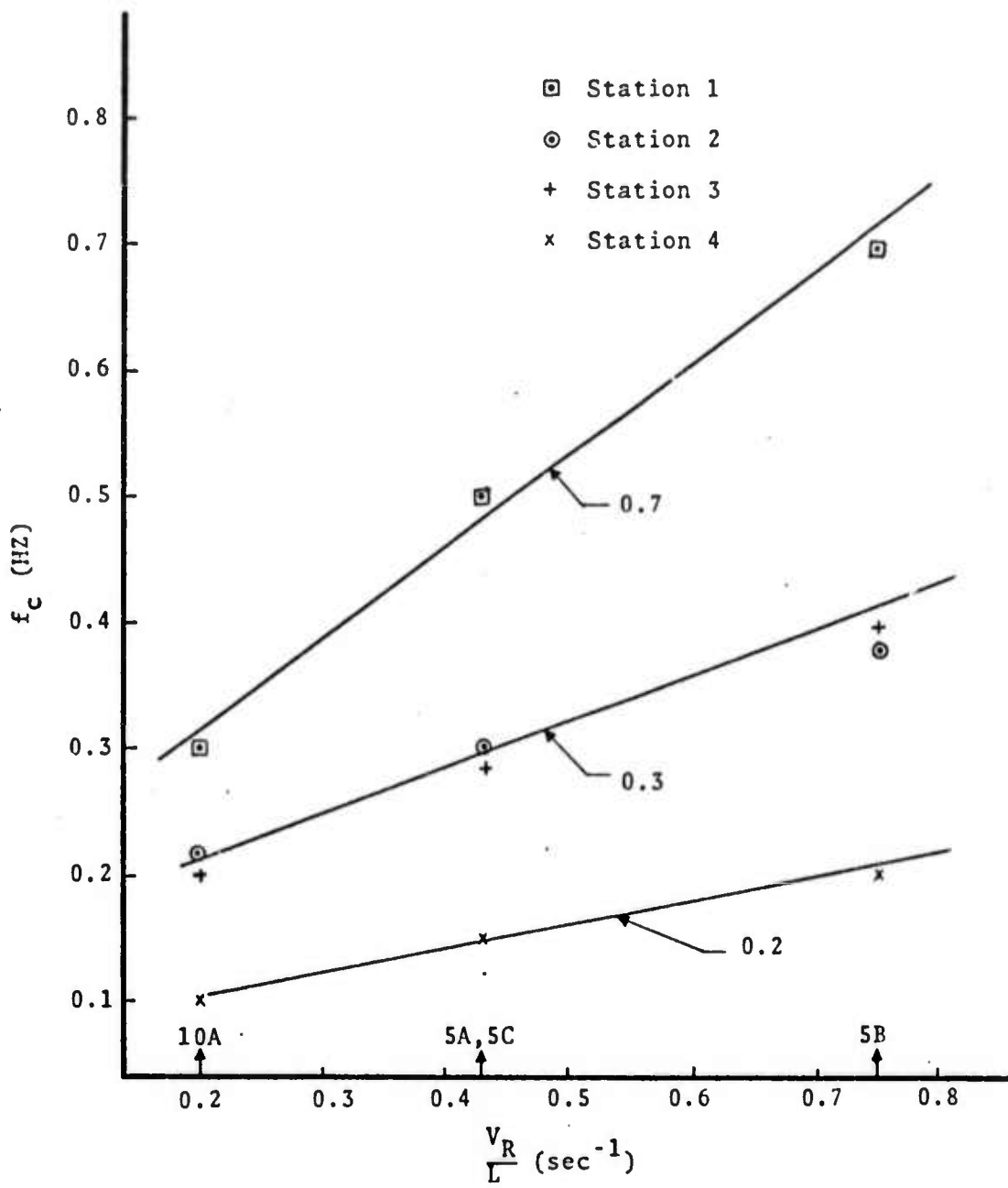


Fig. 44--Corner frequency versus the ratio of rupture velocity and fault length at a radius of 10 km from the center of the fault.

ABS TRANSFORMS - DX AND DY (cm-sec)

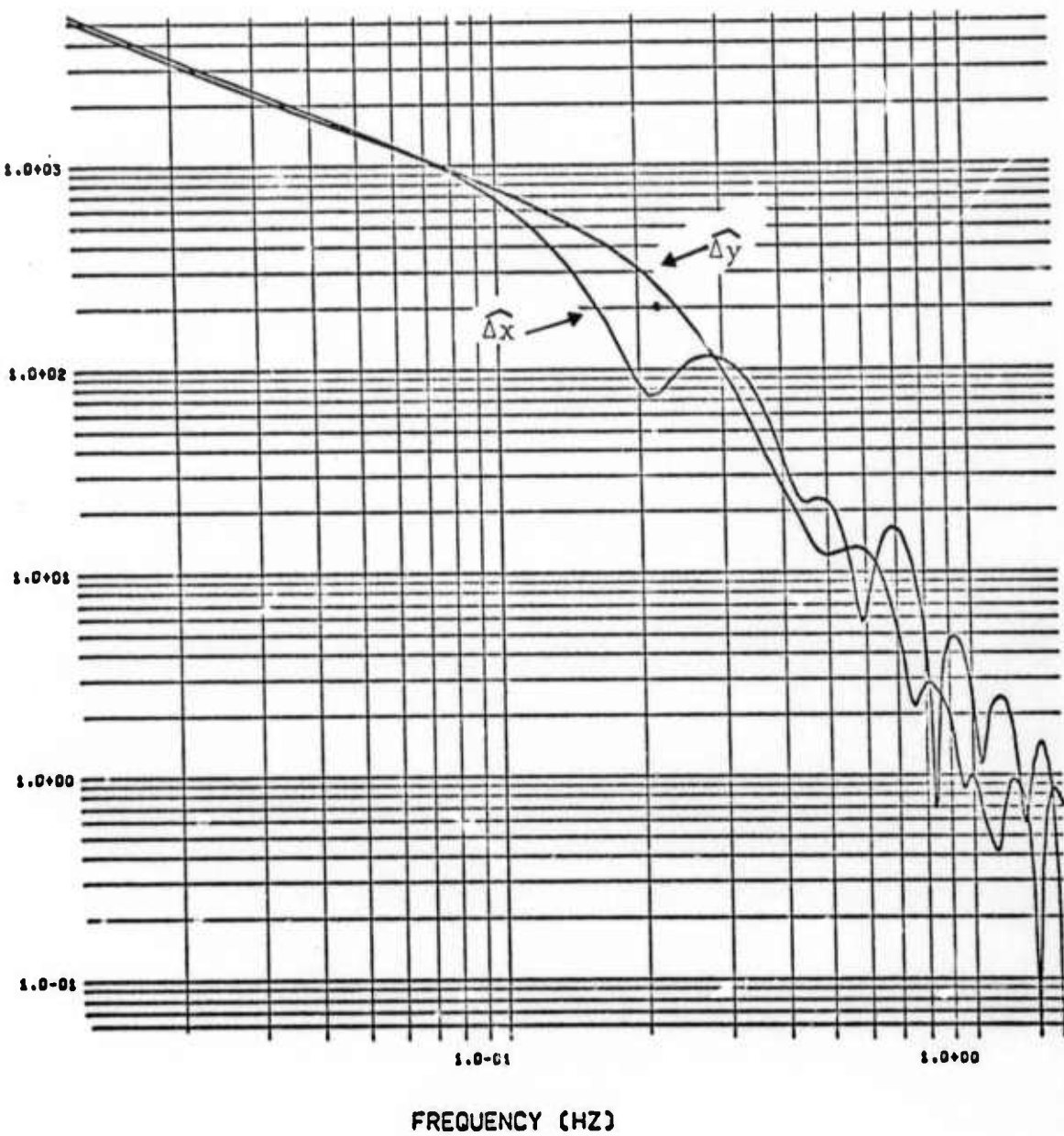


Fig. 45--Displacement spectra at Station 2, 10A.

ABS TRANSFORMS - DX AND DY (cm-sec)

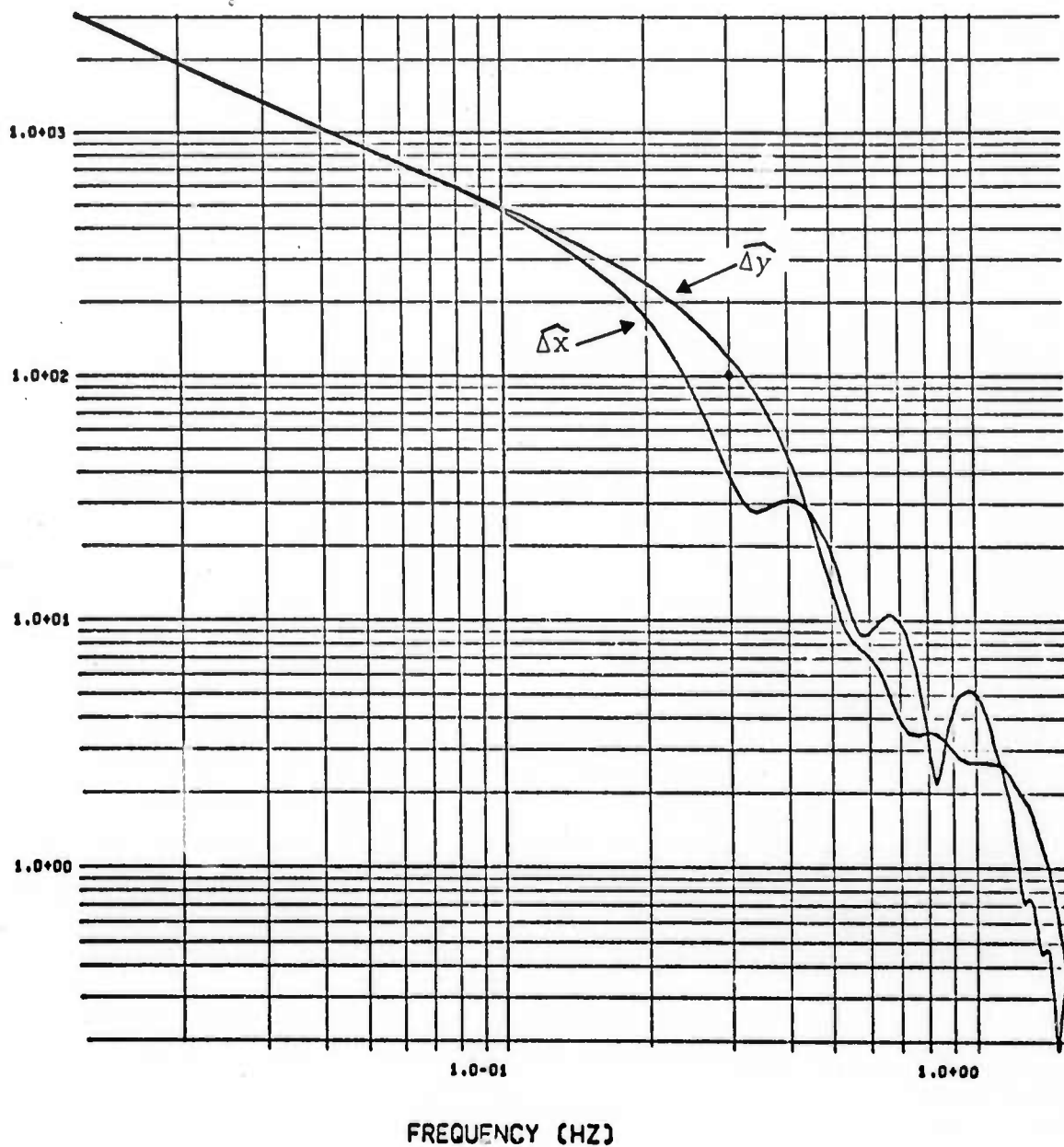


Fig. 46--Displacement spectra at Station 2, 5A.

ABS TRANSFORMS - DX AND DY (cm-sec)

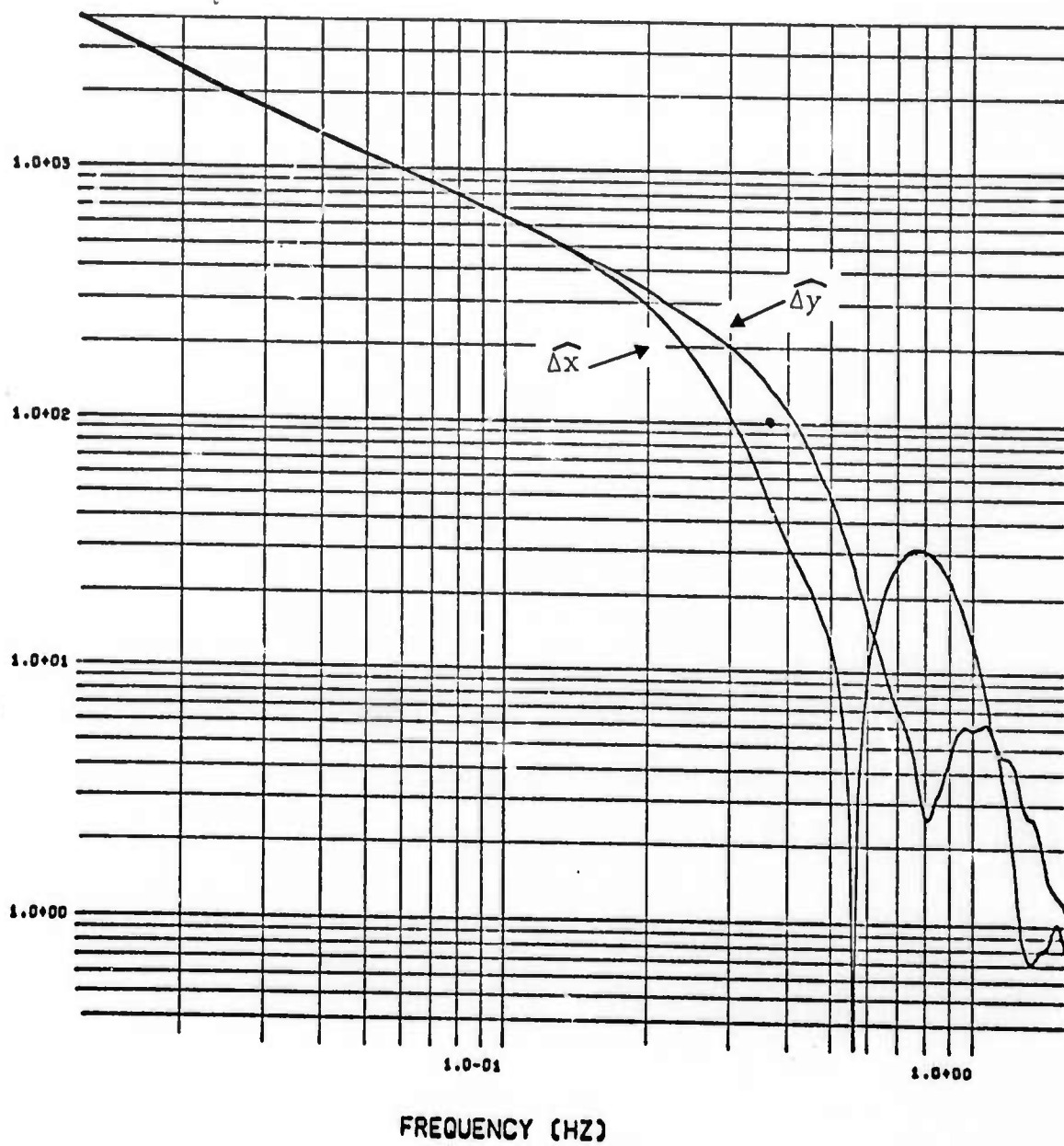


Fig. 47--Displacement spectra at Station 2, 5B.

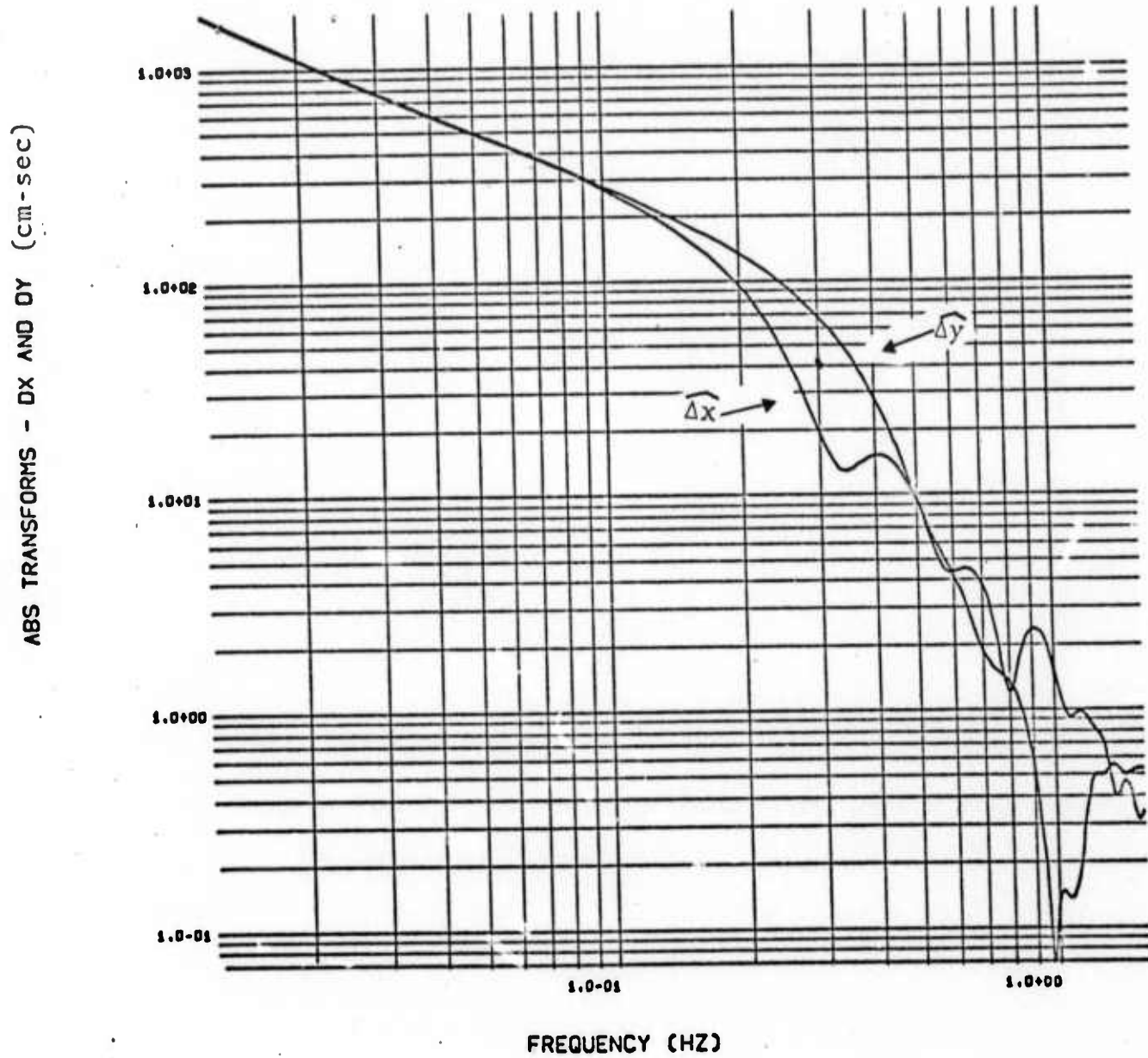


Fig. 48--Displacement spectra at Station 2, 5C.

IV. SUMMARY

A stick-slip rupture model has been incorporated into a two-dimensional Lagrangian code with the added feature that rupture initiation is plastic work dependent. Laboratory data, from appropriate rock mechanics tests, may be used to specify the parameters in the model.

Theoretical seismograms have been generated in both the frequency and time domain along with a decomposition of the ground motion into P and S components. Results from the four calculations, run to date, are as follows:

- A finite rupture velocity produces a noticeable Doppler effect in the radiation pattern with the S component in the fault plane approximately 2.5 times larger than the S component in the auxiliary plane. The same factor applies to the S_{\max}/P_{\max} ratio.
- The earthquake source produces static, azimuthally dependent values of pressure and body rotation. The feature should cause an increase in surface wave excitation for earthquakes relative to explosions and may be responsible for the effectiveness of the M_s/m_b discriminant.
- Peak particle velocity (v) is linearly related to the product of rupture velocity (V_R) and dynamic stress drop ($\tau_0 - \tau_k$). From Fig. 22

$$v = 0.35 V_R (\tau_0 - \tau_k) \quad (4.1)$$

where the constant has units of $(m)(km)^{-1}(kb)^{-1}$ and represents an azimuthal average.

- At low frequencies, the displacement spectrum shows an f^{-1} trend, caused by the local static displacement. At high frequencies the spectrum decays as f^{-3} , indicating that the equivalent elastic source should be continuous in both displacement and particle velocity.
- Corner frequency (f_c) seems to be linearly related to the ratio of rupture velocity (V_R) and fault length (L). From Fig. 44

$$f_c = 0.4 \frac{V_R}{L} \quad (4.2)$$

- There is some indication that value of the displacement spectrum (\hat{u}) at the corner frequency is proportional to the product of fault length (L) and stress drop ($\tau_0 - \tau_k$). From Figs. 45 through 48

$$\hat{u} = 0.4 L (\tau_0 - \tau_k) \quad (4.3)$$

where the coefficient has units of $(m)(sec)(km)^{-1}(kb)^{-1}$.

Equations (4.1), (4.2), and (4.3) do not permit a unique determination of V_R , L and $\tau_0 - \tau_k$ given v , u and f_c in the near field. However, if limits can be placed on one of the parameters, the stress drop for instance, then the remaining parameters may also be limited.

For example, suppose the following near field measurements have been obtained:

$$f_c = 1 \text{ Hz}$$

$$\hat{u} = 8 \times 10^{-2} \text{ m-sec (at 10 km)}$$

and the stress drop ($\tau_0 - \tau_k$) is assumed to be 0.2 kbar. Equation (4.3) gives

$$L = 1 \text{ km}$$

and Eq. (4.2) gives

$$V_R = 2.5 \text{ km/sec}$$

This implies that a peak particle velocity of approximately 18 cm/sec has also been measured. If the stress drop is doubled then both the rupture velocity and fault length must be decreased by the same factor.

Equations (4.1), (4.2) and (4.3) should be regarded as a means of obtaining at least some insight into the parameters required by the rupture model in order to match a given set of near field data. Iteration on the parameters will obviously be required in order to produce the optimum match.

Finally, the code is practically unlimited in terms of its ability to accept a given rupture model. This flexibility has been obtained by isolating the normal and tangential stress components at the fault surface and solving for these stress components using contact discontinuity boundary conditions. A description of the rupture process now depends only on an imaginative interpretation and synthesis of appropriate laboratory test data.

V. REFERENCES

1. Reid, H. F., "The Mechanics of Earthquakes. The Elastic Rebound Theory. Regional Strain," Bull. Nat. Res. Council, No. 90, 1933.
2. Benioff, Hugo, "Earthquake Source Mechanisms," Science, 143, March 1964.
3. Haskell, N. A., "Elastic Displacements in the Near Field of a Propagating Fault," Bull. Seism. Soc. Am., 59, April 1969.
4. Savage, J. C., "Radiation from a Realistic Model of Faulting," Bull. Seism. Soc. Am., 56, 1966.
5. Archambeau, C. B., "General Theory of Elastodynamic Source Fields," Reviews of Geophysics, 6, No. 3, 1968.
6. Burridge, R., "The Numerical Solution of Certain Integral Equations with Non-integrable Kernels Arising in the Theory of Crack Propagation and Elastic Wave Diffraction," Phil. Trans. Roy. Soc. London, Ser. A, 265, December 1969.
7. Richards, Paul G., "The Dynamic Field of a Growing Plane Elliptical Shear Crack," Lamont-Doherty Geological Observatory, (contribution number to be assigned), 1972.
8. Cherry, J. T., S. Sack, G. Maenchen, and V. Kransky, "Two-dimensional Stress Induced Adiabatic Flow," Lawrence Livermore Laboratory, UCRL-50987, 1970.
9. Wilkins, M. L., "Calculation of Elastic-Plastic Flow," in Methods in Computational Physics, Vol. 3, 1964, pp. 211-263.
10. Sedgwick, R. T., and D. A. Wolfgang, "CRAM, A Two-Dimensional Lagrangian Code for Elastic-Plastic Hydrodynamic Material Behavior," General Electric Co., Report No. 695D1002, February 1969.
11. Cherry, J. T., and W. R. Hurdlow, "Numerical Simulation of Seismic Disturbances," Geophysics, 31, February 1966.
12. Cherry, J. T., "Computer Calculations of Explosion-Produced Craters," Int. J. Rock Mech. Min. Sci., 4, pp. 1-22, 1967.

14. Butkovich, T. R., "Calculation of the Shock Wave from an Underground Nuclear Explosion in Granite," J. Geophys. Res., 70, February 1965.
15. Riney, T. D., G. A. Frazier, S. K. Garg, A. J. Good, R. G. Herrmann, L. W. Morland, J. W. Pritchett, M. H. Rice, and J. Sweet, "Constitutive Models and Computer Techniques for Ground Motion Predictions," Systems, Science and Software, Report SSS-R-73-1490, March 1973.
16. Cherry, J. T., C. B. Archambeau, G. A. Frazier, A. J. Good, K. G. Hamilton, and D. J. Harkrider, "The Teleseismic Radiation Field from Explosions," Systems, Science and Software, Report SSS-R-72-1193, July 1972.
17. Cherry, J. T., A. J. Good, and K. G. Hamilton, "Free Field Calculations for Seismic Predictions," Systems, Science and Software, Report SSS-R-73-1605, April 1973.

19. Johnson, T., F. T. Wu, and C. H. Scholz, "Source Parameters for Stick-Slip and for Earthquakes," Science, 179, January 1973.
20. Byerlee, J. D., "Static and Kinetic Friction of Granite at High Normal Stress," Int. J. Rock Mech. Min. Sci., 7, pp. 577-582, 1970.

APPENDIX I

The difference equations used in CRAM^[10] to move an interior point are written such that the boundary conditions for an exterior point are obscured. Since we would like to isolate the normal and tangential stresses at an interior interface, this requires that the interface be treated as an exterior line over which the correct boundary stresses are applied. In this section a differencing scheme is obtained that isolates the boundary stresses and that is consistent with the CRAM interior difference equations.

The conservation of linear momentum (equation of motion) in two-dimensional Cartesian geometry is

$$\frac{d\dot{x}}{dt} = \frac{1}{\rho} \left[\frac{\partial \bar{xx}}{\partial x} + \frac{\partial \bar{xy}}{\partial y} \right] \quad (1)$$

$$\frac{d\dot{y}}{dt} = \frac{1}{\rho} \left[\frac{\partial \bar{yy}}{\partial y} + \frac{\partial \bar{xy}}{\partial x} \right] \quad (2)$$

If a Lagrangian coordinate system (k, j) is established in the material, then

$$\frac{\partial \Sigma}{\partial k} = \frac{\partial \Sigma}{\partial x} \frac{\partial x}{\partial k} + \frac{\partial \Sigma}{\partial y} \frac{\partial y}{\partial k}$$

$$\frac{\partial \Sigma}{\partial j} = \frac{\partial \Sigma}{\partial x} \frac{\partial x}{\partial j} + \frac{\partial \Sigma}{\partial y} \frac{\partial y}{\partial j}$$

where Σ is a typical stress component (\bar{xx} , \bar{yy} , \bar{xy}) in the equation of motion. Solving for $\partial \Sigma / \partial x$ and $\partial \Sigma / \partial y$ gives

$$\frac{\partial \Sigma}{\partial x} = \frac{1}{J} \left[\frac{\partial \Sigma}{\partial j} \frac{\partial y}{\partial k} - \frac{\partial \Sigma}{\partial k} \frac{\partial y}{\partial j} \right] \quad (3)$$

$$\frac{\partial \Sigma}{\partial y} = -\frac{1}{J} \left[\frac{\partial \Sigma}{\partial j} \frac{\partial x}{\partial k} - \frac{\partial \Sigma}{\partial k} \frac{\partial x}{\partial j} \right] \quad (4)$$

where

$$J = \frac{\partial x}{\partial j} \frac{\partial y}{\partial k} - \frac{\partial x}{\partial k} \frac{\partial y}{\partial j} \quad (5)$$

If the k, j coordinates assume discrete values

$$1, 2, \dots k-1, k, k+1, \dots k_{\max}$$

$$1, 2, \dots j-1, j, j+1, \dots j_{\max}$$

then

$$\vec{R}_j \times \vec{R}_k = |\vec{R}_j| |\vec{R}_k| \sin \alpha \vec{e} = 2A_a \vec{e} \quad (6)$$

where

$$\vec{R}_j = \frac{\partial x}{\partial j} \vec{e}_x + \frac{\partial y}{\partial j} \vec{e}_y \quad \vec{R}_k = \frac{\partial x}{\partial k} \vec{e}_x + \frac{\partial y}{\partial k} \vec{e}_y$$

Also

$$\vec{R}_j \times \vec{R}_k = \left(\frac{\partial x}{\partial j} \frac{\partial y}{\partial k} - \frac{\partial x}{\partial k} \frac{\partial y}{\partial j} \right) \vec{e}_x \times \vec{e}_y = J \vec{e}_k \times \vec{e}_y \quad (7)$$

Comparing Eqs. (6) and (7) shows that a good approximation to J will be the zone area ($A_a + A_b$) if

$$\vec{e} = \vec{e}_x \times \vec{e}_y \quad (8)$$

Equation (8) is satisfied if the x, y and k, j coordinates have the same relative orientation as that shown in Fig. 1, i.e., if the unit vector obtained from the $\vec{j} \times \vec{k}$ operation is equal to the unit vector from $\vec{e}_x \times \vec{e}_y$.

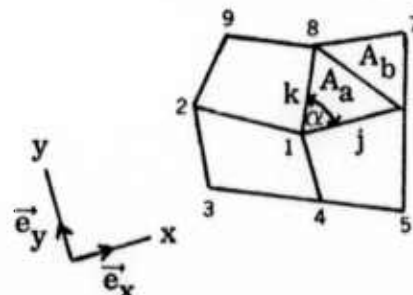


Fig. 1--The x, y and k, j coordinate system.

Figure 1 also shows the numbering system to be used for both nodal point and interior variables. Table 1 gives the equivalence between the numbering system and the k, j values.

Table 1

Number	k, j Interior	k, j Exterior
1	$k-1/2, j-1/2$	k, j
2		$k, j-1$
3		$k-1, j-1$
4		$k-1, j$
5		$k-1, j+1$
6	$k-1/2, j+1/2$	$k, j+1$
7	$k+1/2, j+1/2$	$k+1, j+1$
8	$k+1/2, j+1/2$	$k+1, j$
9		$k+1, j-1$

Typical interior variables are density, stress, strain, internal energy and area. Exterior variables are acceleration, velocity and position vector.

Equations (3) and (4) and Fig. 1 suggest a rather natural differencing scheme; i. e.,

$$\frac{1}{\rho} \frac{\partial \Sigma}{\partial x} = \frac{\sum_{78} y_{81}}{\frac{\rho_7 J_7 + \rho_8 J_8}{2}} w_k + \frac{\sum_{61} y_{14}}{\frac{\rho_6 J_6 + \rho_1 J_1}{2}} (1 - w_k) - \frac{\sum_{76} y_{61} w_j}{\frac{\rho_7 J_7 + \rho_6 J_6}{2}}$$

$$- \frac{\sum_{81} y_{12}}{\frac{\rho_8 J_8 + \rho_1 J_1}{2}} (1 - w_j) \quad (9)$$

$$\frac{1}{\rho} \frac{\partial \Sigma}{\partial y} = - \frac{\sum_{78} x_{81}}{\rho_{77} + \rho_{88}} w_k - \frac{\sum_{61} x_{14}}{\rho_{66} + \rho_{11}} (1 - w_k) + \frac{\sum_{76} x_{61} w_j}{\rho_{77} + \rho_{66}} \\ + \frac{\sum_{81} x_{12}}{\rho_{88} + \rho_{11}} (1 - w_j) \quad (10)$$

where $\Sigma_{28} = \Sigma_7 - \Sigma_8$, $y_{81} = y_8 - y_1$, etc., and w_k and w_j weight the individual acceleration components based on their location with respect to point 1.

A fairly simple weighting scheme used in the TENSOR code^[8] is

$$w_k = \frac{\vec{R}_{14} \cdot \vec{R}_{84}}{\vec{R}_{84} \cdot \vec{R}_{84}} \quad w_j = \frac{\vec{R}_{12} \cdot \vec{R}_{62}}{\vec{R}_{62} \cdot \vec{R}_{62}}$$

In Eqs. (9) and (10), if

$$w_k = w_j = 1/2 \quad (11)$$

$$\frac{\rho_c J_c + \rho_d J_d}{2} = \frac{\rho_1 J_1 + \rho_2 J_2 + \rho_3 J_3 + \rho_4 J_4}{4} \quad (12)$$

then the CRAM interior differencing is obtained. Both HEMP^[9] and CRAM use the same interior differencing scheme. Equations (11) and (12) reduce the TENSOR difference equations to those of CRAM and HEMP.

If a k line is to be decoupled from the grid, as in Fig. 2, then Eqs. (9) and (10) permit this if $w_k^+ = 1$ for k^+ and $w_k^- = 0$ for k^- . For a point on k^+ , $w_k = 1$ and $w_\ell = 1/2$. Equations (9), (10) and (12) may be used to write the spatial derivatives in Eqs. (1) and (2) giving

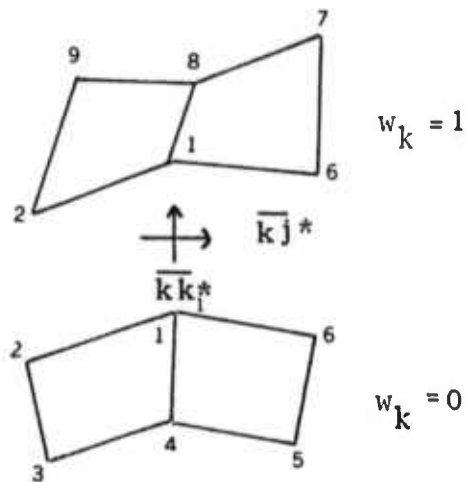


Fig. 2--A decoupled interior grid line. The boundary stresses $\bar{k}k^*$ and $\bar{k}j^*$ do not change when the interface is viewed from below ($w_k = 1$) or above ($w_k = 0$).

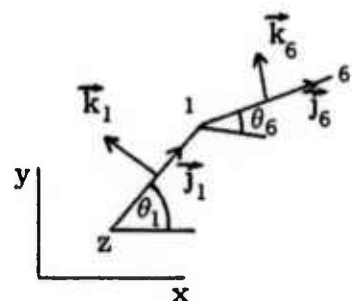


Fig. 3--The orthogonal \bar{j} , \bar{k} unit vectors.

$$\frac{1}{\rho} \frac{\partial \bar{xx}}{\partial x} = \frac{\bar{xx}_{7,8} y_{8,1}}{\phi^+} - \left[\frac{(\bar{xx}_7 - \bar{xx}_6^*) y_{6,1} + (\bar{xx}_8 - \bar{xx}_1^*) y_{1,2}}{\phi^+} \right] \quad (13)$$

$$\frac{1}{\rho} \frac{\partial \bar{xy}}{\partial y} = - \frac{\bar{xy}_{7,8} x_{8,1}}{\phi^+} + \left[\frac{(\bar{xy}_7 - \bar{xy}_6^*) x_{6,1} + (\bar{xy}_8 - \bar{xy}_1^*) x_{1,2}}{\phi^+} \right] \quad (14)$$

$$\frac{1}{\rho} \frac{\partial \bar{yy}}{\partial y} = - \frac{\bar{yy}_{7,8} x_{8,1}}{\phi^+} + \left[\frac{(\bar{yy}_7 - \bar{yy}_6^*) x_{6,1} + (\bar{yy}_8 - \bar{yy}_1^*) x_{1,2}}{\phi^+} \right] \quad (15)$$

$$\frac{1}{\rho} \frac{\partial \bar{xy}}{\partial x} = \frac{\bar{xy}_{7,8} y_{8,1}}{\phi^+} - \left[\frac{(\bar{xy}_7 - \bar{xy}_6^*) y_{6,1} + (\bar{xy}_8 - \bar{xy}_1^*) y_{1,2}}{\phi^+} \right] \quad (16)$$

where

$$\phi^+ = \frac{\rho_7 J_7 + \rho_8 J_8}{2} \quad (17)$$

Along a typical interface line joining two adjacent nodal points (Fig. 3) orthogonal unit vectors \vec{k} and \vec{j} are

$$\vec{k} = -\vec{e}_x \sin\theta + \vec{e}_y \cos\theta \quad (18)$$

$$\vec{j} = \vec{e}_x \cos\theta + \vec{e}_y \sin\theta$$

The stress components in this coordinate system are

$$\bar{kk} = \bar{yy} \cos^2\theta + \bar{xx} \sin^2\theta - 2\bar{xy} \sin\theta \cos\theta \quad (19)$$

$$\bar{kj} = \bar{xy}(\cos^2\theta - \sin^2\theta) + (\bar{yy} - \bar{xx}) \sin\theta \cos\theta \quad (20)$$

$$\bar{jj} = \bar{xx} \cos^2\theta + \bar{yy} \sin^2\theta + 2\bar{xy} \sin\theta \cos\theta \quad (21)$$

The acceleration of a point on k^+ may be written as

$$\left(\frac{d\dot{x}}{dt} \right)^+ = \frac{1}{\phi^+} \left[\bar{xx}_{7,8} y_{8,6} + \bar{xx}_8 y_{2,8} - \bar{xy}_7 x_{8,6} - \bar{xy}_8 x_{2,8} + \bar{kk}_6^* y_{6,1}^+ + \bar{kk}_1^* y_{1,2}^+ - \bar{kj}_6^* x_{6,1}^+ - \bar{kj}_1^* x_{1,2}^+ \right] \quad (22)$$

$$\left(\frac{dy}{dt}\right)^+ = \frac{1}{\phi^+} \left[-\bar{yy}_7 x_{86}^- + \bar{yy}_8 x_{28}^- + \bar{xy}_7 y_{86}^- + \bar{xy}_8 y_{28}^- - \bar{kk}_6^* x_{61}^+ \right. \\ \left. - \bar{kj}_1^* x_{12}^+ - \bar{kj}_6^* y_{61}^+ - \bar{kj}_1^* y_{12}^+ \right] \quad (23)$$

Similarly, the acceleration of a point on k^- may be written as

$$\left(\frac{dx}{dt}\right)^- = \frac{1}{\phi^-} \left[\bar{xx}_6 y_{64}^- + \bar{xx}_1 y_{42}^- - \bar{xy}_6 x_{64}^- - \bar{xy}_1 x_{42}^- - \bar{kk}_6^* y_{61}^- \right. \\ \left. - \bar{kk}_1^* y_{12}^- + \bar{kj}_6^* x_{61}^- + \bar{kj}_1^* x_{12}^- \right] \quad (24)$$

$$\left(\frac{dy}{dx}\right)^- = \frac{1}{\phi^-} \left[-\bar{yy}_6 x_{64}^- + \bar{yy}_1 x_{42}^- + \bar{xy}_6 y_{64}^- + \bar{xy}_1 y_{42}^- + \bar{kk}_6^* x_{61}^- \right. \\ \left. + \bar{kk}_1^* x_{12}^- + \bar{kj}_6^* y_{61}^- + \bar{kj}_1^* y_{12}^- \right] \quad (25)$$

These equations have been derived assuming that \bar{kk}_6^* , \bar{kj}_6^* , \bar{kk}_1^* and \bar{kj}_1^* are specified along the 6-2 interface, finding the corresponding stresses in the x,y coordinate system, i.e.,

$$\bar{xx}^* = \bar{jj}^* \cos^2 \theta + \bar{kk}^* \sin^2 \theta - 2\bar{kj}^* \sin \theta \cos \theta \quad (26)$$

$$\bar{yy}^* = \bar{jj}^* \sin^2 \theta + \bar{kk}^* \cos^2 \theta + 2\bar{kj}^* \sin \theta \cos \theta \quad (27)$$

$$\bar{xy}^* = (\bar{jj}^* - \bar{kk}^*) \sin \theta \cos \theta + \bar{kj}^* (\cos^2 \theta - \sin^2 \theta) \quad (28)$$

and then substituting these expressions for \bar{xx}_6^* , \bar{yy}_6^* , \bar{xy}_6^* , \bar{xx}_1^* , \bar{yy}_1^* , \bar{xy}_1^* into Eqs. (13) through (16)

Equations (22) through (25) will be used to move the points on the decoupled grid line. They are consistent with the interior difference equations.

APPENDIX II

In order to use Equations 22 through 25 in Appendix I the boundary stresses must be specified. In order to solve for these stresses we apply contact discontinuity boundary conditions, which require that the normal component of stress and normal component of velocity be continuous at the boundary.

The unit vectors normal and tangent to the 6-2 interface may be written

$$\begin{aligned}\vec{k} &= -\sin\theta \vec{e}_x + \cos\theta \vec{e}_y & \vec{e}_x &= -\sin\theta \vec{k} + \cos\theta \vec{j} \\ \vec{j} &= \cos\theta \vec{e}_x + \sin\theta \vec{e}_y & \vec{e}_y &= \cos\theta \vec{k} + \sin\theta \vec{j}\end{aligned}\quad (1)$$

The acceleration components on the plus side of the line may be written

$$a_k^+ = \frac{1}{\phi^+} \left[g_k^+ + R_{61} \vec{K} \vec{k}_7 + R_{12} \vec{K} \vec{k}_8 - (R_{61} + R_{12}) \vec{K} \vec{k}^* \right] \quad (2)$$

$$a_j^+ = \frac{1}{\phi^+} \left[g_j^+ + R_{61} \vec{K} \vec{j}_7 + R_{12} \vec{K} \vec{j}_8 - (R_{61} + R_{12}) \vec{K} \vec{j}^* \right] \quad (3)$$

The corresponding acceleration components on the minus side are

$$a_k^- = \frac{1}{\phi^-} \left[g_k^- + (R_{61} + R_{12}) \vec{K} \vec{k}^* - R_{61} \vec{K} \vec{k}_6 - R_{12} \vec{K} \vec{k}_1 \right] \quad (4)$$

$$a_j^- = \frac{1}{\phi^-} \left[g_j^- + (R_{61} + R_{12}) \vec{K} \vec{j}^* - R_{61} \vec{K} \vec{j}_6 - R_{12} \vec{K} \vec{j}_1 \right] \quad (5)$$

where

$$g_k^+ = -(\bar{xx}_{7,8} y_{8,1} - \bar{xy}_{7,8} x_{8,1}) \sin\theta - (\bar{yy}_{7,8} x_{8,1} - \bar{xy}_{7,8} y_{8,1}) \cos\theta \quad (6)$$

$$g_k^- = -(\bar{xx}_{6,1} y_{1,4} - \bar{xy}_{6,1} x_{1,4}) \sin\theta - (\bar{yy}_{6,1} x_{1,4} - \bar{xy}_{6,1} y_{1,4}) \cos\theta$$

$$g_j^+ = (\bar{xx}_{7,8} y_{8,1} - \bar{xy}_{7,8} x_{8,1}) \cos\theta - (\bar{yy}_{7,8} x_{8,1} - \bar{xy}_{7,8} y_{8,1}) \sin\theta \quad (7)$$

$$g_j^- = (\bar{xx}_{6,1} y_{1,4} - \bar{xy}_{6,1} x_{1,4}) \cos\theta - (\bar{yy}_{6,1} x_{1,4} - \bar{xy}_{6,1} y_{1,4}) \sin\theta$$

$$\phi^+ = \frac{1}{2} [\rho_7 J_7 + \rho_8 J_8] \quad \phi^- = \frac{1}{2} [\rho_6 J_6 + \rho_1 J_1] \quad (8)$$

Equations 2 through 5 have been derived from Equations 13 through 16 in Appendix I by assuming that the boundary stress is uniform over the entire 6-2 portion of the grid line. These equations, therefore, are not completely consistent with the interior difference equations. The assumption concerning uniform boundary stress is necessary since the contact discontinuity boundary conditions will result in an equation that relates the normal components of acceleration on the plus and minus side of the boundary. This equation should contain only one unknown, i.e., the normal component of the boundary stress.

In order to find the relation between the above acceleration components at a slipping interface, we follow the technique used by Cherry, et al.^[8] and attach a coordinate system to the point on the minus side, with \hat{k} and \hat{j} being the unit vectors normal and tangent to the slip line at the point to be moved.

If \vec{v}^+ and \vec{v}^- are the velocities on the plus and minus side of the slip line then, from Equation 1, the normal components of velocity are given by

$$\begin{aligned}\vec{v}^+ \cdot \vec{k} &= -\dot{x}^+ \sin\theta + \dot{y}^+ \cos\theta \\ \vec{v}^- \cdot \vec{k} &= -\dot{x}^- \sin\theta + \dot{y}^- \cos\theta\end{aligned}\quad (9)$$

If

$$x_\ell^- = \frac{\partial x^-}{\partial \ell} \quad y_\ell^- = \frac{\partial y^-}{\partial \ell} \quad R_\ell = [(x_\ell^-)^2 + (y_\ell^-)^2]^{1/2}$$

then

$$\sin\theta = \frac{y_\ell^-}{R_\ell} \quad \cos\theta = \frac{x_\ell^-}{R_\ell} \quad (10)$$

Substituting Equation 10 into 9, and equating normal velocity components gives

$$R_\ell \vec{v}^- \cdot \vec{k} = R_\ell \vec{v}^+ \cdot \vec{k} \quad (11)$$

or

$$-\dot{x}^- y_\ell^- + \dot{y}^- x_\ell^- = -\dot{x}^+ y_\ell^- + \dot{y}^+ x_\ell^- \quad (12)$$

Since the $\vec{k}, \vec{\ell}$ coordinate system is attached to the minus side of the slip line then

$$\frac{d}{dt} (-\dot{x}^- y_\ell^- + \dot{y}^- x_\ell^-) = \frac{\partial}{\partial t} (-\dot{x}^+ y_\ell^- + \dot{y}^+ x_\ell^-) \Big|_{k, \ell \text{ constant}} \quad (13)$$

The left side of Equation 13 may be written

$$\begin{aligned} & -y_{\ell} \frac{d}{dt}(\dot{x}_{\ell}) + x_{\ell} \frac{d}{dt} \dot{y}_{\ell} - \dot{x}_{\ell} \dot{y}_{\ell} + \dot{y}_{\ell} \dot{x}_{\ell} \\ & = R_{\ell} a_k^+ + (\vec{v}^+ \cdot \vec{k})(\vec{v}_{\ell}^- \cdot \vec{j}) - (\vec{v}^- \cdot \vec{\ell})(\vec{v}_{\ell}^- \cdot \vec{k}) \end{aligned} \quad (14)$$

Since

$$\begin{aligned} \frac{d}{dt}(R_{\ell} v^+ \cdot \vec{k}) &= \frac{\partial}{\partial t}(R_{\ell} v^+ \cdot \vec{k}) + \frac{(v^+ - v^-)}{R_{\ell}} \cdot \vec{\ell} \frac{\partial}{\partial \ell}(R_{\ell} \vec{v}^+ \cdot \vec{k}) \\ &+ \frac{(v^+ - v^-) \cdot \vec{k}}{R_{\ell}} \cdot \frac{\partial}{\partial k}(R_{\ell} \vec{v}^+ \cdot \vec{k}) \end{aligned}$$

and

$$(v^+ - \vec{v}) \cdot \vec{k} = 0$$

Then the right side of Equation 13 may be written

$$\begin{aligned} & \frac{\partial}{\partial t}(-\dot{x}_{\ell}^+ y_{\ell}^- + \dot{y}_{\ell}^+ x_{\ell}^-) \\ &= R_{\ell} a_k^+ + (\vec{v}^+ \cdot \vec{k})(\vec{v}_{\ell}^- \cdot \vec{j}) - (\vec{v}^- \cdot \vec{\ell})(\vec{v}_{\ell}^- \cdot \vec{k}) - (v^+ - v^-) \cdot \vec{\ell} \vec{v}_{\ell}^+ \cdot \vec{k} \end{aligned} \quad (15)$$

In Equations 14 and 15 a_k^+ and a_k^- are given by

$$a_k^+ = - \frac{d(\dot{x}_{\ell}^+)}{dt} \frac{y_{\ell}^-}{R_{\ell}} + \frac{d(\dot{y}_{\ell}^+)}{dt} \frac{y_{\ell}^-}{R_{\ell}}$$

$$a_k^- = - \frac{d(\dot{x}_{\ell}^-)}{dt} \frac{y_{\ell}^+}{R_{\ell}} + \frac{d(\dot{y}_{\ell}^-)}{dt} \frac{y_{\ell}^+}{R_{\ell}}$$

and are the same acceleration components given by Equations 2 and 4. We have also used the relation

$$-\dot{x}^{\pm} \dot{y}_{\ell}^{\pm} + \dot{y}^{\pm} \dot{x}_{\ell}^{\pm} = (\vec{v}^{\pm} \cdot \vec{k}) (\vec{v}_{\ell}^{\pm} \cdot \vec{j}) - (\vec{v}^{\pm} \cdot \vec{l}) (\vec{v}_{\ell}^{\pm} \cdot \vec{k}) \quad (16)$$

in order to derive Equations 14 and 15.

Substituting Equations 14 and 15 into Equation 13 gives

$$a_k^+ - a_k^- = A_c \quad (16)$$

where

$$A_c = \frac{(\vec{v}^+ - \vec{v}^-) \cdot \vec{l} (\vec{v}_{\ell}^+ + \vec{v}_{\ell}^-) \cdot \vec{k}}{R_{\ell}} \quad (17)$$

Solving Equation 16 for $\bar{k}\bar{k}^*$ gives

$$\bar{k}\bar{k}^* = \frac{\phi^- g_k^+ - \phi^+ g_k^- + \phi^- (R_{61} \bar{k}\bar{k}_7 + R_{12} \bar{k}\bar{k}_8) + \phi^+ (R_{61} \bar{k}\bar{k}_6 + R_{12} \bar{k}\bar{k}_1) - \phi^+ \phi^- A_c}{(R_{61} + R_{12})(\phi^+ + \phi^-)} \quad (18)$$

Equation 18 relates the normal component of stress ($\bar{k}\bar{k}^*$) at the slipping interface to interior zone variables. In order to move the boundary points then $\bar{k}\bar{j}^*$ in Equations 22 through 24 in Appendix I must also be specified.

For a tied point A_c in Equation 18 is set equal to zero, since

$$(\vec{v}^+ - \vec{v}^-) \cdot \vec{l} = 0 .$$

Also the tangential stress component, for a tied point, is obtained from Equations 3 and 5. Since

$$a_j^+ = a_j^-$$

then for a tied point

$$\bar{k}_j^* = \frac{\phi^- g_j^+ - \phi^+ g_j^- + \phi^- (R_{61} \bar{k}_j^7 + R_{12} \bar{k}_j^8) + \phi^+ (R_{61} \bar{k}_j^6 + R_{12} \bar{k}_j^1)}{(R_{61} + R_{12})(\phi^+ + \phi^-)} \quad (19)$$

APPENDIX III

Plastic flow is due to the inability of real materials to support unlimited values of shear stress. In the code the deviatoric stress components are modified such that the resulting stress state is consistent with a Mises yield criterion.

If the second deviatoric invariant (J) is greater than a specified value ($1/3 Y^2$), then

$$S_{ij} = \hat{S}_{ij} - \frac{Y}{\sqrt{3J}} \left(J > \frac{Y^2}{3} \right) \quad (1)$$

where S_{ij} is the adjusted stress deviator

\hat{S}_{ij} is the stress deviator calculated by assuming that the total strain rate is elastic, and

$$J = \frac{1}{2} (\hat{S}_{ij} \hat{S}_{ji}) \quad (2)$$

For a triaxial test, Y corresponds to the maximum allowable stress difference at failure.

Rupture initiation is being modeled by accumulating the difference between $\sqrt{3J}$ and Y during yielding. When this accumulation reaches a specified value then the point at the fault surface enters the slip routine. Between two consecutive cycles, n and $n+1$, the accumulation takes the form

$$e^{n+1} = e^n + \frac{\sqrt{3J} - Y}{Y}, \quad \left(J > \frac{Y^2}{3} \right) \quad (3)$$

$$e^{n+1} = e^n \quad \left(J \leq \frac{Y^2}{3} \right)$$

Rupture occurs if

$$e^{n+1} \geq w \quad (4)$$

where w is a specified function of distance from the initial point of rupture (the focus).

Equation (3) is similar to a plastic work criterion, where the plastic work (E^{n+1}) is given by

$$E^{n+1} = E^n + \frac{Y^2}{3\mu} \frac{\sqrt{3J} - Y}{Y} \quad (5)$$

Equations (3) and (5) differ only by the factor $Y^2/3\mu$.

We have been successful in both controlling rupture velocity and reducing the stress concentrations at the end of the fault by allowing w , in Eq. (4), to be a specified function of distance from the point of rupture initiation. The functional form that has been used is

$$w = 6c \left(\frac{x + L/2}{d} \right)^2 \left[\frac{1}{2} - \frac{1}{3} \frac{x + L/2}{d} \right] \quad 0 \leq x + \frac{L}{2} \leq \frac{1}{2} \quad (6a)$$

$$= \frac{c}{2} \left[-\frac{1}{2} + 3 \frac{x + L/2}{d} \right] \quad x + \frac{L}{2} \geq \frac{1}{2} \quad (6b)$$

where L , c and d are input parameters. The rupture is constrained to lie between $-L/2 \leq x \leq L/2$, where L is the fault length.